GROWTH MODEL, SYNTHESIS OF CARBON NANOSTRUCTURES AND ALTERATION OF SURFACE PROPERTIES USING THEM

Sayangdev Naha

PhD Dissertation

Submitted to the Faculty of Virginia Polytechnic Institute and State University in partial fulfillment of the requirements
of the degree of Doctor of Philosophy in Engineering Mechanics

Committee Members:

Dr. Ishwar K. Puri, Chair
Dr. Mark S. Cramer
Dr. Muhammad R. Hajj
Dr. John J. Lesko
Dr. Roop L. Mahajan
Dr. Mayuresh J. Patil

07/25/2008
Blacksburg, Virginia

Keywords: Carbon nanotubes, carbon nanofibers, catalysis, nanotechnology, flame synthesis, silicon nanowires, superhydrophobicity

GROWTH MODEL, SYNTHESIS OF CARBON NANOSTRUCTURES AND ALTERATION OF SURFACE PROPERTIES USING THEM

SAYANGDEV NAHA

ABSTRACT

Flame synthesis is recognized as a much cheaper and higher throughput process for carbon nanotube/nanofiber (CNT/CNF) production compared to conventional catalytic processes like chemical vapor deposition (CVD). Nanostructured carbon materials, such as carbon nanotubes and nanofibers, exhibit superhydrophobic behavior over a range of pH values, including for corrosive liquids. Part of this research reports the development of a rapid on-demand process for the synthesis of superhydrophobic surfaces on silicon (Si) discs using an ethylene-air nonpremixed flame. Such superhydrophobic behavior, combined with increase in effective surface area due to carbon nanostructure (CNS) deposition and corresponding desirable size (nanoscale roughness) attract the growth and attachment of microbial colonies to these CNS-enhanced substrates. This has potentially high-impact application in microbial fuel cells (MiFCs) whereby stainless steel (SS) meshes coated with flame-deposited CNS are used as anodes and the electrons produced by attaching biofilms can generate electricity in a fuel cell. However, despite such and many other applications and promise of carbon nanotubes (CNTs), their production is generally based on empirical principles. There are only a few CNT formation models that predict the dependence of CNT growth on various

synthesis parameters. Typically, these do not incorporate a detailed mechanistic consideration of the various processes that are involved during CNT synthesis. Herein, this need is addressed and a model is presented for catalytic CNT growth that integrates various interdependent physical and chemical mechanisms involved in CNT production. It is validated by comparing its predictions with experimental measurements for CVD synthesis of CNTs and a concise parametric study is presented. The results are extrapolated for flame synthesis that is recognized as a desirable cost-effective process for the bulk synthesis of CNTs, as already mentioned. The last part of this dissertation discusses an extension of the CNT growth model to silicon nanowire/nanowhisker (SiNW) synthesis. SiNWs are synthesized by a number of methods – catalysis by a metal (involving vapor-liquid-solid or VLS growth mode), molecular beam epitaxy, thermal evaporation and laser ablation to name a few. Our model pertains to metal-catalyzed VLS growth mode.

This dissertation is dedicated to my parents, Mr. Tapan Naha and Mrs. Bandana Naha, and my brother Mr. Arkaprovo Naha, without whose encouragement and support from miles away I could not have accomplished my PhD

ACKNOWLEDGEMENTS

I am indebted to my advisor Prof. Ishwar K. Puri for his unwavering support and faith in my capabilities, which made sure I reach this point in my life and my doctoral studies. I acknowledge his role as a mentor, a philosopher and a friend in my endeavor, which most certainly cannot be eclipsed by anyone else. He shared his thorough knowledge and insight on my PhD research topic(s) and guided me through a series of extremely intellectually stimulating discussions over the past four years. His contribution to this work has been immense. I thank him from the core of my heart.

I acknowledge the various stimulating discussions, ideas and support provided by my collaborators and friends in the Multiphysics Research Group – Dr. Soumik Banerjee, Dr. Anindya K. De and Prof. Swarnendu Sen (visiting post-doctoral fellow from Jadavpur University). Without their synergistic excellence and ideas, I could possibly not have reached this stage. I thank my collaborators Prof. Nancy G. Love from University of Michigan (Department of Civil and Environmental Engineering), Prof. Michael W. Ellis from Virginia Tech (Department of Mechanical Engineering) and their respective graduate students Jeremy S. Guest and Jennifer L. Lamp for their support and brilliant ideas. My heartfelt thanks are expressed to undergraduate students I have mentored on the NSF-supported summer undergraduate research program (SURP) – Ross Frey (Purdue University – Summer 2006), Thomas Cochell (Colorado School of Mines – Summer 2007) and Katherine Radavich (University of Wisconsin-Madison – Summer 2008) for their immense help in part of this research. I express my special thanks and gratitude to Mr. Steve McCartney from the Institute of Critical Technology and Applied Science (ICTAS) for his help with microscopy and surface characterization techniques. I

thank and whole-heartedly acknowledge the support extended by my dissertation committee members – Professors Mark S. Cramer, Muhammad R. Hajj, John J. Lesko, Roop L. Mahajan and Mayuresh J. Patil. I wish to specially thank Prof. Roop L. Mahajan for his excellent ideas and unwavering support for my research.

I want to take this opportunity to specially thank my colleague as well as one of the very best of friends Ashok Sinha for his support through tough times. I would like to thank my other co-worker Ranjan for his help, suggestions and various digressional discussions. Finally, I would take this opportunity to thank my family – my parents Mr. Tapan Naha and Mrs. Bandana Naha and my brother Mr. Arkaprovo Naha, who have been my strength and inspiration throughout my life.

TABLE OF CONTENTS

LIST OF FIGURES

FIGURES **PAGES**

LIST OF TABLES

LIST OF ABBREVIATIONS

a-C	Amorphous carbon
CFD	Computational fluid dynamics
CNF	Carbon nanofiber
CNS	Carbon nanostructure
CNT	Carbon nanotube
CVD	Chemical vapor deposition
EDS/EDX	Energy dispersive X-ray spectroscopy
EELS	Electron energy loss spectra
E-SEM	Environmental scanning electron microscopy
FE-SEM	Field emission scanning electron microscopy
HAB	Height above burner
HR-TEM	High resolution transmission electron microscopy
KJMA	Kolmogorov-Johnson-Mehl-Avrami
MBE	Molecular Beam Epitaxy
MCNP	Metal catalyst nanoparticle
MD	Molecular dynamics
MiFC/MFC	Microbial fuel cell

E. Coli	Escherichia coli
MN	Mononuclear
MWCNT/MWNT	Multi-walled carbon nanotube
PAH	Polycyclic aromatic hydrocarbon
PN	Polynuclear
SEM	Scanning electron microscopy
SiNT	Silicon nanotube
SiNW	Silicon nanowire/nanowhisker
STM	Scanning tunneling microscopy
SWCNT/SWNT	Single-walled carbon nanotube
TEM	Transmission electron microscopy
VLS	Vapor-liquid-solid
XPS	X-ray photoelectron spectroscopy

CHAPTER 1

INTRODUCTION

Carbon nanotubes are graphene sheets rolled into seamless tubes with diameters that are of the order of nanometers. Due to their remarkable mechanical properties (Young's modulus about 1 TPa, Ultimate strength about 100 GPa) they have attracted considerable attention from the scientific community. In the last decade or so, several authors have used computer simulations to evaluate mechanical, thermal and electronic properties of CNTs. These nanotubes basically consist of an intercalation of graphitic planes at a fixed distance (0.355 nm) from each other to form a variety of structures. Carbon nanotubes and nanofibers are usually grown on metallic surfaces by the catalytic action of one or more transition metals. Nanostructured composites are very strong candidates for future light-weight structural materials in aerospace industry. Carbon nanostructures also hold considerable promise in the storage of hydrogen for transportation and power generation applications. Although research on carbon nanostructures is a fast-moving field, commercialization is hampered by the lack of methods to economically produce the material in bulk. Also, previous works on understanding their growth have been primarily empirical and qualitative, with the existence of mechanistic models giving quantitative predictions being almost negligible.

A carbon nanotube can be one of three types: (1) armchair, (2) zigzag and (3) chiral depending on the orientation along which the graphitic planes are folded. **Error! Reference source not found.** below describes the chiral vector $\vec{c}$ and the chiral angle θ. When the value of θ is, respectively, 30º, 0º or anywhere in between, a nanotube is

respectively called zigzag, armchair or chiral. The chiral vector $\vec{c}$ is expressed in terms of the unit vectors $\vec{a}_1$ and $\vec{a}_2$ that are oriented along two particular directions along the unit hexagonal cell. The constants *m* and *n* determine whether the nanotube is of the armchair, zigzag, or chiral type. The nanotube is of the armchair type if *m*=*n*, zigzag if either m or n are zero, and chiral for all other cases.

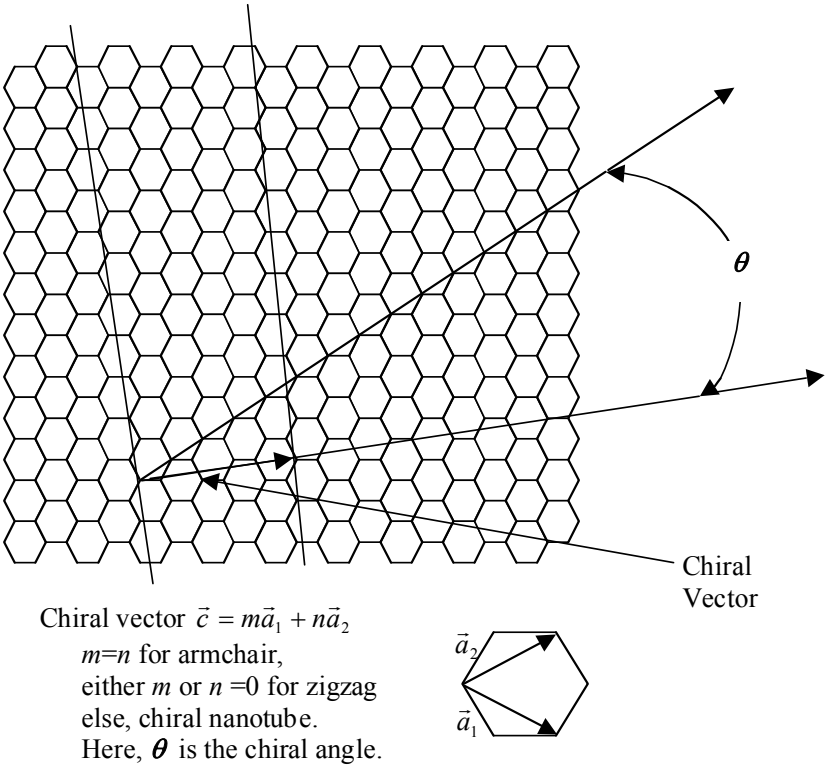

Figure 2.1.1 Various types of carbon nanotubes are characterized by their respective chiral angles

Flame synthesis has been recognized as a desirable cost-effective process for the bulk synthesis of carbon nanotubes and nanofibers, since a much larger throughput can be achieved during flame synthesis as compared to the more conventional CVD and laser ablation processes [1,2]. The existence of hollow carbon filaments in flames was first reported by Singer and Grumer [3] almost a half century ago who noticed their presence

on a stainless steel grid placed in a fuel-rich propane-air flame. Early methods of nanotube [4] and nanowire [5,6] formation also used arc discharge, photolithography and scanning tunneling microscopy (STM). Ajayan and co-workers [7,8,9] reported comprehensive experimental studies on the synthesis of CNTs with well-controlled structures (number of walls, length etc.). Although experimental investigations of CNT flame synthesis have been widely reported recently [10,11,12,13,14,15,16], as yet no comprehensive models have been suggested for this particular process regarding their formation, growth rate or for the characterization of their structure. The available growth models for CNTs are mainly focused on CVD processes. Besides, a comprehensive model that considers and couples all the stages involved in CNT formation satisfactorily (by any method, including CVD) is not yet available in the literature.

A synergistic experimental-computational investigation of CVD as well as flame synthesis of CNTs and CNFs has been provided herein. In the experimental investigation, various graphitic carbon nanostructures are synthesized in well-characterized fuel-rich flames primarily burning ethylene (C_2H_4). These nanostructures are characterized using field emission as well as environmental scanning electron microscopy (FE-SEM and E-SEM respectively) and transmission electron microscopy (TEM). Surface analysis has been conducted using energy dispersive X-ray spectroscopy (EDS/EDX) and X-ray photoelectron spectroscopy (XPS). The experimental measurements are employed to develop and validate a comprehensive mechanistic model to describe the synthesis of carbon nanotubes (CNTs), both by conventional CVD process as well as flame synthesis done in the lab. The output of this model could be used for the molecular modeling of the

structure of CNTs, e.g., using molecular dynamics (MD) simulations, thereby facilitating the development of multiscale models. The salient aspects of the model are:

1. Consideration of the detailed gas phase transport and chemistry of a flame environment, which is essential to identify the key carbon sources. In case of CVD, the feedstock usually contains only one type of hydrocarbon, along with an oxidizing agent and a carrier gas (inert gas like helium (He)) in some cases.
2. Modeling of the adsorption of carbon sources and the accompanying catalytic reactions that result in the deposition of solid carbon on catalyst particles. Although this carbon forms an encapsulating layer that deactivates the catalyst, it also allows for carbon diffusion through the particle.
3. Modeling of the mass transport through the catalyst particle and temperature effect on the parameters.
4. Carbon nucleation following diffusion; as the carbon concentration in the metal particle reaches a critical saturation concentration, it separates out in the form of graphitic filaments at the interface between the metal particle and the substrate on which it is supported.

The nucleation and growth is modeled using nucleation chemistry kinetics, which accounts for carbon-metal (catalyst particle) cluster formation. The formation of nanofibrous carbon is sometimes accompanied by release of gaseous hydrogen [17].

Low-surface-energy materials are frequently used to modify surfaces in order to control surface wettability. Nanostructured carbon materials, such as carbon nanotubes and nanofibers, exhibit superhydrophobic behavior over a range of pH values, including for corrosive liquids. Amorphous carbon (a-C) films also have special wettability

properties. Crystalline silicon is a widely employed substrate for surfaces with controlled chemical and physical properties (e.g., for biosensors, and for studying biomolecular interactions at interfaces). Recently, superhydrophobic surfaces with water contact angle (CA) higher than 150° have attracted much interest because of their potential applications in many industrial processes. Various phenomena, for instance, snow sticking, contamination, oxidation, and current conduction, are expected to become controllable by using such surfaces. Also, reduction of friction during water flow through a closed channel with superhydrophobic interior surfaces is potentially a very useful possible use of hydrophobic surfaces prepared in the way described here because of their excellent stability and high fidelity. In general, the superhydrophobic surfaces were prepared through the combination of low surface free energy and high surface roughness. Therefore, the superhydrophobic surfaces can be obtained mainly by two ways. One way is to generate a rough structure on a hydrophobic surface (CA > 90°), and the other way is to modify an existing rough surface to reduce its surface free energy. The method described herein uses the first technique.

The last portion of this dissertation discusses an extension of the CNT growth model to silicon nanowire/nanowhisker (SiNW) synthesis. SiNWs are synthesized by a number of methods – catalysis by a metal (involving vapor-liquid-solid or VLS growth mode), molecular beam epitaxy (MBE), thermal evaporation and laser ablation to name a few. The VLS growth mode is the one discussed herein (Chapter 5), because of its close similarity to catalytic CNT formation process.

CHAPTER 2

LITERATURE REVIEW

2.1 Previous carbon nanotube synthesis models

Various models have been suggested for the formation of CNTs and carbon nanofibers (CNFs) by CVD (which are summarized in Table 2.1.1). While these models deal with catalytic action, and diffusion and nucleation, most do not combine all of the different processes that contribute to the overall production of CNTs. Moreover, most of the literature related to the flame synthesis of CNTs is experimental and reports observations of the phenomena rather than providing physical insights and characterization of the underlying processes, which is essential for developing comprehensive modeling capabilities for describing the CNT formation under different conditions – in both CVD and flame synthesis.

A number of models pertain to catalysis chemistry have been put forward. Kuwana and Saito [18] suggested a model that describes nanoparticle growth from ferrocene in which they provided a two-step catalytic reaction model for the formation of Fe nanoparticles. Zavarukhin and Kuvshinov [17] proposed a kinetic model for the production of nanofibrous carbon from a methane-hydrogen mixture using nickel as catalyst. They included the effect of catalyst deactivation, which should be an essential component of a comprehensive model. Scott [19] suggested a chemical kinetic model that is based on soot nucleation kinetics for simulating the nucleation and growth of carbon-nickel clusters and single-walled carbon nanotubes. Dateo *et al*. [20] presented a chemical model for the production of carbon nanotubes by using high pressure carbon monoxide (HiPco) as precursor. They provided both detailed and reduced models for the

(1) decomposition of iron pentacarbonyl [$Fe(CO)_5$] which acts as the catalyst precursor, (2) catalyst growth and decomposition, (3) carbon nanotube formation, and (4) overcoating of the catalyst. Zhang and Smith [21] suggested a kinetic model for methane decomposition and the formation of filamentous carbon on a supported cobalt (Co) catalyst. They considered the effects of catalyst deactivation, metal particle size and the carbon density profiles through the catalyst particle at different reaction times. Perez-Cabero *et al*. [22] proposed a kinetic study of carbon nanotube synthesis due to the catalytic decomposition of acetylene over an iron-supported catalyst. They examined the effect of reaction conditions on the reaction yield and on the structural and morphological characteristics of the carbon products that were obtained.

D'Anna *et al*. [23] proposed a reaction pathway for nanoparticle formation in rich premixed atmospheric ethylene flames with C/O ratios across the soot threshold limit. Endo *et al*. [24] conducted a CFD study of carbon nanotube production rates in a CVD reactor based on the catalytic decomposition of xylene. Hinkov *et al*. [25] reported an experimental-modeling study that predicted the effect of gas pressure on the growth rates of single walled carbon nanotubes (SWCNTs) produced by the arc-discharge technique. They used the SPIN and Surface CHEMKIN [26] software packages to solve for the species transport and chemical kinetic effects, and incorporated the chemical model for fullerenes developed by Krestinin and Moravsky [27]. Gommes *et al*. [28] conducted a combined experimental-kinetic modeling study on the effect of operating conditions on the yield of multiwalled CNTs (MWCNTs) in a semi-continuous CVD reactor. They proposed a simple mathematical model for the reaction rate and used mass spectrometry results for the kinetic study, although no direct measurement or prediction of the CNT

production rates was presented. Their (indirect) kinetic model was based on the rate of ethylene decomposition rather than actual CNT production. Yu *et al*. [29] studied the effect of catalyst particle size on the growth rate of CNTs by CVD. They observed that maximum growth occurs for an optimum catalyst particle size, which is 13-15 nm for Fe. They proposed a set of surface reactions and put forward a growth rate expression, which qualitatively explains this optimum size, but their study does not provide quantitative numerical results from their model. Table 2.1.1 is provided below for improved understanding:

Villacampa *et al*. [30] suggested a rate model for the formation of filamentous carbon due to the catalytic decomposition of methane (to form hydrogen). Although they conducted an experimental-numerical study of hydrogen formation, they also included rate equations for the formation of filamentous carbon. Snoeck *et al*. [31] conducted a similar experimental-kinetic modeling study of carbon filament formation on Ni particles in which they considered surface reactions, one-dimensional diffusion (based on Fick's law) of carbon through the catalyst particle and a kinetic prediction of coking threshold. Chen *et al*. [32] investigated the synthesis of carbon nanofibers by CVD and the effect of Ni crystal size on methane decomposition. A recent investigation by Puretzky *et al*. [33] proposed a growth rate model for carbon nanotube formation during CVD. They performed in situ measurements and modeled the growth kinetics of vertically aligned nanotube arrays. Their model focused on CNT growth on a catalyst nanoparticle and suggested some characteristic scales for CNT termination times and termination lengths. As is evident from these examples, various models exist for detailed or semi-detailed descriptions of the nucleation of carbon nanoparticles and the growth of CNTs.

Table 2.1.1 Previous works on modeling of CNT growth

Authors	Mode of synthesis	Temperature of formation	Source of carbon	Catalyst	Modeling approach
De Chen *et al*. (2004)	Tapered oscillating element microbalance (TEOM)	580 ˚C (853 K)	Methane (CH_4)	Nickel	Modeling of carbon diffusion through Ni metal particles used as catalyst and kinetic effects of Ni crystal size based on a detailed kinetic mechanism of carbon nanofiber growth. The model includes the effect of fast catalyst deactivation and includes thermodynamic effect like the change in the Gibbs free energy and the effect of thermodynamic equilibrium constants.
Scott (2004)	Laser ablation	Temperature drop from 3500 K to 1500 K in ~ 1 μs	Fullerene	Nickel	Chemical modeling of the formation of carbon/nickel clusters.
Zavarukhin and Kuvshinov (2004)	Isothermal perfect-mixing chemical vapor deposition (CVD) reactor	490-590 ˚C	CH_4/H_2	High-loaded nickel catalyst (90 wt. % Ni-Al_2O_3	Mathematical model explaining formation of nanofibrous carbon and process kinetics involving catalyst deactivation.
Kuwana and Saito (2005)	CVD	700 ˚C (973 K)	Xylene (C_8H_{10})	Ferrocene [$Fe(C_5H_5)_2$], forming iron nanoparticles	Modeling of formation of Fe nanoparticles in an Eulerian coordinate system. Multi-dimensional computational fluid dynamics (CFD) simulation, including mechanism of nucleation and surface growth on an iron particle after bi-particle collision.
Endo *et al*. (2004)	CVD	700 ˚C (973 K)	Xylene (C_8H_{10})	Iron (Fe) particles	CFD model involving two gas-phase reactions and four surface reactions to predict catalytic formation of CNTs from xylene. Inverse calculations were used, using measurements from exhaust gas.

Authors	Mode of synthesis	Temperature of formation	Source of carbon	Catalyst	Modeling approach
D'Anna *et al*. (2001)	Flame synthesis, rich premixed flame	1500-1750 K	Ethylene (C_2H_4)	None	Reaction pathway for nanoparticle formation.
Zhang and Smith (2005)	CVD	500 ˚C (773 K)	Methane (CH_4)	Cobalt (Co)	Model involving the surface catalytic reactions that transfer carbon to solid phase, diffusion of carbon through metal particle, nucleation and growth of carbon nanotubes.
Jourdain *et al*. (2002)	CVD	1080 ˚C	Methane (CH_4)	Ni-Fe	Mechanism of sequential growth, proposed to explain nanotube structure.
Perez-Cabero *et al*. (2004)	CVD	700 ˚C	Acetylene (C_2H_2)	Fe	Kinetic study including surface catalysis model involving catalysis deactivation.
Puretzky *et al*. (2005)	CVD	535-900 ˚C	Acetylene (C_2H_2)	Silicon (Si) substrate with evaporated aluminum-iron-molybdenum (Al/Fe/Mo) multi-layered catalyst	Kinetic modeling of CNT formation and growth on a catalyst nanoparticle. Deals with the growth rate of CNT length with addition of carbon nanoparticles to the surface. Both termination time and termination length were modeled and corresponding scales were proposed. Catalyst deactivation (both due to formation of encapsulating carbon as well as due to deposition of acetylene pyrolysis products on the surface) and reactivation were taken accounted for.
Kuwana *et al*. (2005)	CVD	700 ˚C (973 K)	Xylene (C_8H_{10})	Iron (Fe) particles	CFD model involving two gas-phase reactions and four surface reactions to predict catalytic formation of CNTs from xylene. Detailed model for catalyst deactivation was proposed. Inverse calculations were used, using measurements from exhaust gas. Continuation of work by the same group (Endo *et al*. (2004)).

Authors	Mode of synthesis	Temperature of formation	Source of carbon	Catalyst	Modeling approach
Snoeck *et al*. (1997)	Methane cracking	773-823 K	Methane (CH_4)	Nickel (Ni)	Kinetic model study of carbon filament formation on Ni particle, involving surface reaction, one-dimensional diffusion (Fick's law) and kinetic prediction of coking threshold.
Dateo *et al*. (2002)	High pressure carbon monoxide process	1000-1400 K (appx. 100 atm. pressure)	Carbon monoxide (CO)	Iron pentacarbonyl [$Fe(CO)_5$]	Chemical kinetic models (both detailed and reduced) proposed for surface reactions, iron-carbon cluster formation and carbon nanotube growth.
Villacampa *et al*. (2003)	Catalytic decomposition of methane	550-800 ˚C	Methane (CH_4)	(Nickel-Aluminum oxide) Ni-Al_2O_3 coprecipitated catalyst	Experimental-numerical work, mainly studying the formation of hydrogen by catalytic decomposition of methane. Growth rate model for formation of filamentous carbon also suggested.
Hinkov *et al*. (2005)	DC arc-discharge method	Anode temperature 4000-6500 K and cathode temperature 1840 K	Graphite anode	Ni-Yttrium biocatalyst	Experimental-numerical work, studying the effect of gas pressure on SWNT formation
Gommes *et al*. (2004)	CVD	700 ˚C (973 K)	Ethylene (C_2H_4)	$Fe_x - Co_y$ supported on alumina	Experimental-numerical work consisting of a kinetic study of the effect of the operating conditions of a CVD reactor on the yield of multiwalled carbon nanotubes (MWCNTs)
Yu *et al*. (2005)	CVD	600-650 ˚C	CO/H_2	Silica supported Fe	Experimental work with a proposed rate model for the formation of CNTs. The expression of growth rate is used to explain the effect of particle size qualitatively, but there are no quantitative numerical results.
Kamachali (2006)	CVD	600-650 ˚C (873-1073 K)	C_2H_2	Fe	Proposed theoretical model, compared with a few experimental data points from other sources
Larouche *et al*. (2005)	Plasma torch	1000-1250 K	C particles	Fe/C particles	Solutal Be´nard–Marangoni instability (BMI) theory proposed

Authors	Mode of synthesis	Temperature of formation	Source of carbon	Catalyst	Modeling approach
					for CNT growth using plasma torch method with Fe nanoparticle catalyst

2.2 Previous research on flame synthesis

Besides the work of Singer and Grumer cited above [3], the existence of large carbon shells in soot produced by the vaporization of a graphite disk was alluded to by Zhang *et al*. [34]. However, the literature pertaining to the flame synthesis of CNTs and CNFs remained dormant until Howard *et al.* found evidence of uncatalyzed special fullerene structures and nanotubes mixed with soot agglomerates in specimens extracted from low-pressure premixed benzene or acetylene/oxygen/argon flames [35,36]. Thereafter, Vander Wal *et al*. catalyzed CNT synthesis with metallocene aerosols in nitrogen diluted acetylene and ethylene-air nonpremixed flames [37]. Acetylene was found to provide a tenfold increase of nanotube yield over ethylene. Cooling of the flame was found to be essential for CNT formation, since the absence of nitrogen addition to the fuel resulted in the formation soot aggregates alone. Yuan *et al*. investigated multi wall nanotube (MWNT) formation on a Ni-Cr wire placed in a methane-air nonpremixed flame [38].The largest CNT harvest was in the soot-laden region of the flame at ~1500K. They suggested that PAHs deactivate the Ni catalyst particles. The role of radical decomposition has also been discussed by Merkulov *et al*. [39]. In a subsequent investigation Yuan *et al*. reported CNT synthesis in ethylene-air nonpremixed flames established with and without nitrogen dilution [40]. A baked stainless steel (SS) grid with Fe, Cr, and Ni oxide deposits on its surface was employed as a catalyst substrate. Nitrogen addition straightened the tubes, and this was attributed to lowering of the

ambient temperature. The undiluted flame temperature in the investigation was 1547ºC while the nitrogen diluted flame temperature was ~1244ºC.

Vander Wal and coworkers considered CNT and CNF formation in $CO/H_2/He$ and C_2H_2/H_2 nonpremixed "pyrolysis" flames (that had an insufficient air supply for complete oxidation), and their corresponding synthesis in a furnace [41,42,43,44]. They employed aerosols consisting of either nickel or iron nitrates. Iron was found to be active in CO mixtures and Ni with C_2H_2. Their results also showed that while the catalyst particle composition and morphology controls the CNT structure and its growth rates, the reactant gas composition plays a deciding role in their formation. While small ~1 nm Fe nanoparticles were found to be active, they determined that Ni particles must be ~5 nm to be active in the flames. They attributed the CNT growth mechanism to either carbon/solvation/diffusion/precipitation base growth [45,46,47] or *yarmulke*-like [48] growth.

Merchan-Merchan *et al*. observed uncatalyzed [13] and catalyzed [14] CNT formation in CH_4-air/O_2 nonpremixed counterflow flames. They suggested that oxygen-induced hydrocarbon pyrolysis is required for CNT synthesis, but the exact growth mechanism remained undetermined. They attributed the presence of various carbon nanoforms to spatial variations in temperature and chemical species concentrations in the flame environment. Sen and Puri [1] and Arana *et al*. [2] also demonstrated that the flame synthesis of aligned CNTs and CNFs is possible on a variety of substrates. Height *et al*. [11] used a premixed acetylene flame in an axial flow using Fe (derived from $Fe(CO)_5$ vapors) as catalyst.

Lee *et al*. [49] synthesized Ni-catalyzed multiwalled CNTs and CNFs on a substrate using an ethylene inverse nonpremixed flame as the source of heat and gaseous hydrocarbon species. Pan *et al*. [50] used an ethanol-air flame and a Ni-based substrate to produce a mixture of CNTs and CNFs, and a carbon steel and low alloy steel substrate to produce mainly CNFs. They proposed intuitive models for the formation of hollow-cored CNTs and solid-cored CNFs, but their model was conceptual and based on pictorial representations. Nakazawa *et al*. [51] reported an experimental study on the formation of carbon nanotubes in a wall stagnation flow. They introduced a nickel-coated stagnation plate made of ceramic into a fuel-rich ethylene-air mixture above a burner which produced a trumpet-shaped flame and observed the formation of CNTs at a temperature of 650 K. Tsantilis *et al*. [52] suggested a population balance model of flame synthesis of titania (TiO_2) nanoparticles that can be extended to carbon nanoparticle formation.

2.3 Previous research on surface alteration using carbon deposition

Very little work is reported on alteration of surface hydrophobicity properties via carbon deposition using a flame. Our work described in Section 3.2.2 is one of the first to achieve that. Low surface-energy materials, such as amorphous carbon (a-C) films [53], are frequently used to modify surfaces in order to control their wettability. Here, we present a technique for the rapid deposition of a superhydrophobic a-C layer consisting of uniform carbon nanobeads on a Si substrate using a coflow ethylene-air nonpremixed flame. The flame conditions have been described in detail previously [1,2]. The nanobeads are morphologically similar to the carbon nanopearls synthesized by Levesque and co-workers [54] through acetylene dissociation at 700ºC on nickel catalyst nanoclusters.

CHAPTER 3

EXPERIMENTAL SETUP AND CNS SYNTHESIS

3.1 Experimental Setup

The burner used to establish the flame for synthesis of carbon nanostructures is shown in Figure 3.1.1. A detailed illustration of the burner and its components has been provided in Appendix I. We used ethylene (99.5% purity) obtained from Airgas, Inc. (EY CP20) as the fuel. The air source was Breathing Grade E Size 300 16PK CGA 346 (also from Airgas, Inc. – AI BCS3C058). The substrates were placed upon the flat flame 10 mm above the burner. The axisymmetric burner consisted of two concentric tubes of 11.1 and 101.6 mm inner diameters. The fuel flow rate was 4.6 cm^3/s (≈276 cm^3/min), and the outer airflow was 713.3 cm^3/s [1,2]. The burner has an annular cover of ceramic honeycomb and has glass beads inside the outer tube, which help in making the flow velocity uniform (by avoiding the top hat profile) as much as possible, to make the flame stable. The flame height is controlled not to exceed 70 mm. The flame temperature was ≈1550ºC. The images of the carbon nanostructures were obtained with a LEO 1550 Field Emission Scanning Electron Microscope (FE-SEM) and a Philips Transmission Electron Microscope (TEM). The flow rates of fuel and air passing to the burner were controlled and measured using gas flow controllers fitted with digital meters. Omega FMA-1610A and Omega FMA-1619A air flow meters were used to measure air flow and fuel flow rates respectively. Details of the surface characterization equipment are provided in Appendix IV.

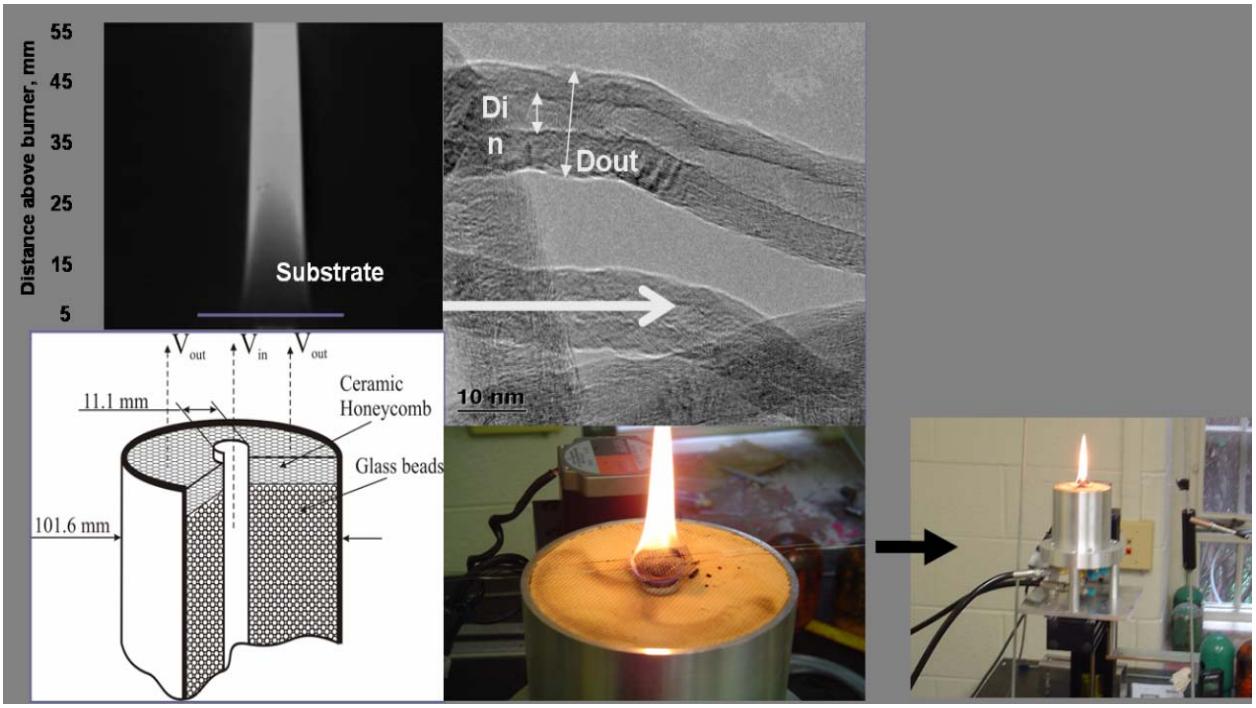

Figure 3.1.1 Experimental setup for flame synthesis of carbon nanostructures

3.2 Results

3.2.1 Flame synthesis of carbon nanostructures

Figure 3.2.1(a) and Figure 3.2.1(b) show SEM images of carbon growth on an iron substrate after 5 and 10 minutes, respectively, at 4 mm height above the burner (thorough the procedure described in Refs. 1 and 2). The five-minute specimen consisted of carbon nodules and no CNTs/CNFs are visible. In contrast, the 10 minute specimen consists of both the nodules and carbon nanofilaments of various diameters. These were grown on Fe wires of 0.1 mm diameter. Although carbon deposition occurs early on, filamentous carbon separation, which forms CNTs/CNFs, is not discernible before a critical time. Our simulation results also show that the rate of filamentous carbon deposition increases over a period and tends to assume a larger almost constant value later on. Figure 3.2.2(a) shows a lower magnification view carbon nanostructures deposited on a stainless steel (SS) wire exposed to the abovementioned ethylene flame for 10 minutes. Figure 3.2.2(b) is shown in order to compare the same structure of the wire surface (at the same magnification) for an exposure time of 15 minutes. The images clearly show the variation of surface structure with change in the exposure time. While the surface still shows the presence of some carbon fibers from a side view after an exposure time of 10 min, it seems to be seriously affected by the deposition of carbon and thermal degradation after an exposure of 15 min.

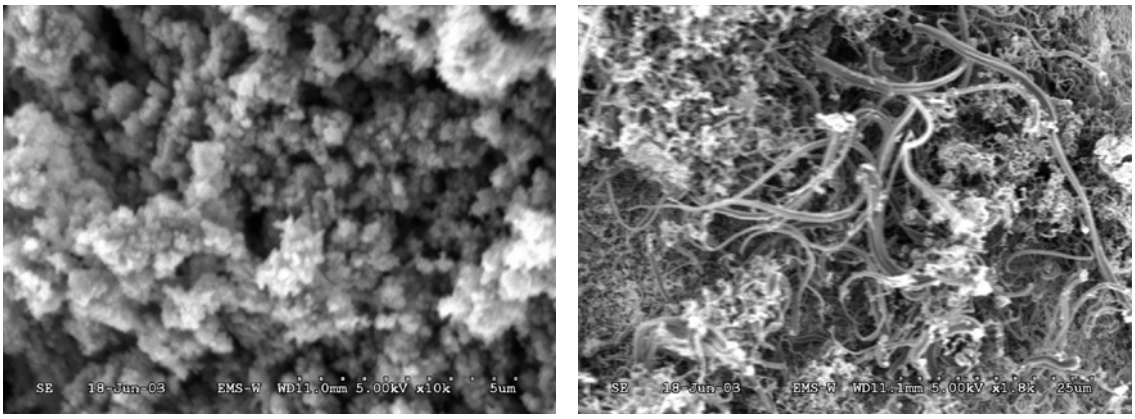

(a) 5 minutes (b) 10 minutes

Figure 3.2.1 SEM images of carbon deposited on an Fe wire substrate after (a) 5 min and (b) 10 min exposure to flame

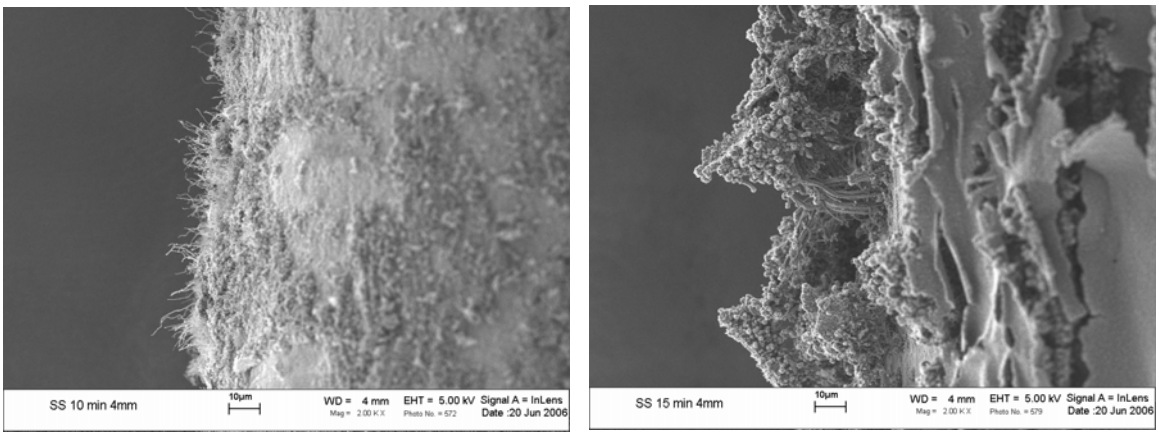

(a) 10 minutes (b) 15 minutes

Figure 3.2.2 Zoomed out SEM images of carbon deposited on an Fe wire substrate after (a) 10 min and (b) 15 min exposure to flame

Figure 3.2.3 below shows SEM images of carbon nanotubes grown on a Ni wire substrate. The wires were introduced in the flame described above at a height of 4 mm above the burner top. Figure 3.2.3(a) shows the carbon nanostructures typically observed after 10 min of exposure to the flame and Figure 3.2.3(b) shows the same for 15 min. Additional representative images are shown in Appendix II for the same two conditions described above using Ni wire catalyst. The major reason for showing these is to stress on the fact that using Ni, flame synthesis can be used to obtain relatively pure CNTs/CNFs compared to Fe, which yields a mixture of nanospheres, nanobeads, CNTs and CNFs. Figure 3.2.4(a) and (b) show carbon nanostructures grown on silicon (Si) substrates coated with ferrofluid. The exposure times were 5 min and 10 min respectively. Si substrates were dip-coated with ferrofluid and the carrier medium (water in this case) was allowed to evaporate, leaving behind Fe nanoparticles on the surface of the Si disc. These deposited nanoparticles then acted as catalyst to CNT/CNF growth in the flame. Figure 3.2.5(a) and (b) show lower magnification views of the structures flame-deposited on such a substrate. This technique, although adopted for a faster and more efficient growth of CNTs/CNFs, came with the existence of some impurities, mostly incorporated due to the surfactants that are used to coat the magnetite (Fe_3O_4) particles in the ferrofluid. These surfactants (also called dispersants) are used to prevent the ferrofluid particles from clumping together. A result of such impurities can be found in Figure 3.2.5(b).

Figure 3.2.6(a) shows an SEM image of the carbon nanostructures (along with crystal impurities) deposited on a ferrofluid-coated Si disc. Figure 3.2.6(b) and Figure 3.2.6(c) show EDS spectra corresponding to regions 1 and 2 respectively in Figure 3.2.6(a). These spectra are raw data reported from the EDS analyzer on the LEO (Zeiss)

1550 FE-SEM (Refer to Appendix IV). As can be observed from the spectra, for region 1 (which corresponds to the ribbon-like crystal growth), there is almost no carbon (C) present. Instead, there is an abundance of sodium (Na) and oxygen (O). A substantial amount of iron (Fe) is also observed. Region 2, on the other hand, shows an abundance of C and Fe, as expected. Na is typically derived from a Na salt of sulfonated octadecyldiphenyl ether (i.e., a surfactant having an alkylpolyphenyl structure). Such Na salts are very common dispersants in ferrofluids. As such, these are also deposited on the Si discs once the carrier medium evaporates. These, when exposed to the high temperature and possible oxidation in the flame, lead to the formation of oxides. As such, impurities in the form of Na-containing salt crystals (exact composition unknown) as well as iron oxide crystals are found on the Si discs coated with ferrofluid. The iron is also deposited basically as magnetite nanoparticles and as such prone to oxidation in the flame environment to form crystal-like structures of their oxides. A complete study of these impurities and their effect on the structures formed during flame synthesis requires detailed analytical chemistry and is beyond the scope of this study. We coated a stainless steel wire mesh substrate with ferrofluid and exposed it to the abovementioned flame for 10 minutes, which gave us the results shown in Appendix II.

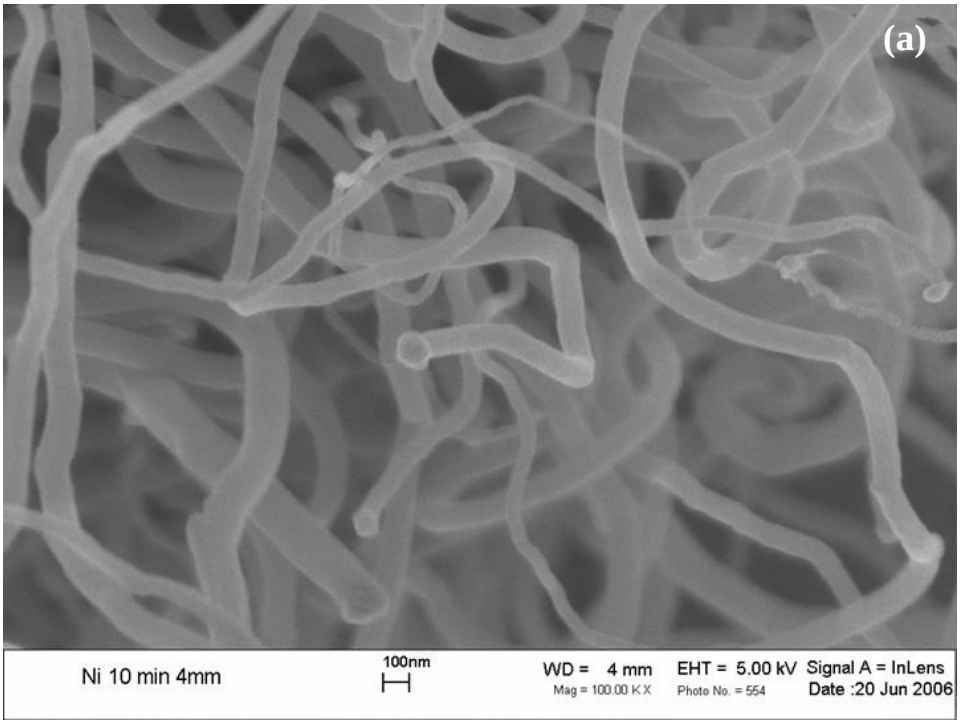

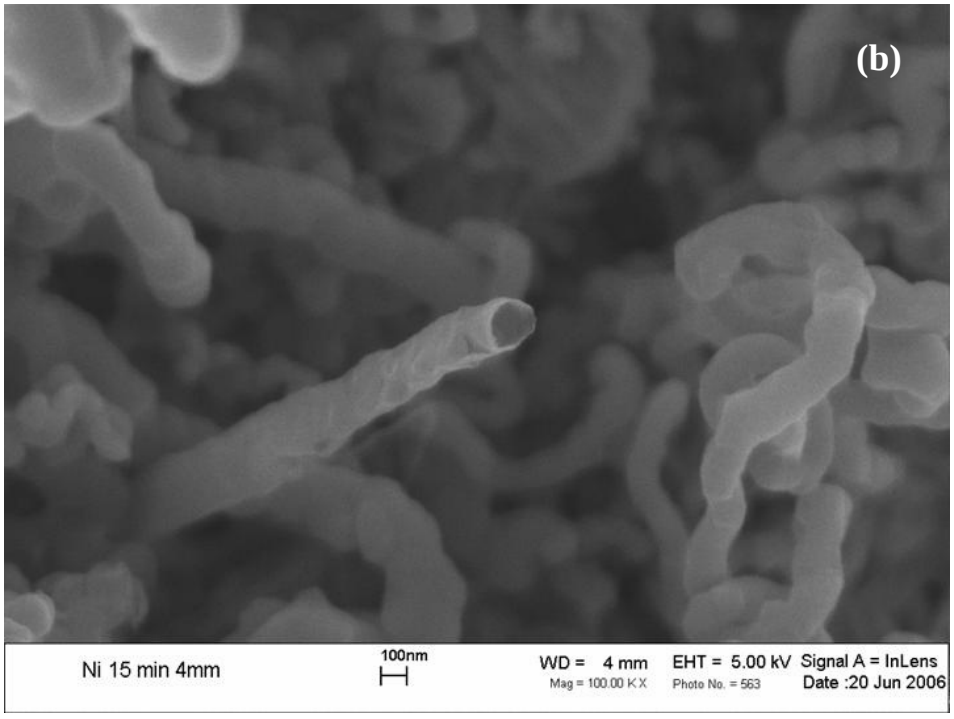

Figure 3.2.3 Carbon nanotubes flame synthesized on Ni wire catalyst

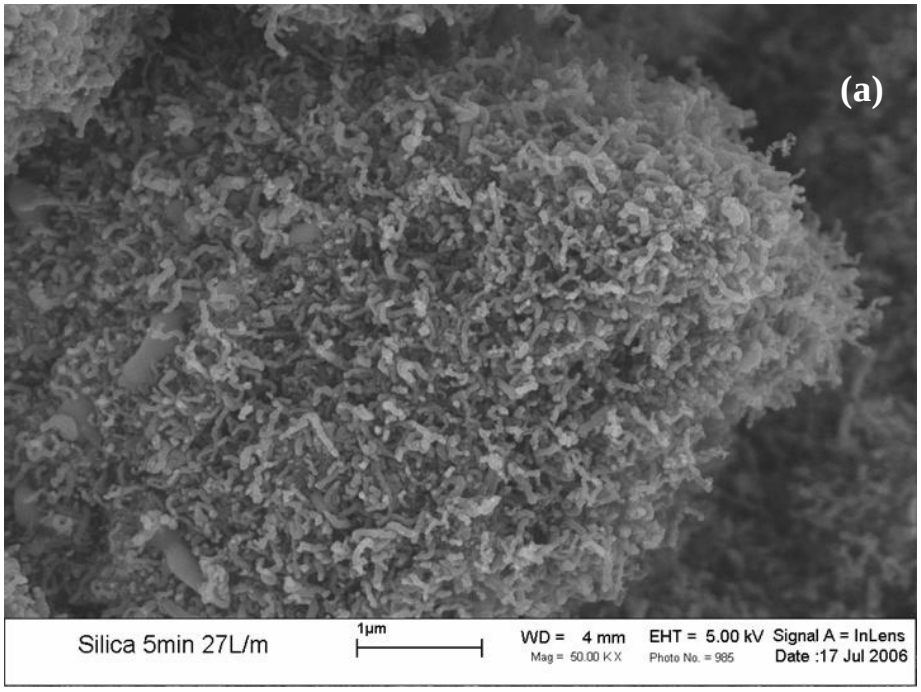

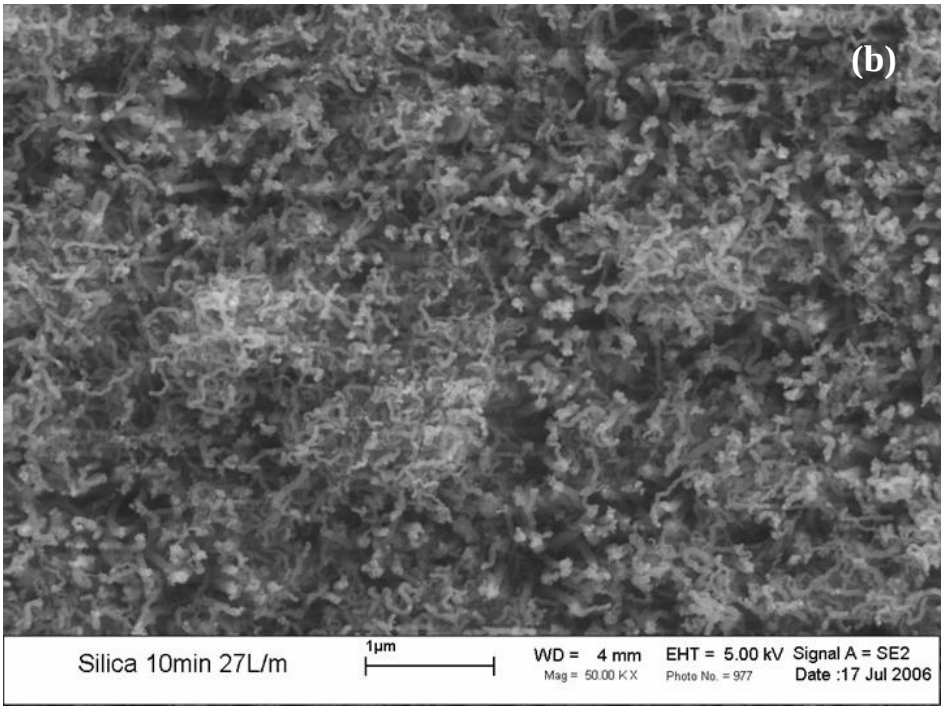

Figure 3.2.4 Carbon nanofiber growth on Si disc coated with ferrofluid catalyst at (a) 5 minutes and (b) 10 minutes of exposure time

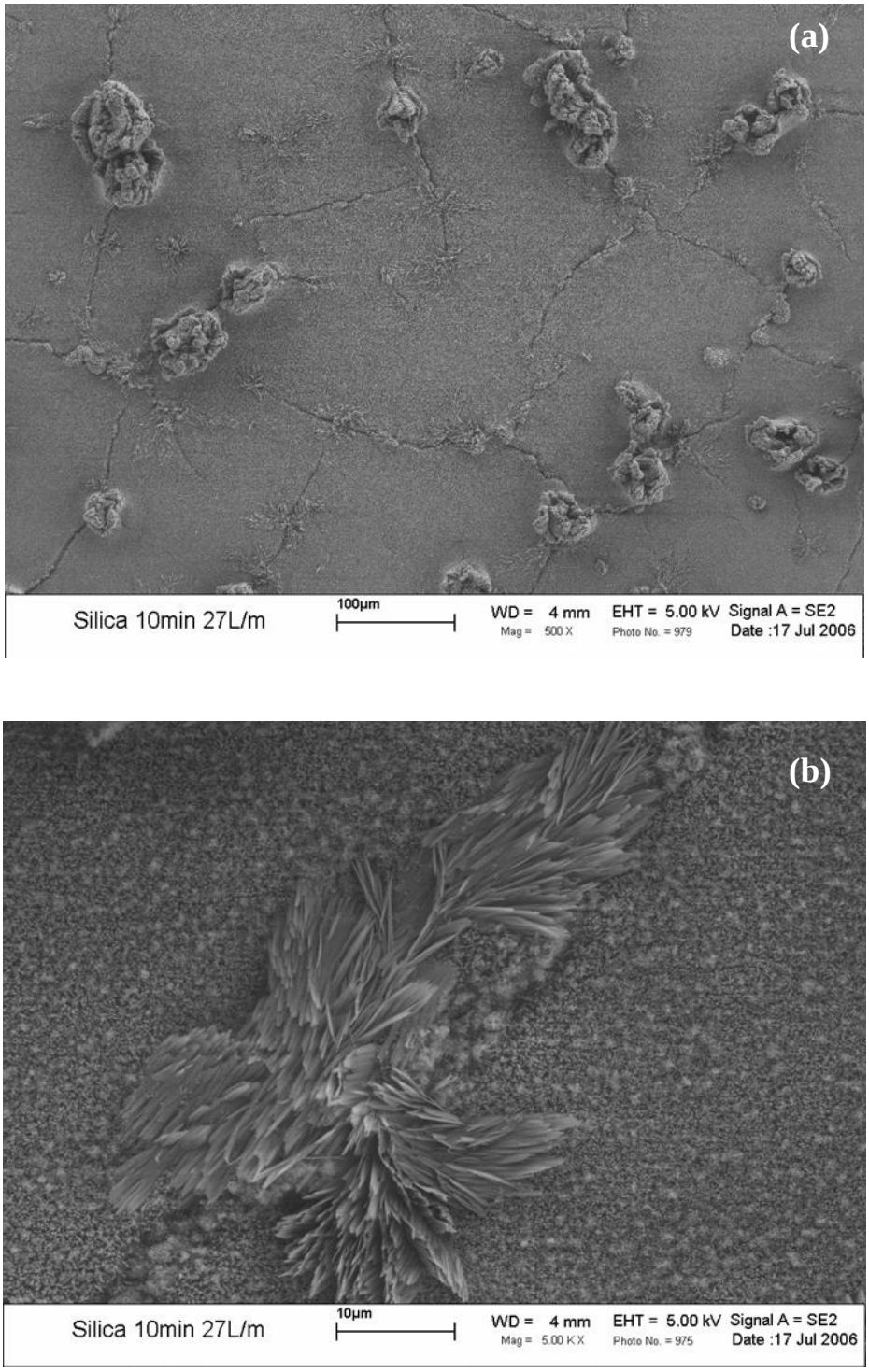

Figure 3.2.5 (a) Lower magnification view of carbon nanofibers synthesized on ferrofluid-coated Si disc and (b) crystal impurity derived from the ferrofluid dispersant

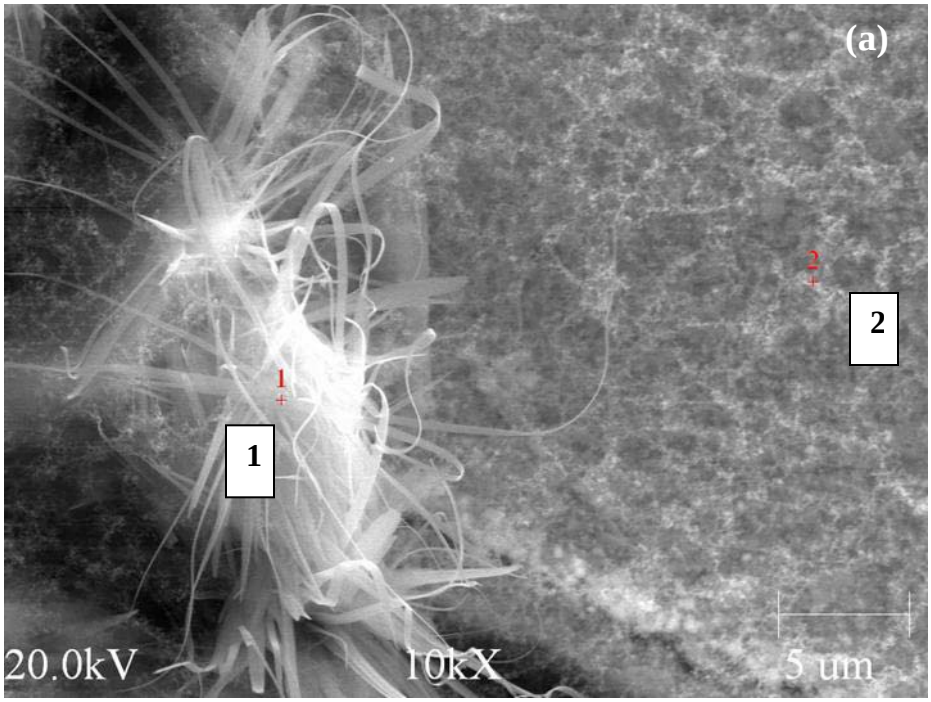

Si wafer-1

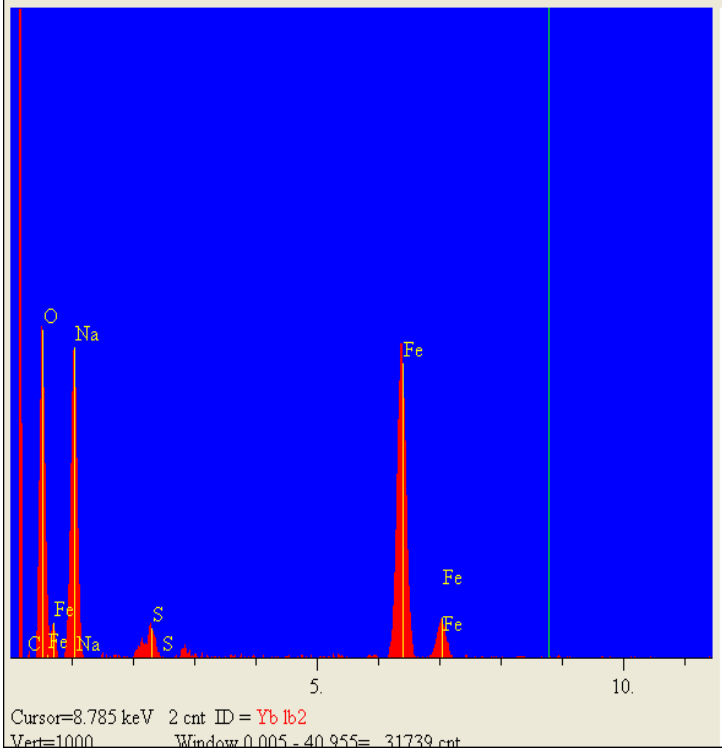

(b)

Elt.	Intensity (c/s)	Atomic %	Conc	MDL 3-sig	
C	0.00	0.000	0.000	0.000	
O	114.58	49.497	30.716	0.657	
Na	121.56	30.654	27.334	0.393	
S	14.53	1.131	1.406	0.217	
Fe	180.50	18.718	40.544	0.352	
		100.000	100.000		Total

kV	20.0
Esc	On
Sum Peak	Off
Elapsed Livetime	45.0

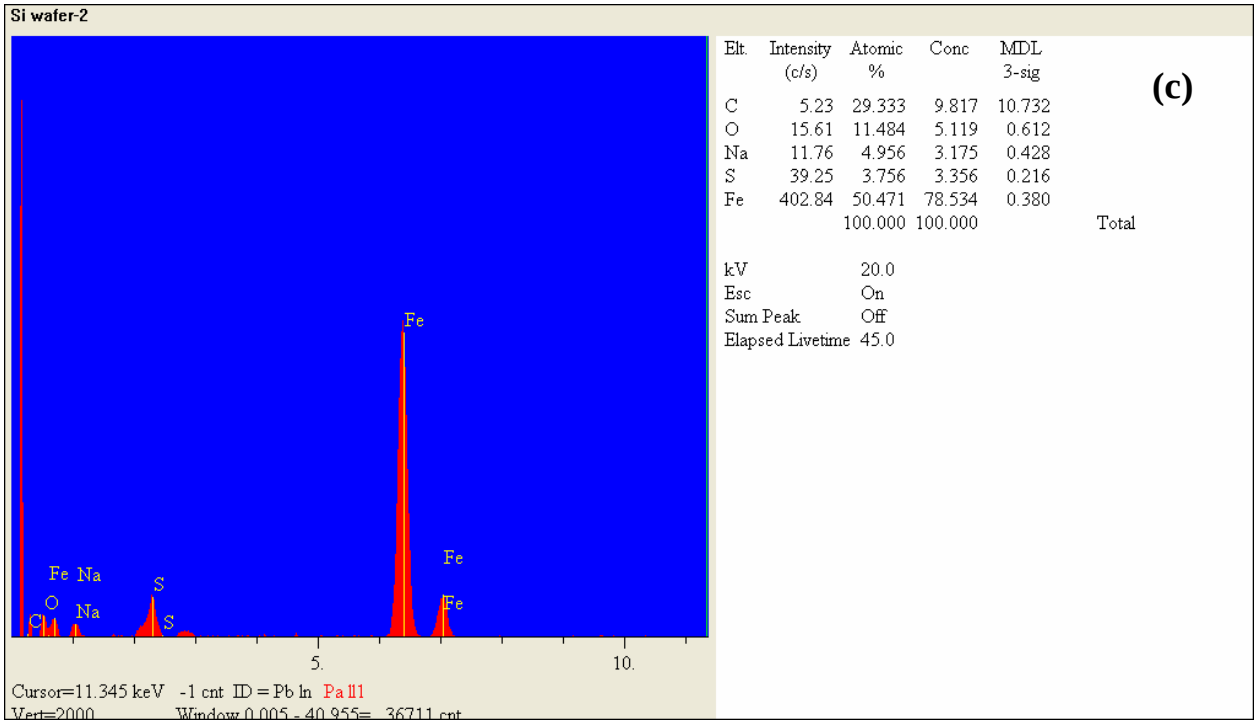

Figure 3.2.6 (a) SEM image of deposition on ferrofluid-coated Si disc, (b) EDS spectra of elements in region 1 and (c) EDS spectra in region 2

3.2.2 Altering surface wettability using flame synthesis

A flat flame that stagnated against the silicon wafer was used as the carbon source to grow the a-C nanobeads [55], as shown in Figure 3.2.7(a). The carbonaceous material was deposited on the Si disc in three zones. A central gray circular deposition region produced at the center was surrounded by a brown annular zone, which in turn was enveloped by an outer black sooty region (Figure 3.2.7(b)). The carbon coating exhibited superhydrophobic behavior from the disc center until the boundary between the brown and the black sooty regions. This superhydrophobicity is readily inferred from the microscope images presented in Figure 3.2.8, which show ≈2 mm water droplets placed at various radial locations on substrates coated with 2.5, 5 and 7.5 min nanobead deposits. While the nanobead film deposited on the disc can be easily wiped off, it does not fall off by itself when the disc is tilted or even turned upside down. The surface hydrophobicity has been observed to be very stable over a period of six months.

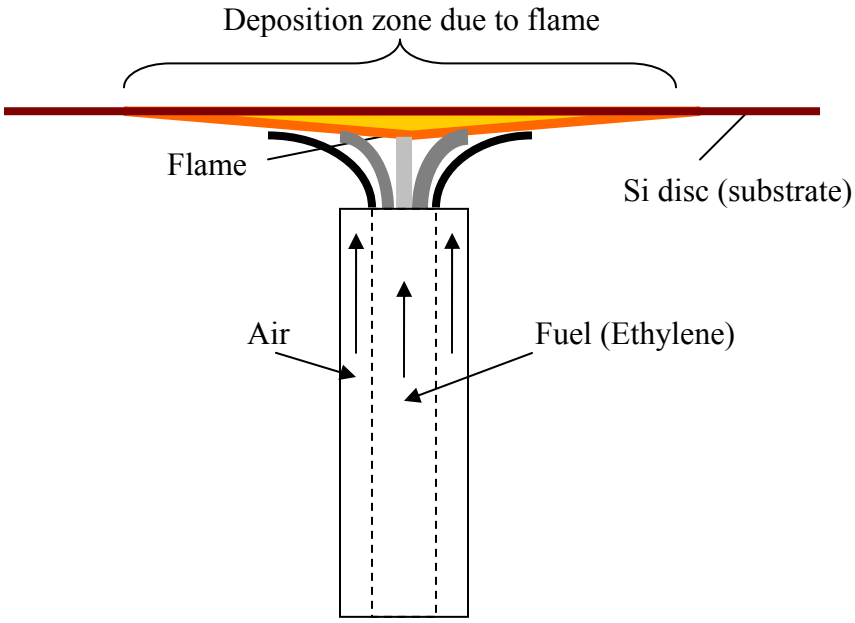

(a)

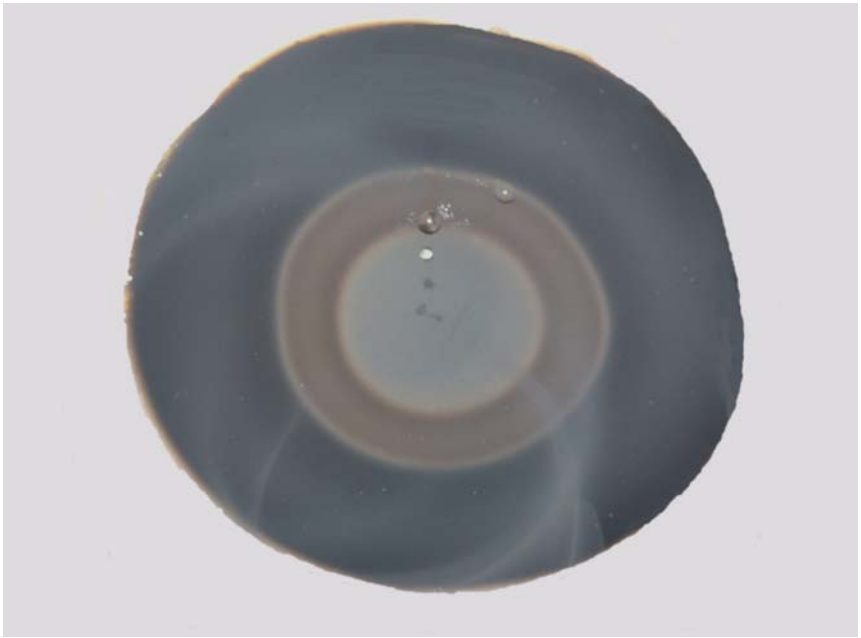

(b)

Figure 3.2.7 (a) Schematic of the carbon nanopearl synthesis process. (b) A Si disc with a carbon nanostructure coating after 5 min exposure to the flame.

The external contact angle θ (schematically described in Figure 3.2.8(a)) lies in the range 152.4º–157.1° for all cases. A similar water droplet placed on an untreated silicon surface has an external contact angle of 40.8°, as shown in Figure 3.2.8(e), confirming that the uncoated wafer surface is hydrophilic. Contact angles in excess of 150° offer evidence of superhydrophobic behavior [56].

The exposure time of the disc to the flame influences the area of the nanobead deposit. Nanobead deposits were investigated for three exposure times – 2.5, 5 and 7.5 minutes. The superhydrophobic behavior of the nanobead coating extends from the center of the disc (radius≈0) to a ≈25 mm radius (Figure 3.2.8(b)) for the 2.5 min sample. The radius over which hydrophobicity is exhibited decreases with increasing flame exposure time. The 5 min sample exhibits hydrophobicity from the disc center up to a 23 mm radius, while for a 7.5 min sample this is observed until a smaller radius of 20 mm (cf. Figure 3.2.8(c) and Figure 3.2.8(d)). As the flame exposure time of the Si disc increases, the outer sooty region covering moves towards the disc center, thereby decreasing the area of the superhydrophobic nanobead region.

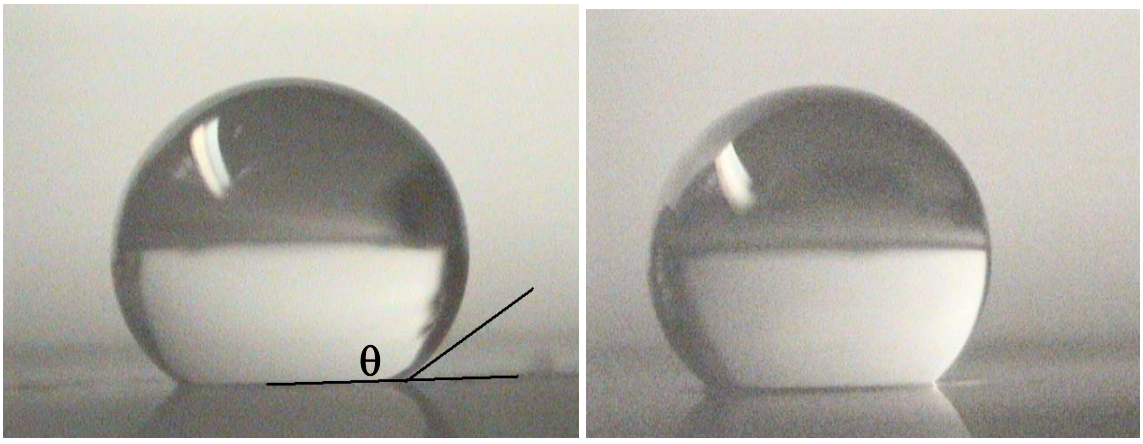

(a) (b)

(c)

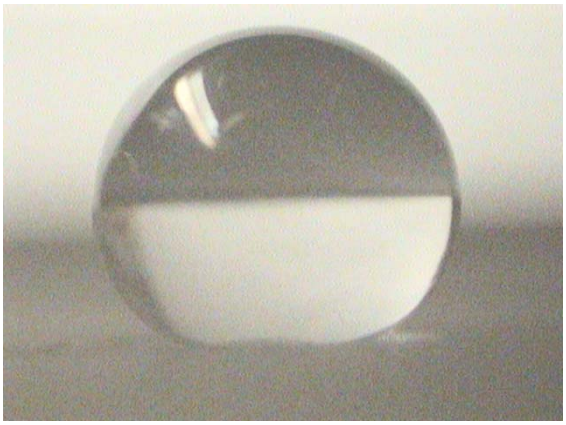

(d)

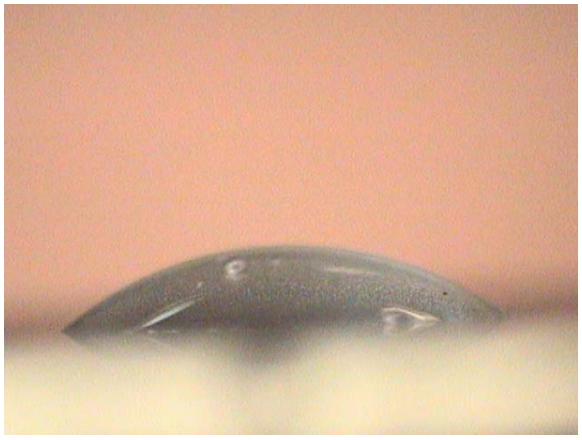

(e)

Figure 3.2.8 Images of 2 mm (appx.) water droplets placed on a Si disc containing a nanobead deposit following a 2.5 min exposure to the flame at radii of (a) 10 mm (showing the contact angle θ) and (b) 25 mm. Images of 2 mm (appx.) water droplets placed on a Si disc containing a nanobead deposit at a radius of 10 mm after (c) 5 and (d) 7.5 min exposures to the flame. (e) Image of a water droplet placed on a wafer that was not exposed to the flame.

Figure 3.2.9 illustrates the superhydrophobic region on the Si surface. Figure 3.2.10(a)-(d) present SEM images of a 5 min carbon deposit obtained at the disc center and at 9 mm, 20 mm and 43 mm radii removed from it, respectively. There is a significant difference in the surface structures presented in Figure 3.2.10(a), (b) and (d).

The disc center and the 9 mm radial position, both of which are superhydrophobic, have closely packed spongy nanobeads that generate nanoscale surface roughness. On the other hand, at a 43 mm distance from the disc center, nanobeads are scarce and most of the region appears to be coated with smaller soot globules that produce very little nanoscale surface roughness. As a result, this portion of the deposit is highly hydrophilic. A drop of water placed at such locations smears the surface almost immediately. In contrast, the water droplets roll off very easily from the flame-synthesized nanobead substrates closer to the center, even with slight tilting of the disc.

Figure 3.2.10(a) presents an image of the central grayish region (refer to Figure 3.2.7(b)) for a 5 min sample. Morphologically, these resemble the spongy nanobeads with typical diameters of 100–150 nm as reported in Ref. [54]. Our synthesis method, however, produces individual nanobead structures ranging between 20 and 50 nm that assemble together to form larger chainlike structures. A similar structure is also apparent in the brown annular region, as shown in Figure 3.2.10(c).

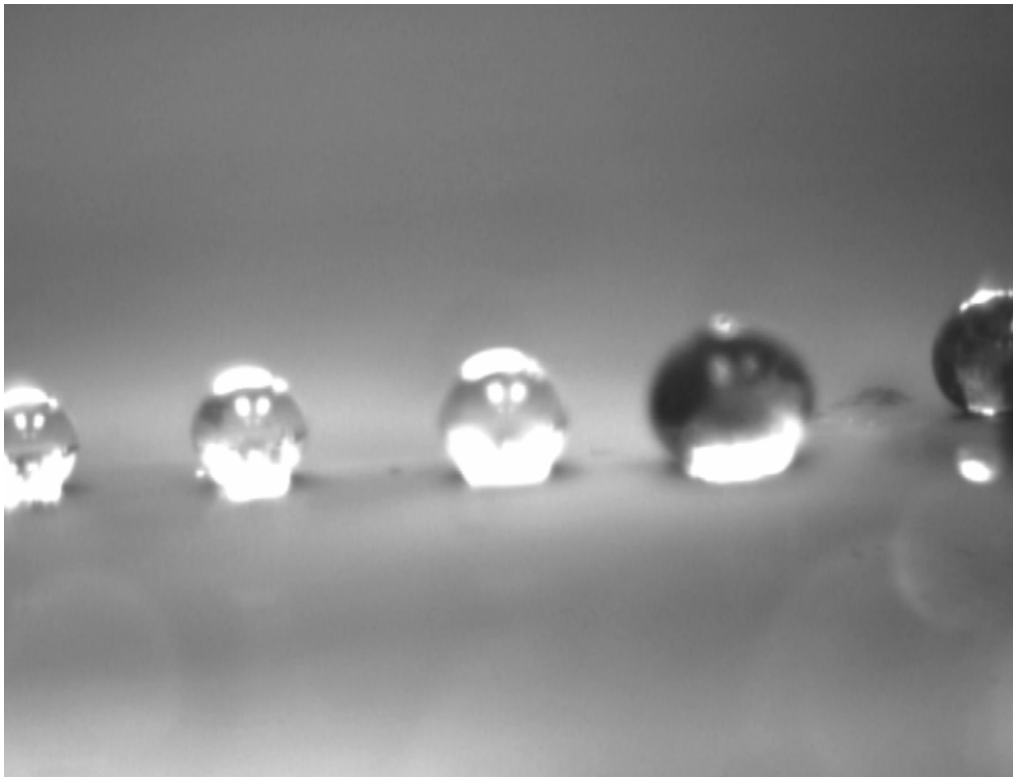

Figure 3.2.9 Droplets lined up on the surface of a Si disc with hydrophobic nanopearl coating on it

Zhou *et al.* [57] have discussed the wettability (ranging from hydrophilic to superhydrophobic) of amorphous carbon films that were deposited by magnetron sputtering on silicon and glass substrates at different temperatures. They reported an increase in the water contact angle (hence hydrophobicity) with increasing deposition temperature and attributed the cause partially to the presence of graphite-like porous structures that were produced at elevated temperatures. Wang and Kang [58] also synthesized smooth, nonporous solid carbon nanospheres by decomposing CH_4 at 1100°C with mixed-valent (rare earth metal) oxide-catalytic carbonization. The spheres were formed on the wall of the reaction chamber and had an average diameter of 210 nm

and consisted of partially ordered carbon flakes in the 1–30 nm size range, but were not aggregated.

The structure of a surface has a profound effect on its wettability [57,59]. Pozzato *et al*. [59] stated that when water droplets (1) form very large contact angles in excess of 150° on superhydrophobic surfaces and (2) show very low hysteresis allowing the drops to easily roll off the surfaces, they exist in the Cassie equilibrium state [59]. A water droplet in such a state sits on the asperities of the surface while air is entrapped in the structure below these. The other superhydrophobic equilibrium state is the Wenzel state [59] during which water penetrates into the rough surface cavities. Although very large contact angles can also be achieved in this state, there is large hysteresis. Thus, the droplets do not roll off as readily but tend to stick to the surface. As the SEM images in Figure 3.2.10(a), (b) and (c) show, the flame-synthesized nanobead substrate offers a very closely packed structure due to its nanoscale dimensions. This makes it unlikely that water droplets can penetrate the asperities of the surface. Consequently, air is most likely entrapped below the droplets placed on the nanobead substrates so that they exhibit superhydrophobicity in the Cassie equilibrium state.

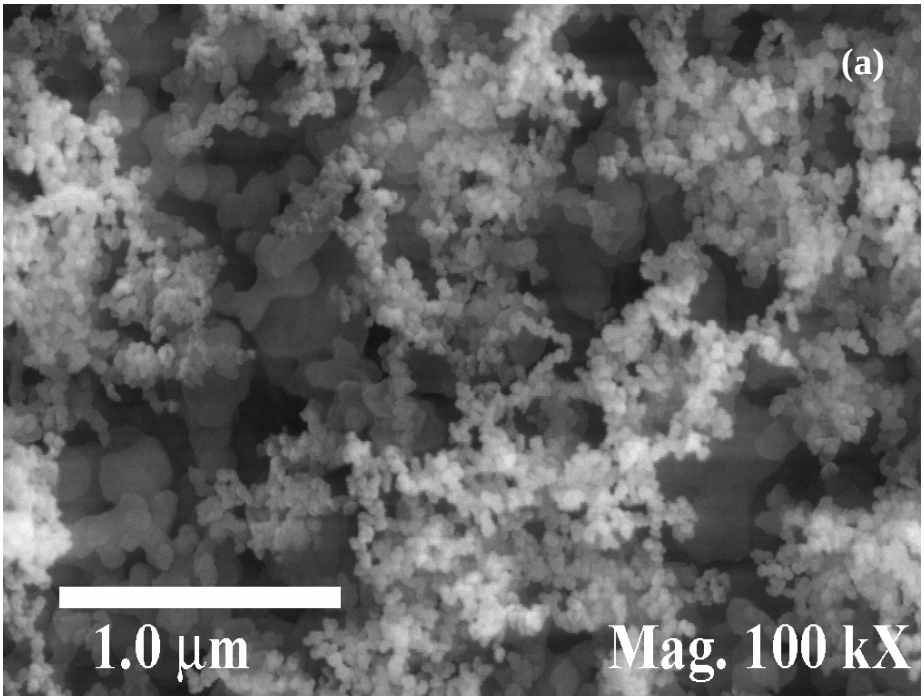
(a)
1.0 μm
Mag. 100 kX

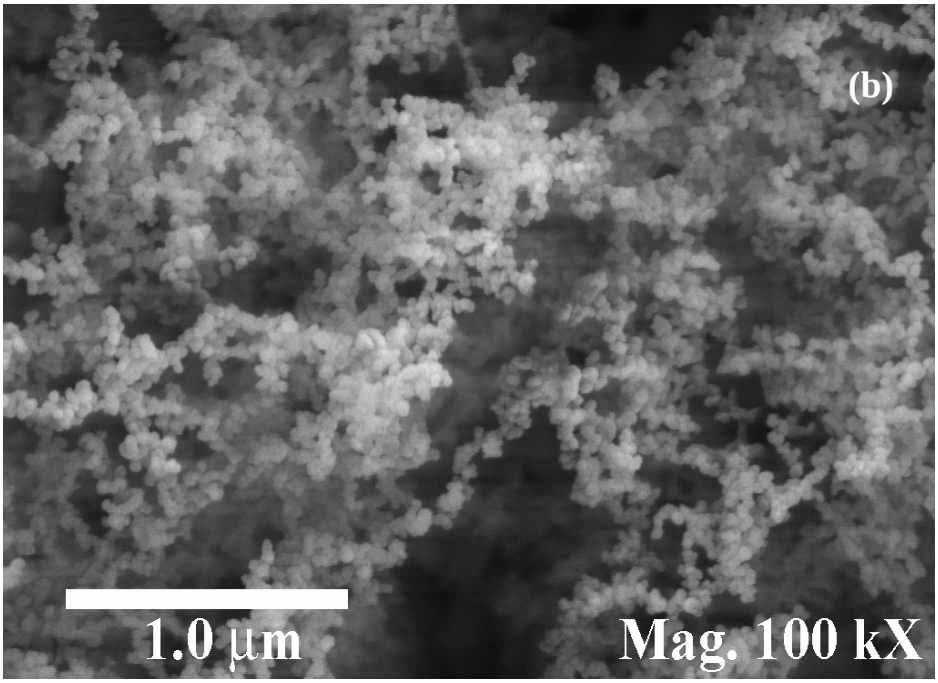
(b)
1.0 μm
Mag. 100 kX

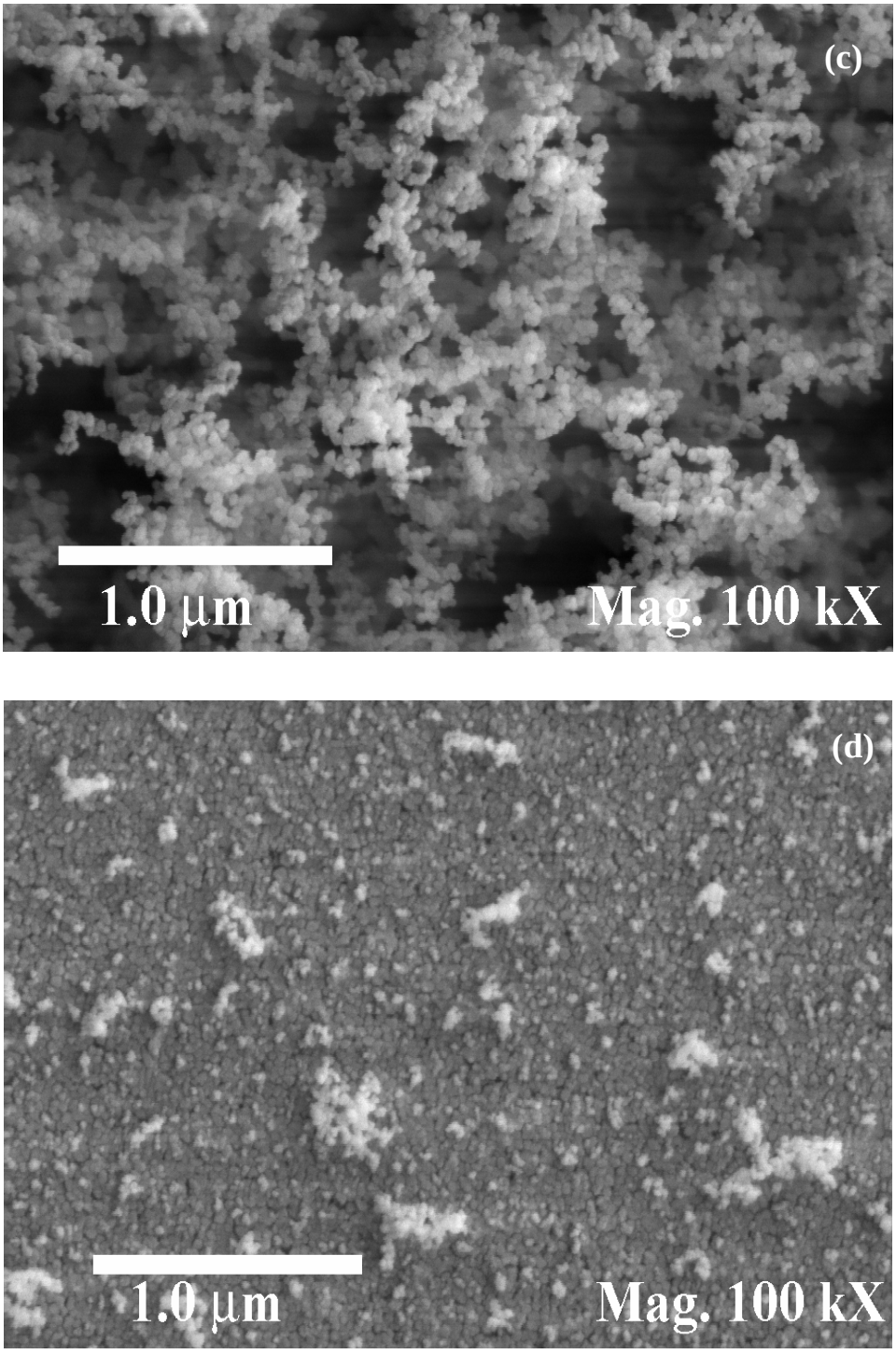

Figure 3.2.10 SEM images obtained for a 5 minute sample at (a) 9 mm from the disc center and (b) 43 mm from the disc center; SEM images of nanobead grown for 5 minutes on a silicon disc (c) at the central region and (d) at 20 mm radius

TEM images, presented in Figure 3.2.11 for a Si substrate exposed to the flat flame for 5 min, show that the carbon nanobeads are connected to one another. Since the deposition process for the nanobeads is not catalytic, we hypothesize that the growth is a result of gas-phase fuel pyrolysis during combustion. The pyrolysis products are transported into the stagnation layer adjacent to the relatively colder Si surface on which they condense and form nanobeads. (Pyrolysis is dominant in the fuel core, while oxidation occurs outside the flame sheet. Soot formation occurs in the proximity of the flame sheet on the fuel side, since a small amount of oxygenation below a critical value promotes soot precursors [60].)

Sharon *et al*. [61], who were the first to produce carbon nanobeads, found that it is desirable to have a carbon source that contains a combination of sp^2 and sp^3 bond structures. They stated that a pure sp^2 source such as graphite makes the formation of spherical structures very difficult. They synthesized spongy carbon nanobeads by pyrolyzing camphor vapor at 1000°C in an argon atmosphere using ferrocene as a catalyst and produced both solid and hollow carbon nanobeads of two sizes, ~ 250 nm and 500–800 nm. These consisted of amorphous layers that were covered by graphitic shells. Electron energy-loss (EEL) spectral analysis showed that the inner portions of the beads were amorphous, which they concluded was the result of camphor pyrolysis [61]. They observed that the larger beads aggregated, with 10 or more being interconnected by an outer shell and an outer covering of fibrous graphitic carbon.

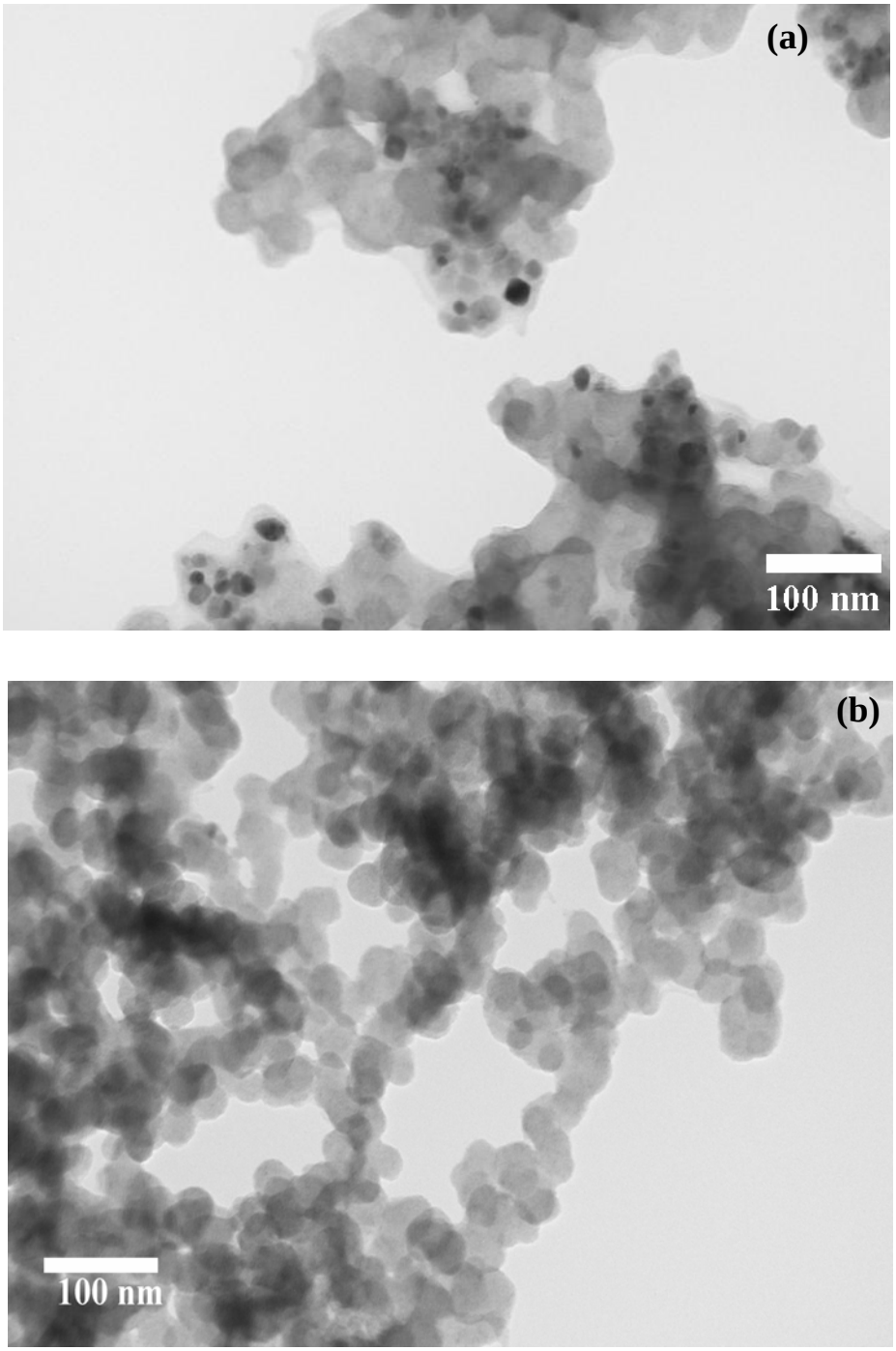

Figure 3.2.11 TEM images of the (a) nanobead-containing and (b) sooty regions of the disc

X-ray Photoelectron Spectroscopy (XPS) of the flame-synthesized surface deposit was performed to characterize the carbon coating. The resulting C1s spectrum from a magnesium (Mg) energy source is presented in Figure 3.2.12. The sp^2 and sp^3 spectra were curvefit onto that obtained from the sample. They were fitted with two Gaussian curves on a Shirley background [62] with the binding energies centered around 284.5 and 285.4 eV, corresponding to sp^2-bonded and sp^3-bonded carbon, respectively. The peaks for the two samples are very similar and occur at ≈285 eV. The sp^2 to sp^3 ratios of the as-deposited films were calculated from the relative intensities deduced from the curve-fitting. Each of the components is a convolution of a Gaussian and a Lorentzian convolution [62], since the sp^2 and sp^3 hybridized carbon bonds correspond to a combination of these convolutions as discussed by Diaz *et al*. [63]. The entire range of the photoelectric spectrum is also shown for the nanobead and outer black sooty regions in Figure 3.2.12(c). Analysis of the various spectra indicates that the nanobead region contains 98.1% carbon by volume with a similar 97.5% carbon content in the sooty region. While the carbon content is similar, the corresponding nanostructures are different as shown in Figure 3.2.12(a) and (b).

Hydrophobic a-C films have been reported to contain a 50-71% sp^2 hybridized structure [57]. The flame-synthesized nanobead-containing surface of the disc had 55% and the sooty region 53.3% sp^2 hybridized carbon, i.e., the sp^3/sp^2 ratio for the two regions was ≈0.82 and ≈0.87 (as shown in Figure 3.2.12(a) and (b)), respectively. An sp^2 structure pertains to planar hexagonal graphitic rings while sp^3 is the tetrahedral structure that is present in diamond. In order to form three-dimensional concentric spheres, the conversion of sp^2 C-bonds into sp^3 bonds is required. The relatively large presence of sp^3

bonds explains the preponderance of the spherical spongy nanobead structures. The absence of a catalyst as well as nearly equal distribution of sp^2 and sp^3 hybridized structures leads us to believe that these spongy structures are, in fact, overwhelmingly amorphous in structure. These results and the SEM images of Figure 3.2.12(a) and (b) show that the nanobead structures are also present in the sooty region, although with a much lower surface density. Figure 3.2.12(c) shows the complete spectra for the nanobead region.

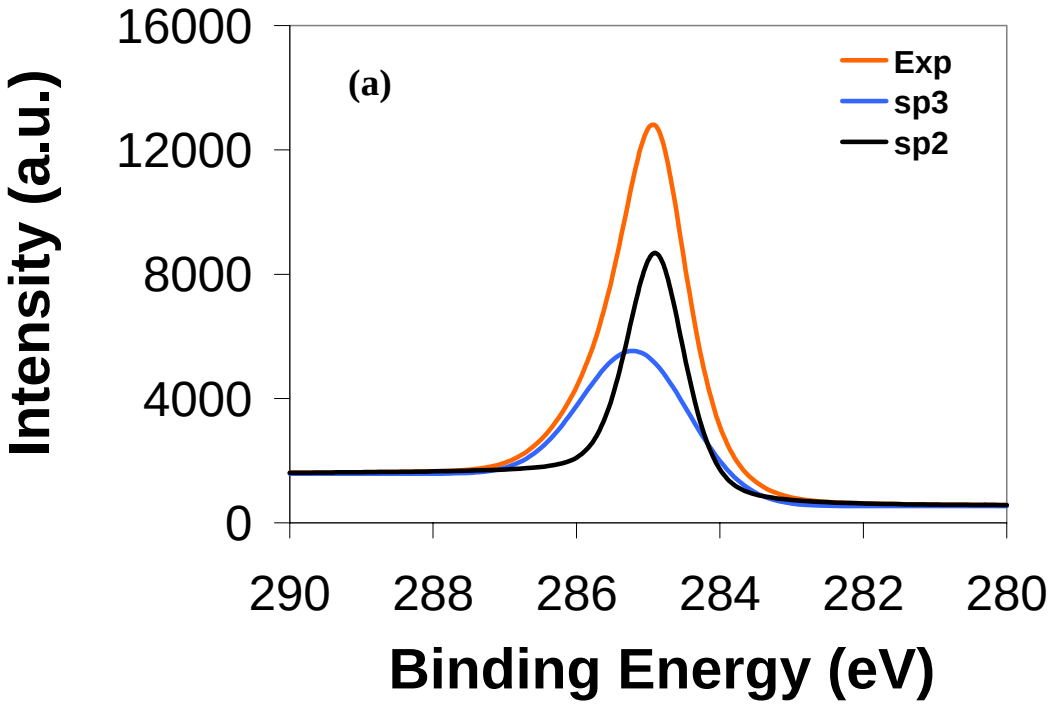
(a)
Exp
sp3
sp2
Intensity (a.u.)
16000
12000
8000
4000
0
290
288
286
284
282
280
Binding Energy (eV)

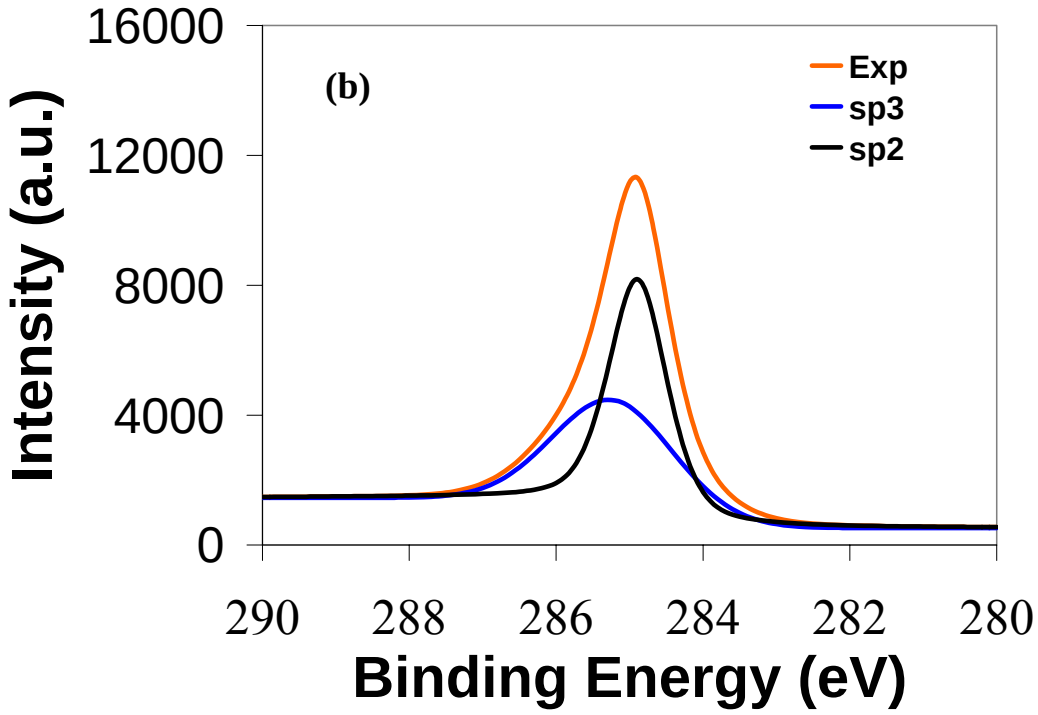
(b)
Exp
sp3
sp2
Intensity (a.u.)
16000
12000
8000
4000
0
290
288
286
284
282
280
Binding Energy (eV)

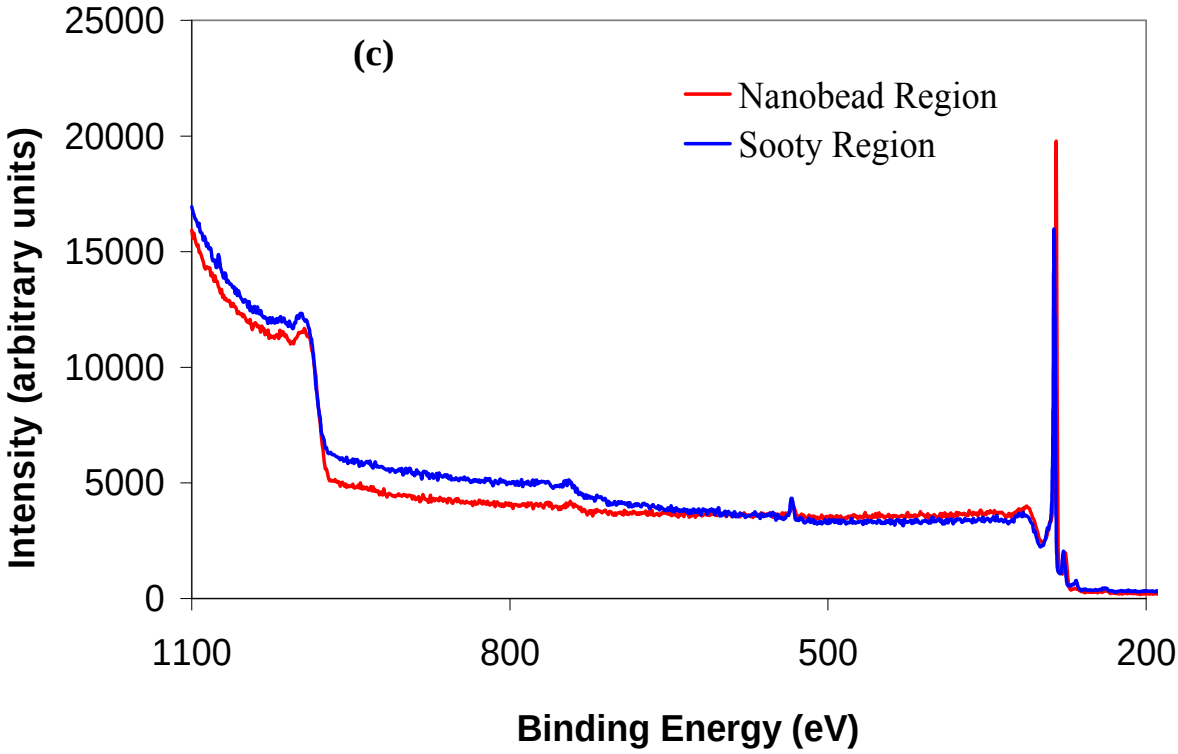

Figure 3.2.12 C1s spectra of (a) hydrophobic region and (b) sooty (hydrophilic) region of the disc and (c) complete XPS spectra of carbon deposited on the disc

3.2.3 Interaction of flame deposited carbon nanostructures with biofilms

Efforts are underway to harness energy from wastewater by developing microbial fuel cells (MiFCs) that generate electricity [64].A significant challenge in their development is the transfer of electrons from the microbes (bacteria) to the anode. Nanostructure-enhanced anodes have the potential to facilitate more efficient electron transfer since some forms present outstanding conducting properties and the nanostructures also increase the available surface area for cellular attachment.

Due to the affinity of some bacteria towards iron as well as hydrophobic surfaces, we exposed stainless steel (SS) substrates and to the ethylene flame described in Section 3.1. This resulted in the synthesis of carbon nanofiber/nanotube forests on the SS surface. These were then tested for biofilm formation using both – pure (e.g. *E. Coli*) as well as mixed (sludge water) cultures. Images were obtained using an environmental SEM (E-SEM) in low-vacuum mode without sputter-coating them with gold or any other surface treatment so as to prevent biofilm destruction. Figure 3.2.13(a) shows *Escherichia coli* K12 cells attaching on to a carbon fiber from a carbon cloth. Figure 3.2.13(b) shows the same cells in a biofilm formation on CNS coated SS substrate. The extracellular polymer substances (EPS) appears as the sludgy substance around the cells, which indicates that the cells are interacting amongst each other and have the potential for producing electrons and driving the MiFC. Figure 3.2.13(c) shows peapod-like cells forming a microbial colony on a similarly prepared SS substrate, but using a mixed non-nitrifying culture (sludge water).

We conjecture that the increase in surface area as well as the nature of the nanoscale asperities on the SS substrate induced by deposition of CNS in the flame

reactor promotes this attachment [65].It has been reported that such attachment is also promoted by the existence of hydrophobic surfaces (note that we have already reported the superhydrophobic characteristics of flame-deposited carbon films on surfaces in Section 3.2.2.). A combination of such effects could contribute to the affinity of such microbial colonies towards the CNS-enhanced substrates. This is an ongoing research area in our group with interesting future possibilities.

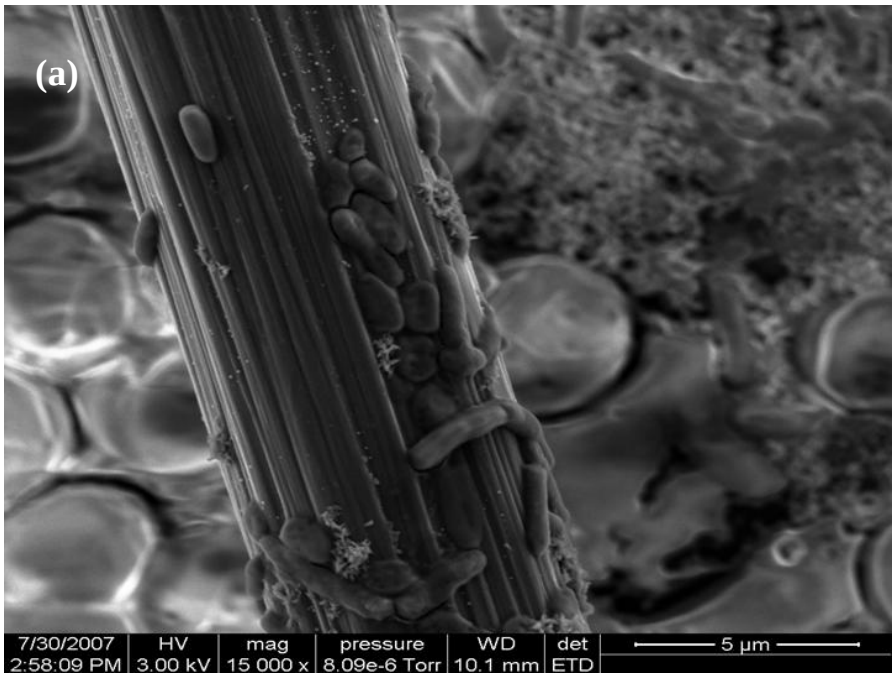

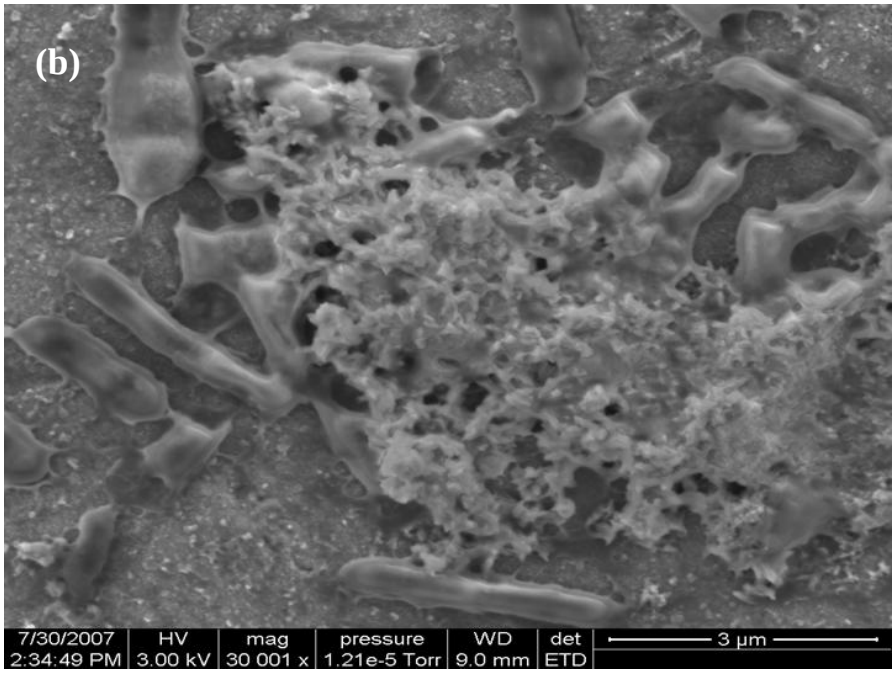

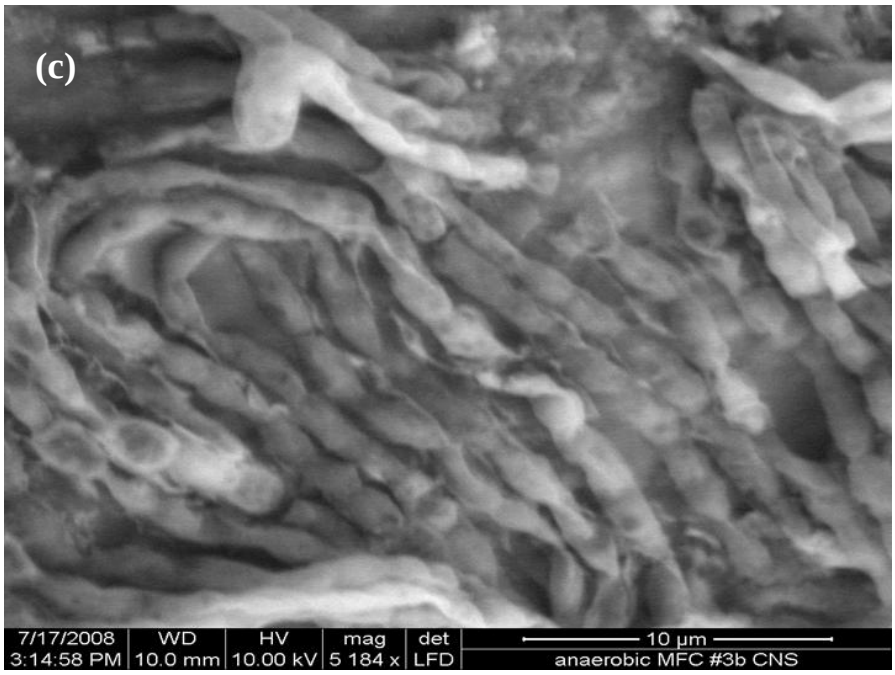

Figure 3.2.13 Microbial colonies formed on (a) carbon cloth fiber and (b) & (c) CNS-enhanced stainless steel (SS) anodes

3.3 Conclusions

In summary, a rapid on-demand process is presented for the synthesis of superhydrophobic surfaces on silicon. These coatings are durable and exhibit superhydrophobic behavior over long periods. FE-SEM, TEM and XPS analyses show the surface structure to be composed mainly of amorphous carbon nanobeads which, being closely packed, produce nanoscale roughness inducing superhydrophobicity. Our group is involved in a multidisciplinary project whereby microbial fuel cells (MiFCs) are used for wastewater treatment and simultaneous production of electricity. The key to success in such an endeavor is the attachment of microbial colonies to the anodes, whereby electrons are given out by the bacteria cells to complete the circuit. The superhydrophobic nature of the flame deposited carbon nanostructures, the increase in surface area resulting from their deposition and the ability to deposit these on SS substrates (iron being a key catalyst for CNS growth) enhance such attachment and hence result in better and more efficient wastewater treatment as well as electricity production.

CHAPTER 4

CNT GROWTH MODEL

4.1 Previous model

This model developed by us has also been reported in Ref. 66. Figure 4.1.1(a) schematically describes the carbon nanotube formation process. When the metal catalyst (e.g. wire) is inserted into a flame, it produces metal (or oxide) nanoparticles. Carbon is deposited on the metal surface by catalytic action of which (1) a portion is oxidized, and (2) another part forms an encapsulating layer on the catalyst particle surface due to carbon polymerization, eventually resulting in catalyst deactivation. In our model the particle is approximated as shown in Figure 4.1.1(b) and assumed to have a characteristic dimension 2/3 d_p (where d_p denotes the average diameter of a catalyst particle and is based on the expression of the average diffusion length [21,22]). The interface between the gaseous carbon-containing components and the catalyst nanoparticle (the top surface of Figure 4.1.1(b)) is referred to as the *leading face* while the other interface between the nanoparticle and the supporting substrate is called the *tailing face*.

The boundary condition at the interface between the gaseous combustion products and the catalyst particle is

$$(dn_C / dt)\big|_{x=0} = (r_{dep} - r_{ox}) - r_{diff} - r_{encap}, \tag{4.1.1}$$

where r_{dep} denotes the deposition rate derived from catalysis reactions, r_{ox} the oxidation rate of the carbon layer, r_{diff} the bulk diffusion rate through the metal, and r_{encap} the carbon encapsulation rate. The boundary condition at the interface between the catalyst nanoparticle and the supporting metal substrate is

$$(dn_C/dt)\big|_{x=2/3dp} = r_{diff}' - r_{nucl} - r_{growth}, \tag{4.1.2}$$

where r_{diff}' denotes the carbon diffusion rate across that interface, r_{nucl} the carbon nucleation rate there, and r_{growt} the nanofibrous carbon growth rate at the same interface. Using these boundary conditions, the unsteady state carbon diffusion through the metal catalyst particle is given by

$$(\partial n_C/\partial t) = D_S(\partial^2 n_C/\partial x^2), \tag{4.1.3}$$

where D_S denotes the carbon diffusivity through the metal catalyst. The required initial condition is $n_C\big|_{x=2/3dp} = 0$ at t = 0 for all x. The rate of carbon deposition r_{dep} depends on the gaseous combustion products in contact with the catalyst surface.

The term (r_{dep}-r_{ox}) in Equation (4.1.1) represents the carbon added to the catalyst surface from the ambient and equals the difference between the rate of impingement of single carbon atoms and the single atom desorption rate (67,68). The rate of impingement $R_i = NP/(2\pi MRT_g)^{0.5}$, where N denotes the Avogadro Number, P the partial pressure of the gas-phase specie that contributes carbon atoms to the surface, M the molecular weight of that gas phase species, R the gas constant, and T_g the ambient gas temperature. The desorption rate is n_s/τ, where n_s denotes the surface density of single carbon atoms at the leading face of the catalyst nanoparticle while $\tau = \nu^{-1}\, exp(E_a/kT)$ is the mean characteristic residence time (where ν is a constant characteristic of the surface and the nature of single atoms being deposited, carbon in this case, E_a the adsorption energy of carbon on the catalyst surface, and k is the Boltzmann constant). Therefore, Equation (4.1.1) assumes the form

$$(dn_C/dt)\big|_{x=0} = dn_s/dt = (R_i - n_s/\tau) - r_{diff} - r_{encap}. \quad (4.1.4)$$

The number of carbon atoms remaining on the surface, which leads to catalyst poisoning through the formation of an encapsulating layer, is provided by the rate of carbon encapsulation per unit area $r_{encap} = k_{encap} n_s^n$, [21,69] where k_{encap} represents the rate constant for carbon encapsulation, and n_s the surface density (units: length^{-2}) of carbon atoms at the leading face. The activity data of Chen *et al.* [69] have shown that the best fit for n provides a value of 6 for Ni. Zhang and Smith [21] also compared their activity data with curves obtained using n = 3 and n = 6 and observed a much better fit for the latter value (particularly for Co), which we have adopted.

Concluding about the model, it is observed that it unifies the submodels for: (a) Detailed combustion chemistry using the UNICORN code that accounts for thermal radiation. We have previously experimentally validated the simulated temperatures [2]. The chemistry included PAH species; soot was not modeled, since there is negligible soot formation. (b) Solid carbon deposition from combustion gases on to catalyst particles and catalyst chemistry. (c) Fickian diffusion of carbon through a metal nanoparticle and formation of an encapsulating layer that leads to catalyst poisoning or deactivation. We assume only unidirectional CNT growth. For either tip or base type growth, carbon diffusion through the particle is assumed to occur in only a single direction along the favorable concentration gradient. (d) Nucleation and growth of carbon nanostructures. The most important parameters influencing these submodels are the carbon surface diffusivity (for encapsulation), catalysis reaction constants, bulk carbon diffusivity through the catalyst nanoparticle, surface diffusivity for cluster formation at the tailing face, and stable cluster size (which is still not fundamentally well understood). Carbon is

deposited from surrounding gases for which we use a rate model that accounts for single carbon atom impingement on a catalyst surface and its subsequent desorption [Refs. 67, 68]. This approach handles the uncertainty about catalysis reaction rates and a combination of gaseous species (as in a combustion environment), by making use of their partial pressures and mole fractions in the neighborhood of the catalyst. Salient parameter values of this model are provided in Table 4.3.1.

A schematic showing the inter-connected steps involved in the modeling process is shown in Figure 4.1.2 below for further clarity. The schematic shows various interconnected processes that lead to catalytic synthesis of CNTs.

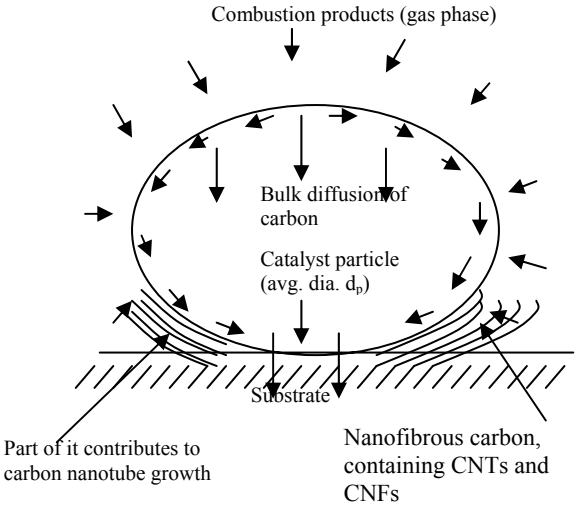

(a)

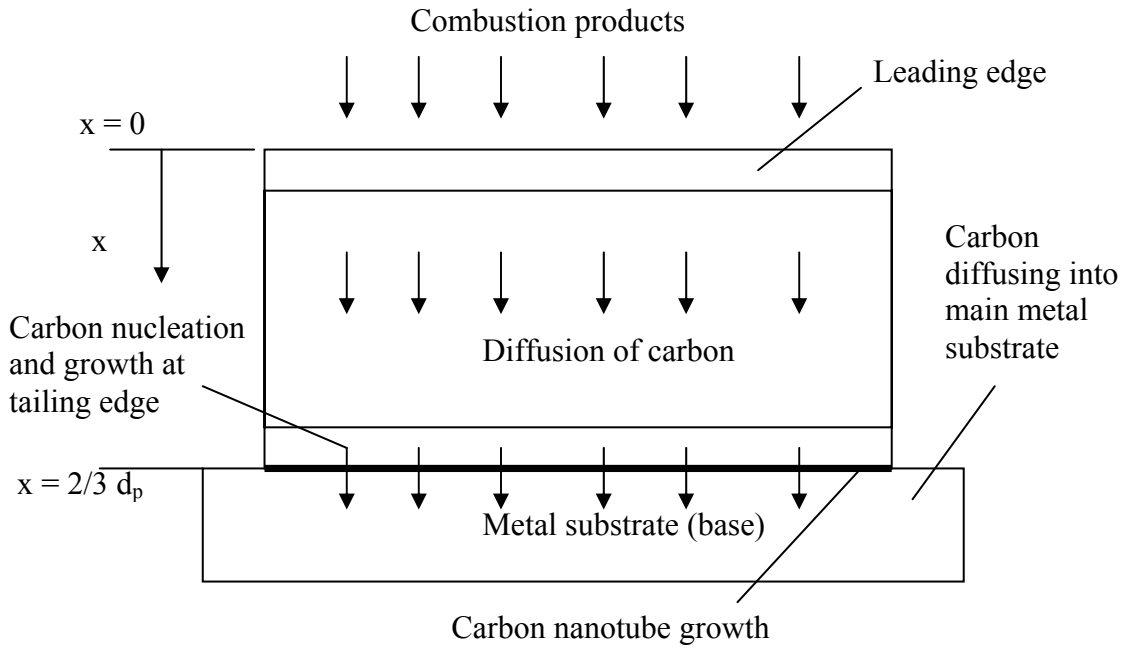

(b)

Figure 4.1.1 Schematic diagrams for (a) CNT growth process, (b) previous model for CNT growth

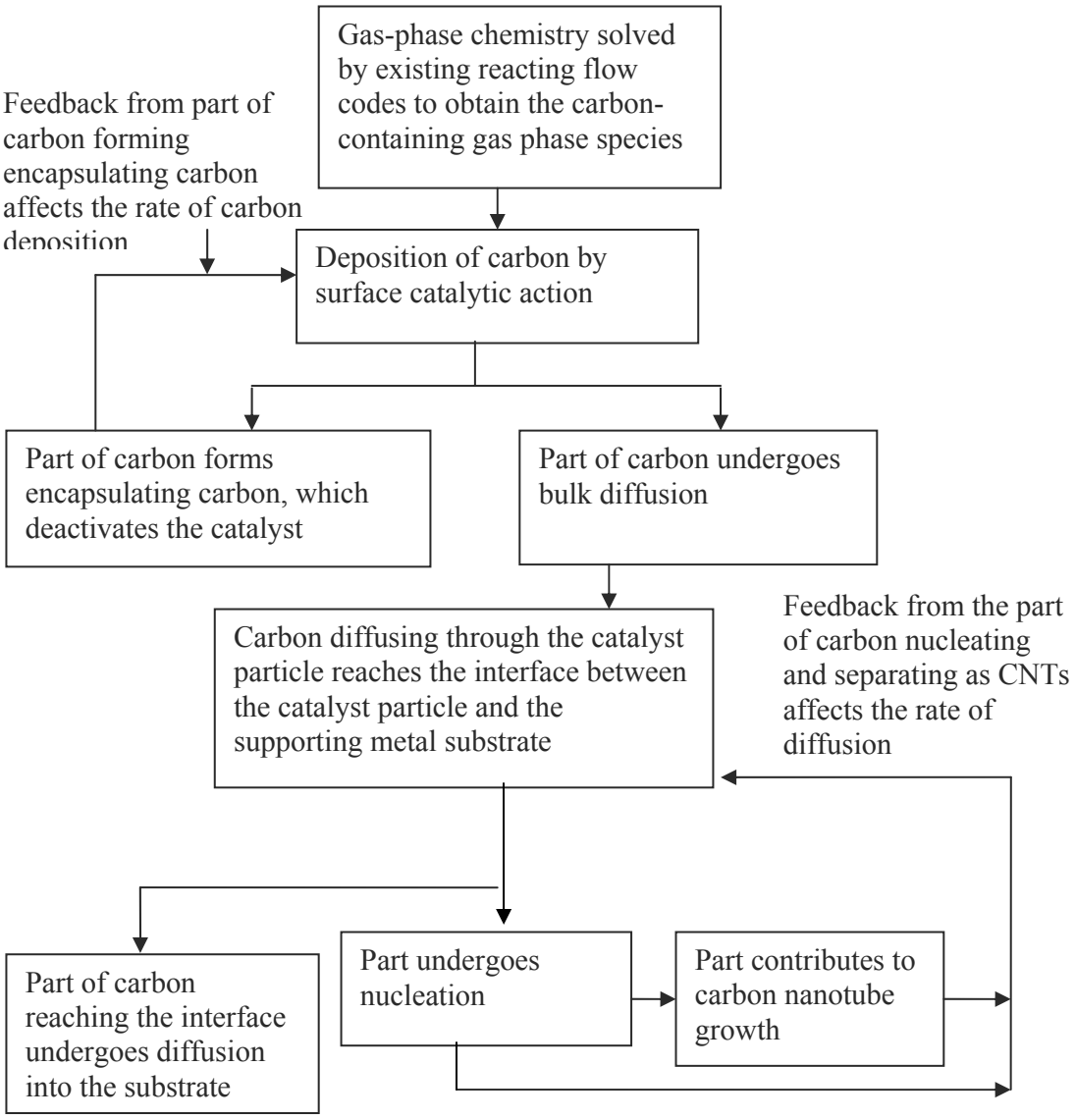

Figure 4.1.2 Schematic of the carbon nanotube growth modeling process

4.2 Modified model

The abovementioned model was modified by us, by considering catalyst surface poisoning in more detail and predicting carbon nanotube growth in terms of rate of increase of length, which is a more readily measurable quantity in experiments. This was recently accepted for publication [70]. The model includes a mechanism for CNT production based on a previous diamond nucleation model [67] that now also contains additional details about the adsorption energies, bulk diffusion energies and sticking coefficients. Figure 4.2.1 shows a schematic depicting the proposed mechanism of carbon nanostructure growth, as already mentioned above. The overall mechanism considers (a) the impingement of carbon atoms from the predominant carbon-containing species in the ambient, (b) their adsorption and desorption at the catalyst-gaseous hydrocarbon interface, (c) surface and bulk diffusions, (d) nucleation, and (e) separation of solid undissolved carbon in nanostructured form. The schematic of Figure 4.2.1 illustrates the modeled processes that lead to the catalyzed formation of CNTs. Salient features of the model are described below.

The overall time evolution of the surface concentration of single C atoms can be expressed as:

$$\frac{dn_1(t)}{dt} = N_{c,ads} - \frac{n_1(t)}{\tau_{res}} - \sigma_x D_s n_1(t) n_x(t) - (i+1)\sigma_i D_s n_1(t) n_i(t) - \Phi_{c1}\left(\frac{n_{p1}+n_{p2}}{\alpha_m n_m A_{np}}\right) - R_{d,out}, \quad (4.2.1)$$

where n_1 denotes the surface density of adsorbed carbon atoms, $N_{c,ads}$ their overall adsorption rate from gaseous hydrocarbons in the CNT synthesis environment, τ_{res} the residence time of the adsorbed hydrocarbons, D_s the surface diffusion coefficient of the adsorbed carbon atoms, $R_{d,out}$ the bulk diffusion rate of carbon atoms out of the catalyst

nanoparticle that contributes to the growth of a single CNT wall layer (here, single refers to the fact that if we consider multiwalled CNTs, this $R_{d,out}$ term will have to be divided by the number of walls to give us the length – so Equation 4.2.15 discussed later has to be divided by the number of CNT walls), α_m and n_m the numbers of carbon monolayers and their surface densities, respectively, and A_{np} the surface area of a catalyst nanoparticle. Φ_{c1} denotes the flux of the carbon-containing gaseous molecules to the surface of the catalyst nanoparticle. It is different from the additional carbon flux Φc, which is explained below.

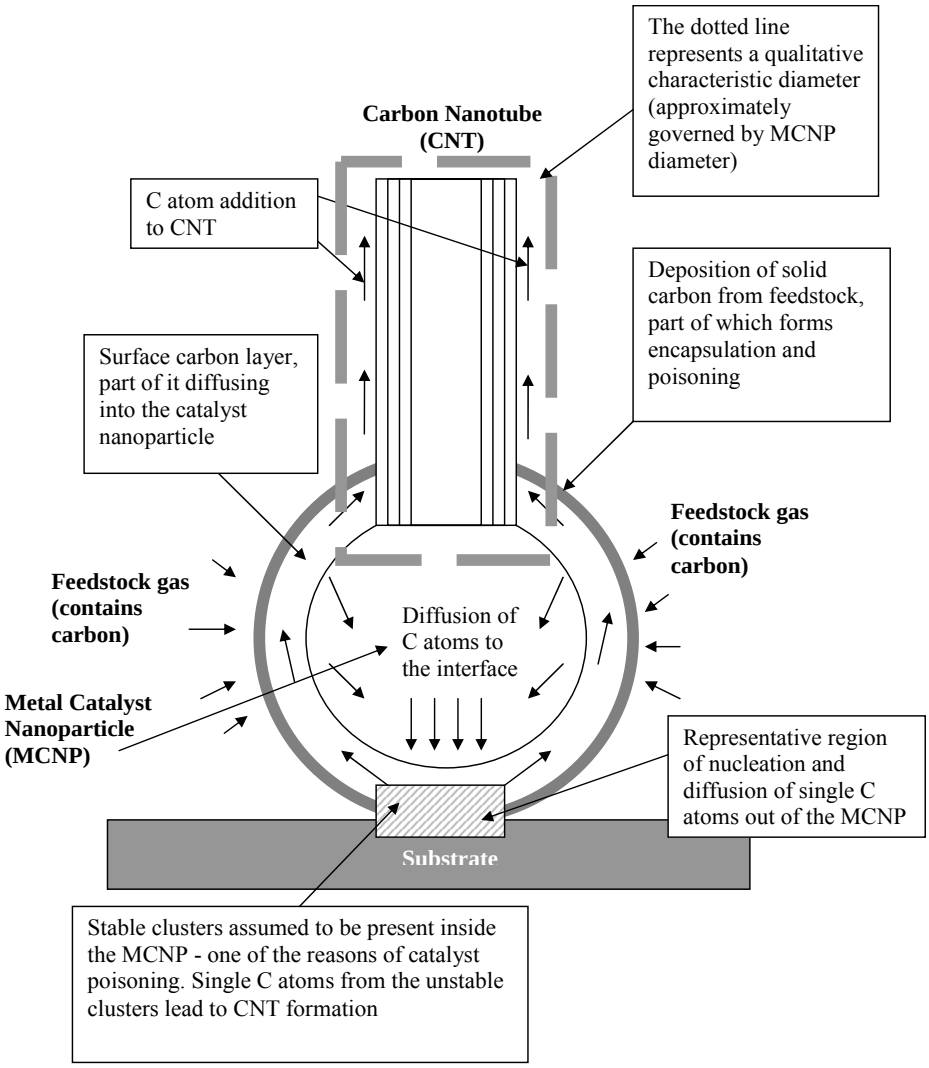

Figure 4.2.1 The various processes contributing to the catalyzed growth of a CNT from a metal catalyst nanoparticle (MCNP) described the modified model

The other symbols in Equation (4.2.1) are also explained in the following discussion.

1. The adsorption rate of the deposited carbon is determined from the impingement rates of the surrounding hydrocarbon species on the deposition surface and their sticking

coefficients. The desorption rate of the impinging C atoms is characterized through a representative mean residence time.

The overall adsorption rate is given by [67]

$$N_{c,ads} = N_{c,i}\nu, \tag{4.2.2}$$

where $N_{c,i}$ represents the impingement rate and ν the sticking coefficient of a particular hydrocarbon species. The sticking coefficient ν is defined as the probability of occurrence of a particular reaction process when a favorable collision occurs [67].

The impingement rate is

$$N_{c,i} = j\frac{N_{Av}P}{\sqrt{2\pi MRT}} = 3.513j\frac{P}{\sqrt{MT}}\times 10^{22}, \tag{4.2.3}$$

where j denotes the number of carbon atoms contained in each molecule of the predominant hydrocarbon species (e.g., j = 2 for C_2H_2), N_{Av} the Avogadro number, P the near-surface partial pressures of hydrocarbon species, M the molecular weight of the hydrocarbon species, R the universal gas constant and T the gas temperature at the surface (assumed herein to be the same as that of the substrate).

The mean residence time is

$$\tau_{res} = \frac{1}{\nu_{vib}}\exp\left(\frac{E_a}{k_B T}\right), \tag{4.2.4}$$

where ν_{vib} denotes the surface vibrational frequency of the adsorbed species, E_a the adsorption energy, k_B Boltzmann's constant and T the substrate temperature. The

combined term on the RHS of Equation (4.2.1) $\left[N_{c,ads} - \frac{n_1(t)}{\tau_{res}} \right]$ represents the net deposition of carbon atoms and includes the contribution from gaseous hydrocarbons and loss due to desorption and oxidation.

2. The surface concentration of C atoms at any instant is $n_1(t)$. These atoms diffuse into and over the substrate with diffusivities D_s and D, respectively. Diffusion into the substrate depletes the surface atoms and results in the formation of a solid solution or a carbide. The surface diffusion leads to the formation and growth of clusters containing j carbon atoms that have a surface density n_j. These clusters are more likely to undergo growth than decay when the cluster size exceeds a critical number i. Growing clusters are termed stable and ones that decay are unstable. In this context, n_i denotes the critical cluster size density at the tailing face, and n_x the stable cluster site density. The catalyst substrate contains N_0 sites that have equal adsorption energies E_a. These two parameters are used to compute the surface diffusivity D_s at different temperatures. For sake of simplicity, we assume that the rates of nucleation and growth are dominated by single C atom addition processes. This implies that the nucleation rate depends upon the addition of these atoms to clusters containing i atoms. The capture numbers σ_i and σ_x describe diffusion fluxes of single C atoms into stable and critical sized nuclei, as discussed by Venables *et al*. [71]. These capture numbers are generally assumed to be slowly varying quantities with σ_i varying from 2 to 4 and σ_x from 5 to 10. Herein, their values are taken as 4 and 5, respectively.

The time evolution of the surface density of stable nuclei is expressed as

$$\frac{dn_x}{dt} = \sigma_i D_s n_1(t) n_i(t), \tag{4.2.5}$$

where Zinsmeister's relation [67] provides the concentration of critical clusters, i.e.,

$$n_i(t) = \begin{cases} \frac{1}{2} n_1(t)(x(t) - i), & x > i \\ n_i = 0, & 1 < x \le i \end{cases}, \text{ where } x = \sigma_i D_s \int_0^t n_1(t) dt. \tag{4.2.6}$$

3. An additional carbon flux Φc produces a poisoning carbonaceous layer n_{p1} due to the deposition of pyrolysis products that are also derived from the adjacent gaseous hydrocarbon species. This flux does not contribute to CNT formation. The poisoning layer can become partially dissolved within the catalyst nanoparticle through a process that is described through the dissolution rate constant k_{dis}. Another inactive catalyst layer n_{p2} is also formed due to metal carbide formation and changes in the catalyst oxidation state by either direct oxygen desorption or indirect hydrogen reduction. It is possible to reactivate the 'poisoned' or deactivated catalyst layer by introducing catalyst reactivation gases, a process that is modeled through the activation rate constant k_{ac} [33].

The rates are given by

$$\frac{dn_{p1}}{dt} = \Phi_c \left(1 - \frac{n_{p1}(t) + n_{p2}(t)}{\alpha_m n_m A_{np}} \right) + k_{cl} n_1(t) - k_{dis} n_{p1}(t), \text{ and} \tag{4.2.7}$$

$$\frac{dn_{p2}}{dt} = R_c \left(1 - \frac{n_{p1}(t) + n_{p2}(t)}{\alpha_m n_m A_{np}} \right) - k_{ac} n_{p2}(t). \tag{4.2.8}$$

where k_{cl} denotes the rate constant describing the formation of a carbonaceous layer, and the rate constant R_c can be differently interpreted depending upon the predominant catalyst deactivation method related to the specific growth conditions.

The additional carbon flux is given by

$$\Phi_c = \Phi_b p_b \exp\left(-\frac{E_{ab}}{k_B T}\right), \tag{4.2.9}$$

where Φ_b denotes the flux of the main pyrolysis product on the surface of a catalyst nanoparticle, and p_b a frequency factor and E_{ab} a corresponding energy barrier. The rate constant is given by

$$k_{cl} = A \exp\left(-\frac{E_{cl}}{k_B T}\right). \tag{4.2.10}$$

where A represents another frequency factor and E_{cl} the activation barrier for the formation of a carbonaceous layer. In the case of direct oxygen desorption from the surface of the catalyst nanoparticle, the rate constant is expressed as

$$R_c = C_1 \exp\left(-\frac{E_R}{k_B T}\right), \tag{4.2.11}$$

where again C_1 denotes a frequency factor and E_R the corresponding activation energy barrier. However, if the deactivation occurs due to reduction by hydrogen present in the gaseous ambient, then this rate assumes the form is

$$R_c = \tilde{\Phi}_{H2} n_{H2} R_{H2}, \tag{4.2.12}$$

where $\tilde{\Phi}_{H2}\, n_{H2}$ represents the hydrogen flux onto the surface of the catalyst nanoparticle and R_{H2} the corresponding rate constant for the sticking and dissociation of H_2 on the surface of the catalyst nanoparticle [33]. The temperature dependent variable is $R_{H2} = C_2 \exp\left(-\frac{E_{RH}}{k_B T}\right)$ where C_2, and E_{RH} again denote the corresponding frequency factor and activation energy.

The last term on the RHS of Equation (4.2.1) is

$$R_{d,out} = C_0 \sqrt{\frac{D_b}{\pi t}}\,, \tag{4.2.13}$$

where $C_0 \approx n_1(t)/a_c$ denotes the volume concentration of the C atoms at the substrate surface, a_c = 1.54 Å is the diameter of a C atom and D_b represents the carbon bulk diffusivity derived from Fick's first law of diffusion. The total number of C atoms, diffusing into the CNT layers is expressed as

$$N_{tot} = \int_0^t R^*_{d,out}\, dt\,, \tag{4.2.14}$$

where $R^*_{d,out} = R_{d,out}(t = t_s)$. The thickness of the CNT layer is given by

$$L(t) = \frac{N_{tot}}{C^*} = \left[\frac{1}{a_c C^*}\sqrt{\frac{D_b}{\pi}}\right] \times \int_0^t \frac{n_1(t)}{\sqrt{t}} dt\,, \tag{4.2.15}$$

where C^* denotes the volume of C atoms necessary to form a carbon monolayer and $n_{1,s}$ the surface density of adsorbed carbon atoms chosen at the saturation value of the surface density of stable nuclei, i.e., $n_1(t) = n_{1,s}$ at $t = t_s$. The surface density of a carbon atom monolayer n_m is O(10^{15} atoms/cm^2). At first, single carbon atoms accumulate on the

surface so that their surface density increases until the inception of clusters. After cluster formation is initiated, this surface density, which has reached a maximum, decreases monotonically. The time at which this maximum occurs is the saturation time t_s which is a characteristic both of the catalyst and the conditions, such as temperature and hydrocarbon partial pressure. The values for the model parameters are listed in Table 4.3.2. A variety of gases (e.g., CO, C_2H_4, C_2H_2) are used during the CVD synthesis of CNTs. For sake of simplicity we have compared our model with experimental results obtained using C_2H_2 as the feedstock gas.

4.3 Choice of model parameters

Table 4.3.1 Parameter values for previous model

Parameters	Values
d_p	20 nm
D_s	13.6 x 10^{-14} cm^2s^{-1} (CVD) 3.66 x 10^{-6} cm^2s^{-1} (Flame Synthesis)
ν	7.214 x 10^{10} s^{-1}
E_a	2.78 x 10^{-19} J/atom
k_{encap}	1.13 x 10^{-79} $cm^{10}s^{-1}$
σ_x	5
σ_i	4
D_1	1 x 10^{-20} cm^2s^{-1}

Table 4.3.2 Parameter values used in the modified model (Cobalt catalyst).

Parameter	Value	Comments and Reference
Φ_{c1}	3×10^{5} atoms/s	33
Φ_{c}	3×10^{-1} atoms/s	33
R_c	6.54×10^{-7} s^{-1}	33
k_{cl}	3.0×10^{-3} s^{-1}	33
N_0	2.6×10^{14} cm^{-2}	Calculated from 67,77
C^*	2.011×10^{22}	77
ν_a	1.0×10^{13} s^{-1}	77
D_b	13.6×10^{-14} cm^2s^{-1}	21
ν	0.2	67
E_a	6.228 eV/atom	21
α_m	1.0	33
n_m	1.0×10^{15} atoms/cm^2	33
σ_x	5	21,77
σ_i	4	21,77
D_s	0.52×10^{-16} cm^2s^{-1}	21

4.4 Results

4.4.1 Model validation

There is no accurate experimental growth rate data for CNT/CNF flame synthesis. Therefore, for model validation, the corresponding measured data for methane-CVD synthesis was chosen. Thereafter, CNT/CNF growth rates for ethylene/air nonpremixed flames have been considered. The validation for our previous model is conducted for methane decomposition in a 23% CH_4/12% H_2/65% Ar mixture at 773 K (total gas flow of 185 mL (STP) min^{-1}at 101 kPa) on a 30 wt% Co/SiO_2 catalyst.

The simulation domain involving the catalyst nanoparticle $\approx 10^{-9}$ m. The bulk diffusivity of carbon in Fe, $D_S \approx 10^{-10}$ m^2/s. Since we use an explicit scheme to solve the transient diffusion equation, the characteristic length scale $\Delta x \sim 10^{-10}$ m for ten spatial points in a nanoparticle. An order of magnitude analysis shows that a minimum time step is given by $\Delta t < (\Delta x)^2/D_s$, (or $< 10^{-10}$ s). When compared with the global process time, this small time step makes the calculations computationally intensive, since at least $\approx 10^{12}$-10^{13} steps are now required to run the simulation for a few minutes. The problem is compounded, since in order to produce accurate solutions, a much lower time step size $\approx 10^{-12}$ s has been chosen.

The values of the parameters in the simulations are as follows. These are summarized in Table 4.3.1 above, as already mentioned. The characteristic nanoparticle size d_p is taken as 20 nm. For the validation study involving CVD deposition of CNTs the value of D_s is assumed to be 13.6×10^{-14} cm^2 s^{-1} [21] whereas for flame synthesis it is taken as 3.66×10^{-6} cm^2 s^{-1} [72]. The ν value is assumed to be 7.214×10^{10} s^{-1} [21,67], that

of E_a as 2.78×10^{-19} J/atom [21], and of k_{encap} to be 1.13×10^{-79} cm^{10} s^{-1} [21,69]. (The value of k_{encap} is usually very small, but the contribution made by the term $k_{encap}n_S^6$, which is the expression for the number of carbon atoms in the encapsulating layer, is significant because n_s is of $O(10^{17}\text{-}10^{21})$ in our calculations.). The filamentous growth rate is compared against the measured data of Ref. 21 in Figure 4.4.1(a). (Here, this rate is represented by $\sigma_x D_1 n_1 n_x$, where σ_x is a capture number, that typically has a value of 5, and is used to describe the diffusion of single atoms into a stable carbon atom cluster formed by nucleation [71].) D_1 denotes the diffusivity with which single carbon atoms diffuse over the cluster formed at the tailing face. For Fe, its typical value is of $O(10^{-20})$ cm^2 s^{-1} [21,67,68]. For steady filament growth, the rate eventually assumes a constant value ≈0.6 mmol/min/g of catalyst. There is very good agreement between the measured data and our simulations.

Our simulations show that steady carbon deposition and filament growth occurs once there is a stable carbon cluster size due to nucleation. A small cluster is formed when carbon atoms collect and become attached, which then grows in size. The model incorporates a critical cluster size formation model that was used originally for diamond nuclei formation [67]. Some clusters decay, and only those that reach a critical cluster size contribute to CNT/CNF growth in the form of nanofibrous carbon. The concentration of critical clusters, n_i is given by $n_i = 0.5n_1(x\text{-}i)$ for $x>i$ and is 0 for $x<0$. Here, x is given by $x = \sigma_i D_1 \int_0^t n_1 dt$ and i is the critical cluster size, its value being taken as 10 [21,67]. σ_i is another capture number, having a value 4 [67,71]. The rate of nucleation is given by $r_{nucl} = (i+1)N_r$, where $N_r = \sigma_i D_1 n_1 n_i$. The growth rate predicted here is the filamentous carbon growth rate and it includes all forms of carbon in the nanofibrous form, including

nodules, nanoparticles, CNTs, CNFs and all sorts of nanostructures. So, strictly speaking, CNTs constitute only part of what is predicted, and presently it is impossible to predict actually what part forms into just tubes or wires.

Validation of the modified model is carried out against experimental data reporting carbon nanotube growth in terms of length, which is a more readily measurable quantity. The literature reports experimental growth rates for CNTs in terms of their change in length for various chemical vapor deposition (CVD) conditions and several catalysts. Sharma *et al*. [73] described the effect of varying temperature (in the range 723-873K) and pressure (from 0.8-20 mTorr) on the CVD growth of multiwalled carbon nanotubes (MWCNTs) with an acetylene flow over a Ni catalyst. Experimental results for Fe catalyzed CNT growth rate have also been reported by several other groups, e.g., Jönsson *et al*. [74], Liu *et al*. [75], and Yu *et al*. [29]. Puretzky *et al*. [33] obtained *in situ* measurements and modeled CNT growth during CVD synthesis using Al/Fe/Mo multilayered catalysts with C_2H_2 feedstock at various partial pressures.

Experimental results reported by Bower *et al*. [76] for cobalt (Co)-catalyzed microwave plasma CVD synthesis of CNTs is used for model validation. This is done, since the model parameter values are most dependable for Co [76] as catalyst and acetylene [77] as feedstock. A parametric study of CNT growth is also conducted for various conditions. The Co catalyst employed in the experiments [76] was supported on a SiO_2 substrate that was surrounded by a gas phase at a temperature and pressure of 1098 K and 20 Torr. The acetylene partial pressure was 5 Torr. The measured outer diameters of the MWCNTs thus formed were predominantly distributed around 30 nm. TEM

micrographs of the CNTs grown in that study typically showed outer diameters of around 10 nm.

A simple relation for the estimation of the number of CNT walls is

$$\frac{d_o - d_i}{2} = n \times t + (n-1) \times d' \qquad (4.1.1),$$

where d_o denotes the outer diameter of the CNT, d_i its inner diameter, n the number of walls, t the thickness of a grapheme sheet forming a concentric tube (roughly equal to the diameter of a C atom), and d' the distance between two graphene sheets. The atomic diameter for carbon is 0.14 nm and the distance between two concentric grapheme sheets is 0.343 nm. Assuming multiwalled CNTs to be composed of perfectly concentric tubes formed by rolling the graphene sheets, the number of walls for a 30 nm OD and 10 nm ID CNT is ≈20.

Figure 4.4.1(b) compares the measurements over their entire duration (1800s) with the model predictions (for the modified model). While the number of walls in the synthesized MWCNTs was not experimentally determined [76], there is excellent agreement between both datasets if each MWCNT is assumed to consist of 20 graphene walls, which is a realistic number of walls based on the above discussion. The inset in the figure presents predictions for MWCNTs containing 5, 10, 20, 30 and 35 walls over an initial duration of 700 s. While there are differences, in general, the growth length for the cases involving 10-35 walls is of the same order of magnitude.

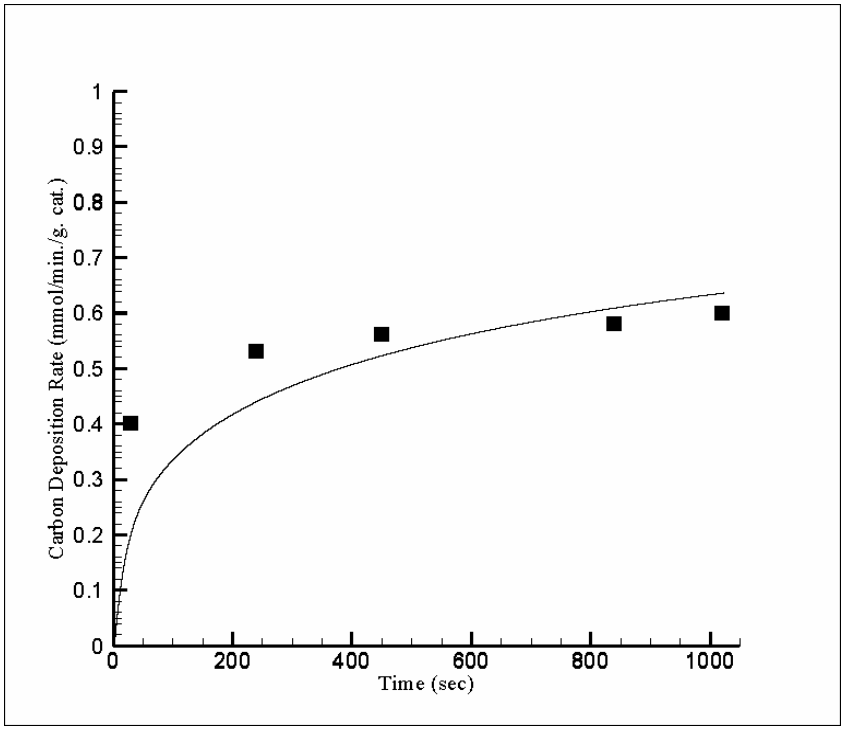
Carbon Deposition Rate (mmol/min./g. cat.)
Time (sec)
0
0.1
0.2
0.3
0.4
0.5
0.6
0.7
0.8
0.9
1
0
200
400
600
800
1000

(a)

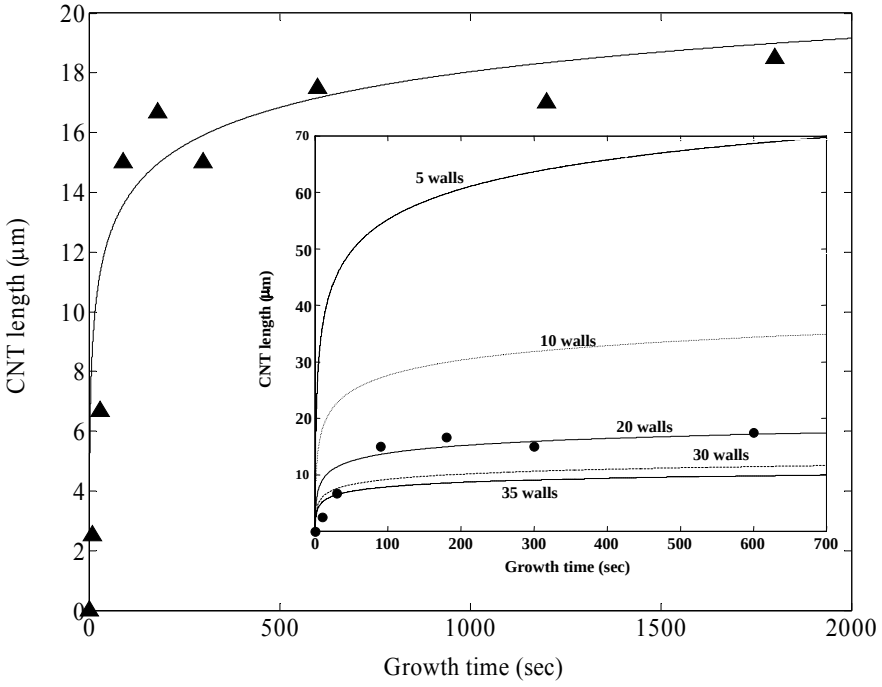
CNT length (μm)
Growth time (sec)
0
2
4
6
8
10
12
14
16
18
20
0
500
1000
1500
2000
5 walls
10 walls
20 walls
30 walls
35 walls
CNT length (μm)
Growth time (sec)
10
20
30
40
50
60
70
0
100
200
300
400
500
600
700

(b)

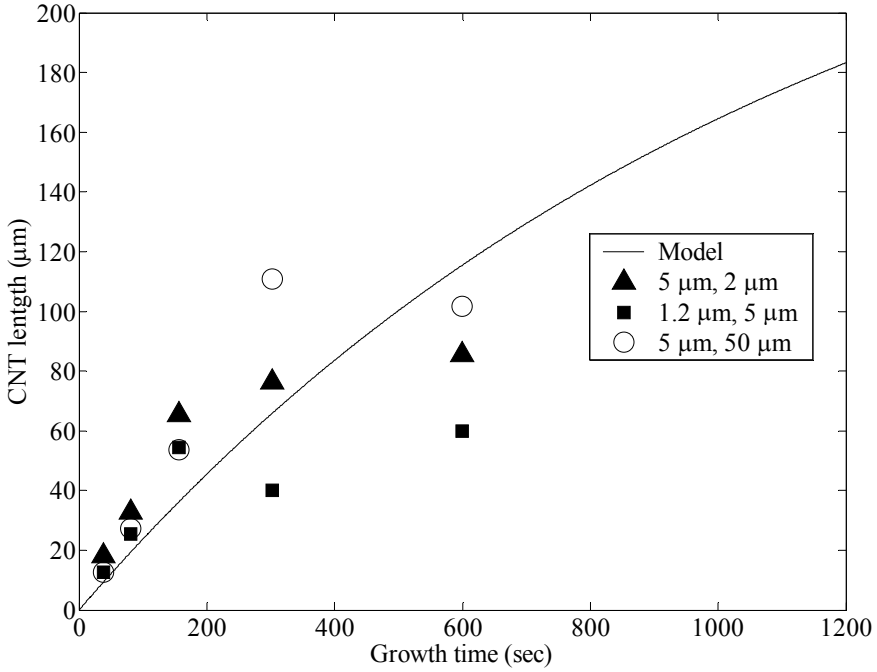

(c)

Figure 4.4.1 (a) Comparison of the growth rate (in mmol/min/g catalyst) of carbon nanostructures (CNTs and CNFs) predicted by the previous model against experimental results obtained by Zhang and Smith [21]; (b) Validation of the model against the experimental results obtained from Bower *et al*. [76]; (c) Validation of the model against experimental results from Bronikowski [78]. The triangles represent experimental growth rate for CNTs deposited on Fe catalyst in patterns of circular dots that have a 5 μm diameter and edge-to-edge dot separations of 2 μm; the small squares represent 1.2 μm particle diameters and 5 μm separations; the circles represent 5 μm particle diameters and 50 μm separations.

The parameter values used for Co catalysis of CNTs correspond unambiguously to experimentally observed growth rate data [76]. For completeness, the model predictions are also compared with similar measurements made by flowing C_2H_4 over silica-supported Fe catalyst beds at 725ºC and 200 Torr pressure [78]. However, dependable model parameter values are unavailable for these conditions, requiring their extrapolation from other conditions. In this case, the agreement between predictions and

measurements is not as good as for cobalt, although the trends and orders of magnitude are similar. We attribute the differences to the uncertainties in measurements as noted through the data scatter and also to the extrapolated parameter values. Moreover, the number of experimentally observed CNT walls varied between 5 and 10 whereas the predictions uniformly assume 10 walls. Figure 4.4.1(c) shows the comparison of the growth rate predicted by the model against the experimental results presented in ref. 78.

4.4.2 Parametric study

The CNT growth rate and terminal length have both been shown to increase with increasing temperature [33,75]. This behavior is reproduced by our model, as shown in Figure 4.4.2(a), between 900 and 1100 K, which is a temperature range typically associated with CVD synthesis. It is observed that the terminal length is very temperature sensitive, which is in accord with the results of Puretzky *et al*. [33]. Our predictions for these lengths at 900, 1000, and 1100 K are approximately 0.16, 2.94, and 19.5 μm respectively. At higher temperatures, several catalyst poisoning mechanisms occur, mainly due to the presence of gas-phase pyrolysis products and the reduction of the catalyst active state [33], which are outside the scope of the model and this investigation.

Figure 4.4.2(b) presents the predicted dependence of the growth rate of length for C_2H_2 partial pressures in the range 50 mTorr to 5 Torr at 1100 K. These results also show that the growth rate and terminal length increase with increasing partial pressure at a constant temperature. Similar experimental results have been reported by Liu *et al*. [75] who used acetylene and silica-supported Fe catalyst. The terminal lengths for 0.05, 2.5 and 5.0 Torr pressures are approximately 0.75, 11.5 and 19.5 μm, respectively.

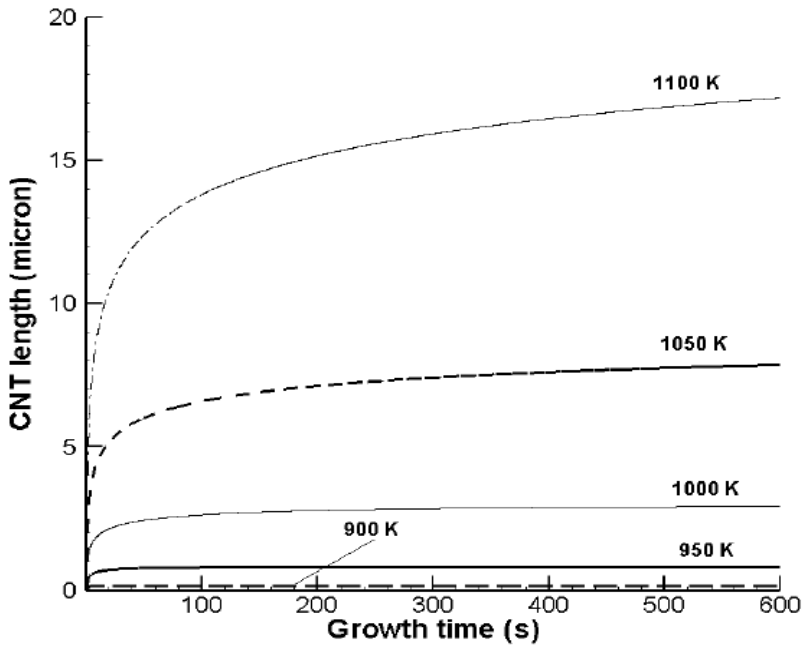

(a)

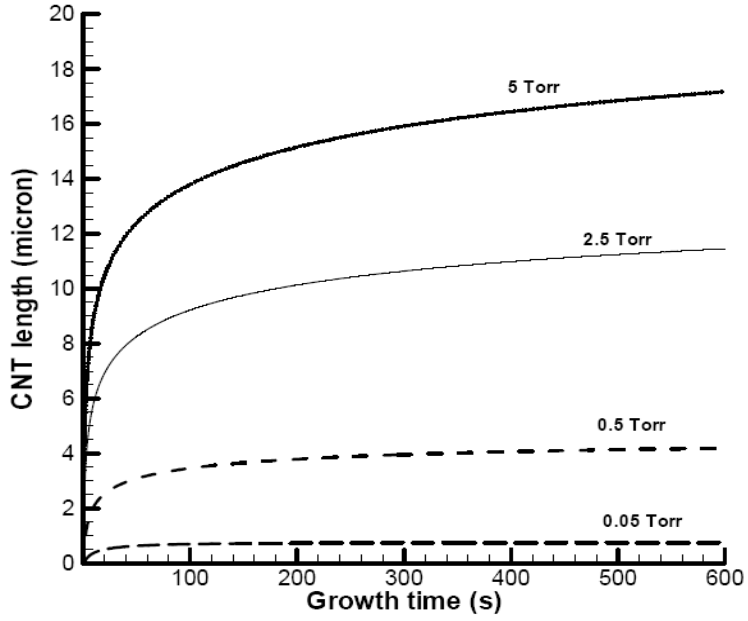

(b)

Figure 4.4.2 (a) CNT length versus time for CVD synthesis at different temperatures using Co as catalyst and 5 Torr. C_2H_2 partial pressure and (b) for CVD synthesis at different C_2H_2 partial pressures using Co as the catalyst at 1100 K.

The growth rate during the CVD synthesis of CNTs increases with an increase in the size of the catalyst particle until it reaches a critical value for which the growth rate is maximum. For example, in case of silica-supported Fe catalyst beds, CNT growth from CO disproportionation reaches a maximum for catalyst particle sizes in the vicinity of 15 nm at temperatures of around 600 °C [29]. Molecular dynamics simulations have shown that large catalyst particles, which contain at least 20 iron atoms, nucleate SWNTs that have a far better tubular structure than SWNTs nucleated from smaller clusters [79]. Here, SWNTs that grew from the larger clusters were found to have diameters similar to the cluster diameter, whereas smaller clusters with diameters smaller than 0.5 nm nucleated nanotubes that were ≈0.6–0.7 nm in diameter. A smaller catalyst particle size leads to a shorter diffusion length and a larger net exposed surface area in relation to its volume, which helps to increase the growth rate of carbon nanostructures. However, the saturation concentration of deposited carbon leading to CNT formation also increases at smaller particle volumes, leading to a lower driving force for carbon diffusion, which tends to negate the first two effects. Therefore, there is a competition between the factors leading to the formation of CNTs. This implies the existence of an optimum particle size at which the growth rate becomes maximum.

Discussion on growth mode

It is imperative to understand the mode of growth and the conditions that determine the same in any discussion about the modeling of carbon nanotube synthesis. The two dominant growth modes that can be observed in catalytic CNT synthesis are base growth and tip growth. These are illustrated in Figure 4.4.3 below.

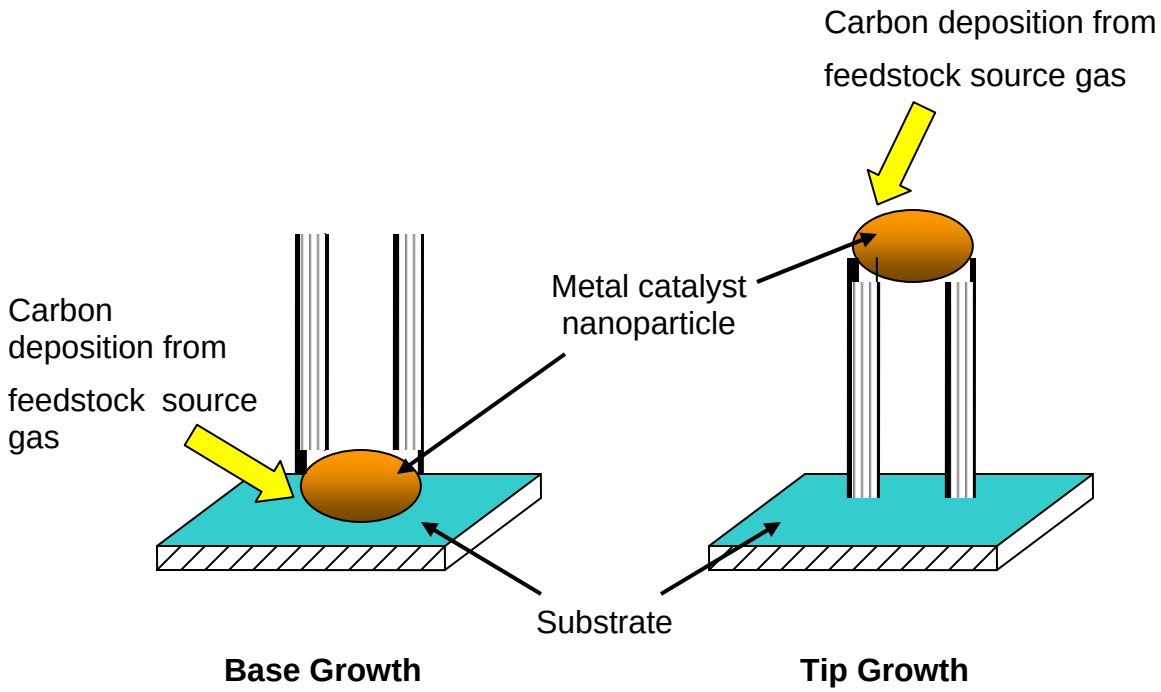

Figure 4.4.3 Carbon nanotube growth mode

Base growth mode arises when the metal nanoparticle catalyzing the growing carbon nanostructure remains at the bottom of the nanotube. For this type of growth the adhesive forces between the substrate and the catalyst nanoparticle are typically too large for the particle to be lifted as the CNT/CNF grows. Alternately, the catalyst nanoparticle is lifted by the growing carbon nanostructure during tip growth, and remains at the tip of the CNT/CNF after its growth ceases. The likely growth (tip or base) mode depends on the energy gain $\Delta E_{np \to CNT}$ due to the addition of C-atoms from the carbon-metal catalyst solution to the graphene sheets forming the CNTs and CNFs. For tip growth to occur, the catalyst particle is lifted from a substrate only if the energy gain is sufficient to overcome the surface binding or interface energy between the nanoparticle and the substrate, i.e.,

$\Delta E_{np\to CNT} \geq \gamma R_p^2$, where γ and R_p respectively denote the surface energy per unit area and the diameter of the metal catalyst particle. Smaller energy gains lead to base growth.

The nature of the growth mode, whether tip or base, is important for various applications. For instance, the nucleation of metal particles on the end caps of CNTs can assist in the alignment of these nanostructures in the presence of external electric or magnetic fields, thus imparting directional properties to materials in which these are embedded [80, 81]. Such functionalized tips can also be used to attract other molecules for various applications, e.g., for functionalization with protonated amines ($-NH_3^+Cl^-$) that add positive charges to CNTs, which allows binding to negatively charged RNA molecules [82]. Continuum scale CNT growth models that typically assume a certain growth mode [21] can also benefit from these predictions. It has further been suggested that the growth mode depends upon two characteristic times, respectively, the diffusion and surface saturation times $\tau_d \approx R_p^2 / D_b$ and $\tau_s \approx C^*_{Sat}{}^2 D_b / Q^2$ [83]. Here, D_b represents carbon bulk diffusivity in the metal catalyst, C^*_{Sat} the carbon saturation concentration in the metal catalyst particle (in terms of number of particles per unit volume), $Q = P_c / (2\pi m k_B T)^{1/2}$ the carbon flux, P_c, T and m the partial pressure, temperature and molecular mass of the carbon-containing gas, respectively, and k_B the Boltzmann constant.

4.4.3 Extension of model to flame synthesis

An axisymmetric combustion code UNICORN [84] is used to solve for the gas-phase species concentrations at the various heights, which are then used as inputs into the CNT/CNF growth model. We used Ni and Fe wire substrates of 0.1-0.25 mm diameter to

grow these carbon nanostructures. Our simulations showed that these small diameter wires produced no appreciable flow disturbances or temperature gradients across the substrate.

Figure 4.4.4(a) shows the variation of the site density of single carbon atoms n_1 over time for the CVD synthesis of CNTs [21]. The result is in excellent agreement with Ref. 21 regarding the magnitude of n_1 and its time history. Like theirs, the peak value of $n_1 \approx 8\times10^{14}$ cm^{-2} occurs at $\approx$ 7 s which thereafter declines to $\approx1.8\times10^{14}$ cm^{-2}. Before carbon nucleation is initiated, the surface density of single carbon atoms increases as they are added through diffusion from the leading face. Later, the diffusion potential (proportional to the difference in the numbers of single carbon atoms at the leading and tailing faces) decreases, since carbon atom accumulation near the tailing face through which CNT/CNF growth occurs reduces its concentration gradient. However, with the onset of nucleation and growth, n_1 decreases at the tailing face, increasing the concentration gradient and reinstating diffusion as the major driving potential for carbon atom transport through the particle. The n_1 value finally stabilizes due to stable filament growth at the tailing face.

Figure 4.4.4(b) presents the surface density of single carbon atoms due to flame synthesis at various heights in the flame. The inset contains profiles at the three heights over ≈0.15 s, but due to the overall similarity of the curves only the plot for the 4 mm height is shown for a longer duration. Previous flame synthesis studies of CNT/CNF growth by our group [1,2] found that the largest yield occurred at this height. For these cases, the nucleation stages (around 0.03 s as compared with 7 s for CVD) and the eventual near-constant stages are reached much earlier than for the CVD process. In

contrast with the CVD example, for which the process time ≈1000s, for flame synthesis it is ≈100s, i.e., and order of magnitude faster. As for CVD, the peak n_1 value occurs very early on. While CVD processes take hours to produce CNTs/CNFs, both our model and previous experimental observations by our group [1,2] confirm a corresponding formation time of the order minutes for flame synthesis. However, the carbon density is two orders of magnitude larger ($\approx 10^{17}$ as compared to $\approx 10^{15}$ cm^{-2} for CVD). The results support our hypothesis that flame synthesis can be a much faster and higher throughput process than CVD. The peak values of n_1 decrease with increasing height above the flame and occur later, which is consistent with our experimental observations.

The growth rates for the three heights are presented in Figure 4.4.5. The CNT/CNF growth rate decreases with increasing height above the burner. The reason for this variation is not just the decreasing temperature with increase in height. Although the flamefront temperature is a factor, the CO concentration, which is the major contributor to carbon deposition, also decreases with increasing height above the burner. Our results show that the contribution to carbon deposition by CO and CO_2 is dominant during CNT/CNF flame synthesis in nonpremixed flames. Not only are saturated and unsaturated hydrocarbon concentrations generally very small at flamefront locations, but the Fe catalyst is also preferentially more reactive there toward CO. Vander Wal [12] studied the preferential reactivity of Fe toward some gaseous carbon-containing species during flame synthesis. It was observed that Fe nanocatalyst particles have a preference toward CO over unsaturated hydrocarbons such as C_2H_2. CO is known to create a more reactive catalyst surface by restructuring bulk single crystal Fe [85,86]. The melting points of selected nanoscale materials have been measured or calculated to be lower than

their bulk counterparts by as much as 50% [12,87]. By competing for active sites (on the near-molten catalyst nanoparticles) CO acts to prevent the catalyst surface from being coated by carbon by limiting the adsorption rates of C_2H_2, C_2H_4 and other unsaturated hydrocarbons. This combined with the thermal restructuring of the nanoparticle makes CO a more desirable source of carbon than gaseous hydrocarbons when they are both present in the combustion products. Hence larger CNT yield is observed closer to the burner.

The model is capable of parametrically investigating the combined effect of several carbon-contributing species in a flame. While these species were introduced into the model, it was observed that their effects were negligible due to their exceedingly small concentrations.

Figure 4.4.5 shows that the filamentous carbon growth rate is approximately an order of magnitude larger from flame synthesis than for CVD (Figure 4.4.1(a)), again confirming our hypothesis that flame synthesis is a higher throughput process. The growth rate decreases with increasing height in the flame and its plot flattens over time so that after a sufficiently long duration, like during CVD, the synthesis rate of CNTs/CNFs also achieves a steady value. In that regard the plots in Figure 4.4.1(a) and Figure 4.4.5 are similar, but the flame synthesis growth rates are about an order of magnitude larger. However, it has been experimentally observed during this study that control over the flame synthesized CNT/CNF growth rate and structures is difficult and, therefore, our predictions may help define future directions in this regard.

In a recent investigation, Yu *et al.* [88] discussed the influence of hydrogen and temperature on CNT production from CO over a Ni-Fe catalyst through a

disproportionation reaction in the temperature range 450-600 °C. They found that at lower temperatures, the initial reaction rate of CO with the Ni-Fe catalyst is much faster. However, a faster initial reaction rate led to earlier catalyst deactivation so that eventually there was a much larger CNT yield at higher temperatures. Catalyst activity was preserved for almost twice as long for the highest temperature as compared to the lowest one. The deactivation time and typical run times for a typical CVD process of the order of hours. Although flame synthesis is much faster and catalyst deactivation should occur earlier, it is still prohibitively expensive to computationally model the process explicitly. In the flame synthesis cases that we have considered, the CO concentration, which is the major contributor to carbon deposition, decreases with increasing height above the burner although the local temperatures decrease (which should induce later catalyst deactivation). The net result is a larger CNT/CNF yield close to the burner.

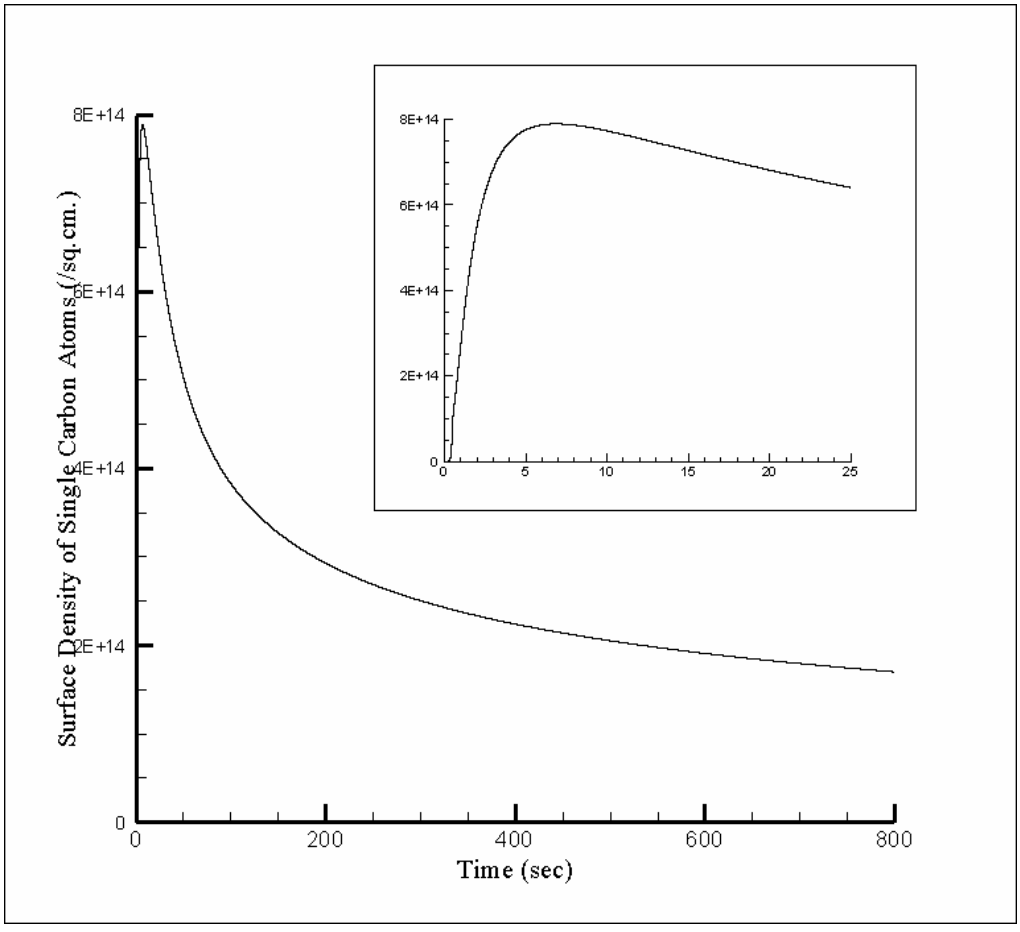
8E+14
6E+14
4E+14
2E+14
0
Surface Density of Single Carbon Atoms (/sq.cm.)
0
200
400
600
800
Time (sec)
8E+14
6E+14
4E+14
2E+14
0
0
5
10
15
20
25

(a)

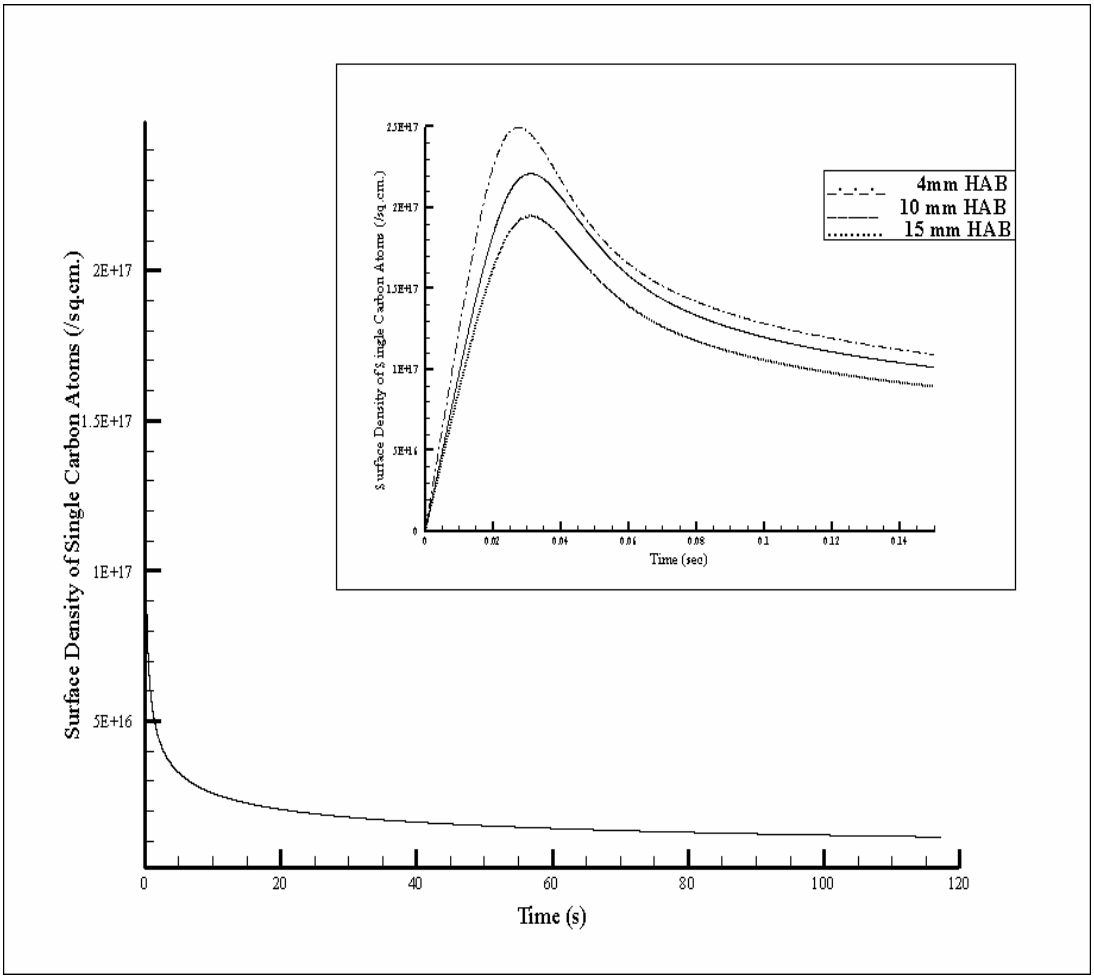

(b)

Figure 4.4.4 (a) Variation of surface densities of single carbon atoms (cm^{-2}) over time (s) for CVD process described in ref 21 and (b) for various heights above the burner during flame synthesis described in refs. 1, 2 and 66

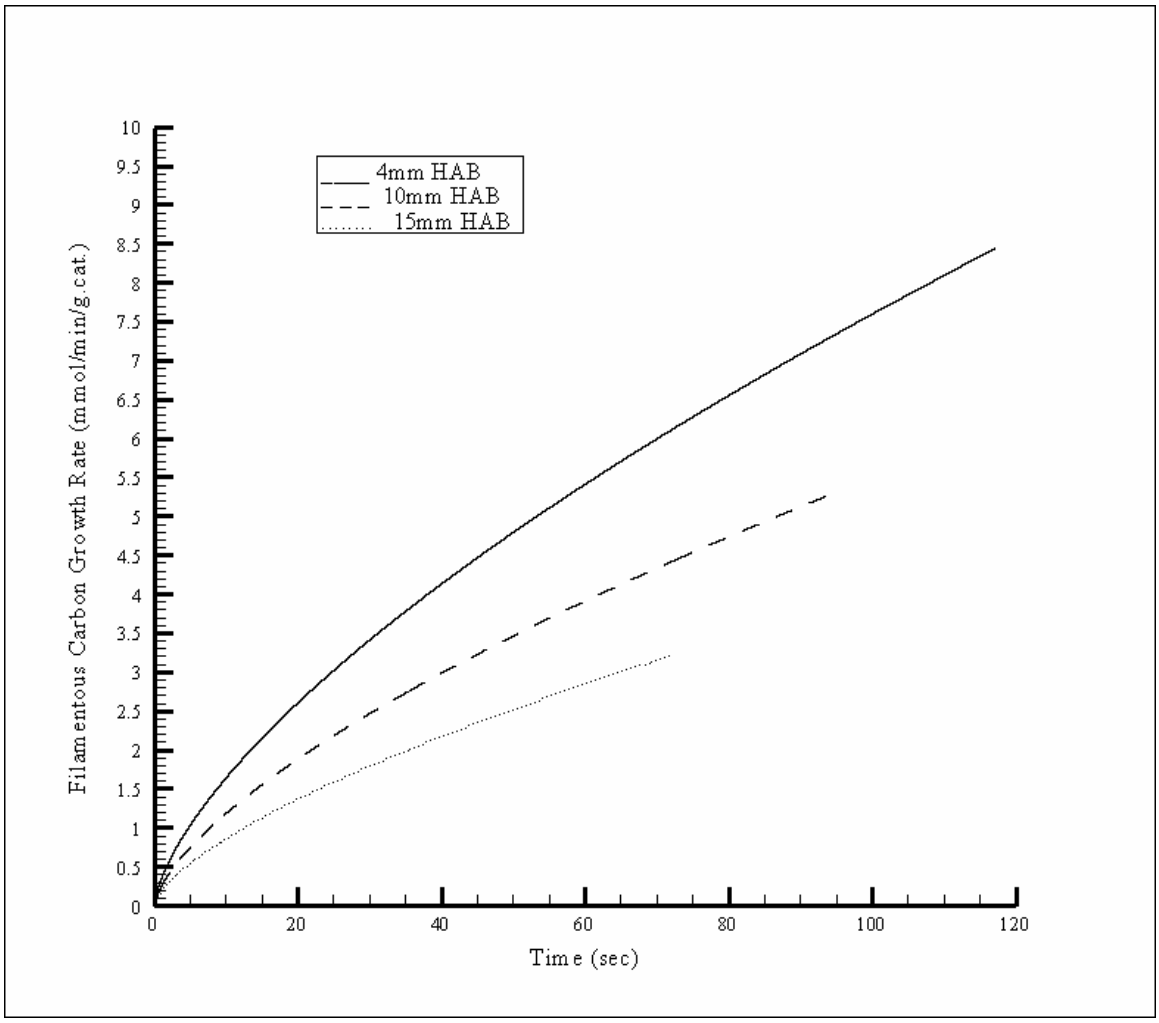

Figure 4.4.5 Carbon deposition rates (mmol/min/g catalyst) corresponding to Figure 4.4.4(b)

4.5 Conclusions

This section of the dissertation proposes a generic model to predict the growth rate of CNTs/CNFs that is also applicable to flame synthesis. The research makes two major contributions. First, it develops a submodel for carbon deposition from a mixture of carbon-containing gases. Existing models address only specific sets of conditions. Therefore, our modification has a significant impact on the results. Second, it integrates a variety of other submodels to develop a comprehensive approach for modeling CNT/CNF synthesis under flame conditions. The model is validated against CVD data due to the dearth of similar data for flame synthesis. The CNT/CNF growth rate is found to decrease with ascending flame height. This variation can be attributed to a coupled effect that arises due to decreasing temperature (which suppresses catalyst deactivation) and decreasing CO concentration (since CO is the major contributor towards carbon deposition). These combined effects explain a higher CNT/CNF yield closer the burner.

The modified model predicts CNT growth rate in terms of length, which is a convenient measurement, since similar measurements in terms of CNT weight are prone to significant errors. The model is validated and can thus be used to identify those CVD conditions that optimize CNT production. A parametric study shows that an increase in either the temperature or feedstock partial pressure leads to increasing CNT growth rate and terminal length, results that are consistent with previous experimental measurements.

CHAPTER 5

CATALYTIC SILICON NANOWIRE GROWTH MODEL

5.1 Summary of previous SiNW growth models

Silicon plays a key role in the microelectronics industry. Nanostructured silicon in the form of wires, ribbons, and tubes has novel electronic and optical properties that are suitable for applications in nanoelectronics and field-effect transistors. Silicon nanotubes and silicon nanowires (SiNTs/SiNWs) are grown using silane (SiH_4) as the silicon (Si) source and gold (Au) nanoparticles as catalyst [89]. Herein, we develop a model for the Au-catalyzed growth of SiNWs.

The vapor-liquid-solid (VLS) growth of SiNWs was first discussed by Wagner and Ellis [90]. They used Au particles as catalysts to grow crystalline semiconductor whiskers from vapor sources such as $SiCl_4$ or SiH_4. At a certain temperature, Au particles on the Si substrate first react with Si to form Au–Si alloy droplets. The melting point of these alloy droplets is lower than for either Si or Au. For example, the melting point of a 4:1 (Au:Si) solution is 363°C, while the corresponding values for bulk Au and bulk Si are 1064°C and 1420°C, respectively. These Au-Si alloy droplets act as catalysts for SiNW growth. The unidirectional growth of Si whiskers can be interpreted based on the difference between the sticking coefficients of the impinging vapor source atoms on the surfaces of the liquid catalytic droplet and the solid substrate. In principle, if the temperature is sufficiently high, an ideal liquid surface captures all impinging Si source atoms, while a solid Si surface rejects almost all these source atoms. This classical VLS mechanism is still considered applicable.

Wang *et al*. [91] discussed a growth model for SiNWs based on the surface tension and contact angle conditions of the catalyst droplet, and subsequent consideration of supersaturation and growth [92]. In some cases, nanowire growth is controlled by surface diffusion; in a diffusion-induced VLS model [93], molecules in the vapor phase are considered to first fall on the liquid surface, then diffuse along it to the liquid-solid (LS) interface, and finally incorporate themselves into the solid wire (see Fig. 13(b)). Thus, the nanowire growth rate depends mainly on the surface concentration gradient and the surface diffusion coefficient of the Si atoms in the catalyst.

All of these models treat surface tension, Gibbs free energy considerations and the contact angle between the metal catalyst droplet and the substrate. However, they do not integrate the molecular processes influencing SiNW growth, such as Si deposition from the ambient, its diffusion into the catalyst droplet, or the subsequent nucleation and growth of the nanowires once the nuclei reach a critical size. The model presented herein is more comprehensive in that it considers these interrelated processes. It does not, however, incorporate the surface contact conditions between the metal catalyst droplet, the substrate and the growing SiNWs.

There is experimental evidence that the diameters of SiNWs are almost identical to those of the Au nanoparticles used to catalyze their growth. The deposition of Si on an Au catalyst particle is modeled using the approach described in *Section 5.1*. We assume that the diffusion of Si atoms deposited on an Au nanoparticle is similar manner to the movement of C atoms through a corresponding catalyst nanoparticle. However, the nucleation of Si atoms in Au is fundamentally different from that of C atoms in an

analogous catalyst. We therefore develop a nucleation model from Si crystal growth theory.

The classical theory of crystal growth [94] assumes a mononuclear (MN) mechanism, i.e., each nucleus formed on the crystal face gives rise to a monatomic layer. The theory thus predicts a growth rate that is proportional to the nucleation rate and the interface area. In reality, other nuclei may form adjacent to the spreading nucleus before the monolayer is completely formed, leading to polynuclear (PN) growth. The PN mechanism occurs during either instantaneous nucleation or progressive nucleation. During instantaneous nucleation, all crystallites in the system nucleate instantaneously at time $t = 0$ after which they grow irreversibly until the phase transition is accomplished. However, crystallites are continuously nucleated during progressive nucleation so that the surface reliefs of crystal faces growing through the MN and PN mechanisms are different.

The simplest kind of growth occurs when nucleation is stationary for which a necessary condition is the time invariance of nucleation frequencies, i.e., the temperature and supersaturation state of the system remain constant. We assume that crystal growth occurs through the more general PN growth mechanism for which we develop a modified Kolmogorov-Johnson-Mehl-Avrami (KJMA) model [95] to describe the island nucleation that is assumed to occur in a layer-by-layer fashion. An island refers to a collection of molecules (either two- or three-dimensional depending on the model) which, after reaching a critical size and a free energy barrier that is associated with the nucleation process, spread outwards.

5.2 Proposed Model

Our predictions of SiNW production are based on an adsorption rate model [96] which contains details of adsorption energies, bulk diffusion energies and sticking coefficients. The overall mechanism considers (a) the impingement of Si atoms from the SiH_4 in the ambient, (b) their adsorption and desorption at the Au catalyst- SiH_4 interface, (c) surface and bulk diffusion, (d) nucleation, and (e) separation of solid undissolved Si into a nanostructured form. The salient features of the model are described below.

The overall time evolution of the surface concentration of single Si atoms is expressed as

$$dn_1(t)/dt = N_{Si,ads} - n_1(t)/\tau_{res} - dN_{nucl}/dt - R_{d,out}, \quad (5.2.1)$$

where n_1 denotes the surface density of adsorbed Si atoms, $N_{c,ads}$ their overall adsorption rate from silane in the SiNW synthesis environment, τ_{res} the residence time of the adsorbed Si in Au, D_s the surface diffusion coefficient of the adsorbed Si atoms, and $R_{d,out}$ the bulk diffusion rate of Si atoms out of the Au nanoparticle (that contributes to the growth of SiNWs). The other symbols in Equation (5.2.1) are explained below.

1. Adsorption Rate: The adsorption rate of the deposited Si is determined from the impingement rates of the surrounding SiH_4 molecules on the deposition surface and their sticking coefficients. The desorption rate of the impinging Si atoms is characterized by a mean residence time. The overall adsorption rate [97]

$$N_{Si,ads} = N_{Si,i} S_{Si}, \quad (5.2.2)$$

where $N_{Si,i}$ represents the impingement rate, and S_{Si} the sticking coefficient of SiH_4. The sticking coefficient is the probability of an Si atom sticking to the catalyst surface when a SiH_4 molecule collides with it. The coefficient has an exponential dependence on the ambient temperature. From SiH_4 thermal decomposition data [98],

$$S_{Si} = 10^{3.0\pm0.2} \exp(-148(kJ/mol)/(RT)) \times (0.1333224 \times P)^{-0.59}, \qquad (5.2.3)$$

where P denotes the near-surface partial pressure of SiH_4 in torr. This expression is valid for the heterogeneous decomposition of SiH_4 for $750 < T < 1000$ K and $1.5\times10^{-3} < P < 15$ torr. For all practical purposes, the VLS growth of SiNWs is carried out in these ranges of temperature and SiH_4 partial pressure. The impingement rate

$$N_{Si,i} = jN_{Av}P/\sqrt{2\pi MRT} = 3.513jP/\sqrt{MT}\times10^{22}, \qquad (5.2.4)$$

where j denotes the number of Si atoms contained in each molecule of SiH_4 (e.g., $j = 1$ in this case), N_{Av} Avogadro's number, M the molecular weight of SiH_4, R the universal gas constant, and T the gas temperature at the surface (assumed herein to be the same as that of the substrate). The mean residence time

$$\tau_{res} = 1/\nu_{vib} \exp(E_a / k_B T), \qquad (5.2.5)$$

where ν_{vib} denotes the surface vibrational frequency of the adsorbed species, E_a the adsorption energy, k_B Boltzmann's constant, and T the substrate temperature. The combined term on the RHS of Eq. (6.1) [$N_{Si,ads} - n_1(t)/\tau_{res}$] represents the net deposition of Si atoms. It includes the contribution from gaseous silane and loss due to desorption and oxidation.

2. Nucleation: Its rate is modeled on a nucleation law that includes an incubation time [99], i.e.,

$$dN_{nucl}/dt = N_0 Z\beta \exp(-\alpha \Delta G^*/(k_B T))\exp(-\tau/t), \quad (5.2.6)$$

where N_0 denotes the number of potential nucleation sites, Z the Zeldovich factor (taken here as 0.05 for Si precipitation under low degrees of supersaturation [99,100]), β^* the atomic impingement rate, G^* the activation barrier for nucleation, τ the incubation period, and ΔG^* the free energy of a precipitate of size r^* during purely homogeneous nucleation. However, perfectly homogeneous nucleation rarely occurs, since a homogeneous distribution of nanoprecipitates is generally formed even on defects like dislocation loops or vacancy/solute-rich clusters, which tends to reduce the activation barrier for nucleation. This is accounted for in the model by incorporating an effective activation barrier equal to $\alpha\Delta G^*$ in Eq. (5.2.6), where α is a constant in the range $0<\alpha<1$.

3. Diffusion and Growth: The last term on the RHS of Eq. (5.2.1)

$$R_{d,out} = C_0\sqrt{D_b/\pi t}\,, \quad (5.2.7)$$

where $C_0 \approx n_1(t)/a_{Si}$ denotes the volume concentration of the Si atoms on the substrate surface, a_{Si} = 1.54 Å the diameter of an Si atom, and D_b the Si bulk diffusivity derived from Fick's first law of diffusion. The total number of Si atoms diffusing into the SiNW layers

$$N_{tot} = \int_0^t R^*_{d,out}\,dt\,, \quad (5.2.8)$$

where $R^*_{d,out} = R_{d,out}(t = t_s)$. The thickness of the SiNW layer

$$L(t) = N_{tot} / C_S^* = (1/(a_{Si} C_S^*)\sqrt{D_b / \pi}) \times \int_0^t n_1(t) / \sqrt{t}\, dt\,, \qquad (5.2.9)$$

where C_S^* denotes the volume of Si atoms necessary to form a Si monolayer and $n_{1,s}$ the surface density of adsorbed Si atoms chosen at the saturation value of the surface density of stable nuclei, i.e., $n_1(t) = n_{1,s}$ at $t = t_s$. The surface density of a Si atom monolayer n_m is O(10^{15} atoms/cm^2).

At first, single Si atoms accumulate on the surface so that their surface density increases until the inception of clusters. Before cluster formation is initiated, this density increases as these atoms are added through diffusion. Later, the diffusion potential decreases, since Si atom accumulation near the catalyst-substrate interface through which SiNW growth occurs reduces the concentration gradient of the same. However, with the onset of nucleation and growth, n_1 decreases at the tailing face, increasing the concentration gradient of Si atoms and reinstating diffusion as the major driving potential for Si atom transport through the particle. The n_1 value finally stabilizes due to stable filament growth at the tailing face. The time at which this maximum occurs is the saturation time t_s, which is a characteristic of both the catalyst and the conditions, such as temperature and SiH_4 partial pressure.

5.3 Results and Discussion

Figure 5.3.1 compares predictions of SiNW growth (from the instant it is initiated) with CVD experimental data [101] for a SiH_4 partial pressure of 0.65 torr, and 400, 426, 451 and 500°C temperatures. Overall, the predicted SiNW growth trend is

similar to that for the measurements. The semi-log plot is presented keeping two things in mind: to clearly show the four temperature conditions in one plot (they are shown separately later on ordinary axes), and to stress on the order of magnitude agreement between the predicted results and reported data. For the 451 °C and 500 °C cases, the plots and the reported data are in very good agreement. However, the agreement deteriorates for the lower temperatures. Indeed, the agreement is better for the growth temperature of 400 °C than for 426 °C.

Figure 5.3.2 compares predictions of the growth rate with measurements for different SiH_4 partial pressures [101]. The model predicts an increase in the growth rate with increasing partial pressure, which is in qualitative agreement with the reported data. However, quantitative differences exist, which are attributed to the unavailability of exact parameter values for the nucleation model for the following reasons.

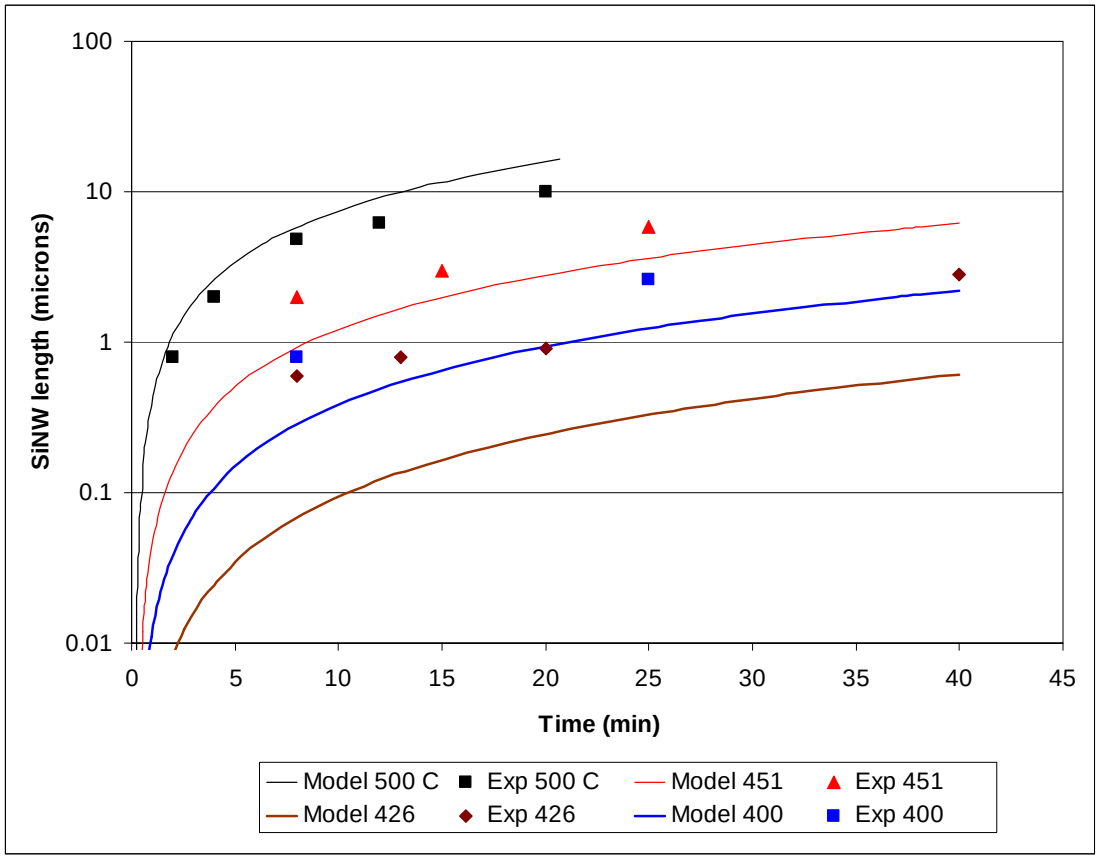

Figure 5.3.1 Semi-log plot showing the comparison between predicted growth (in μm) and experimental growth of SiNW vs. time reported by Lew *et al.* [101] for three different growth temperatures – 400°C, 426°C, 451°C and 500°C.

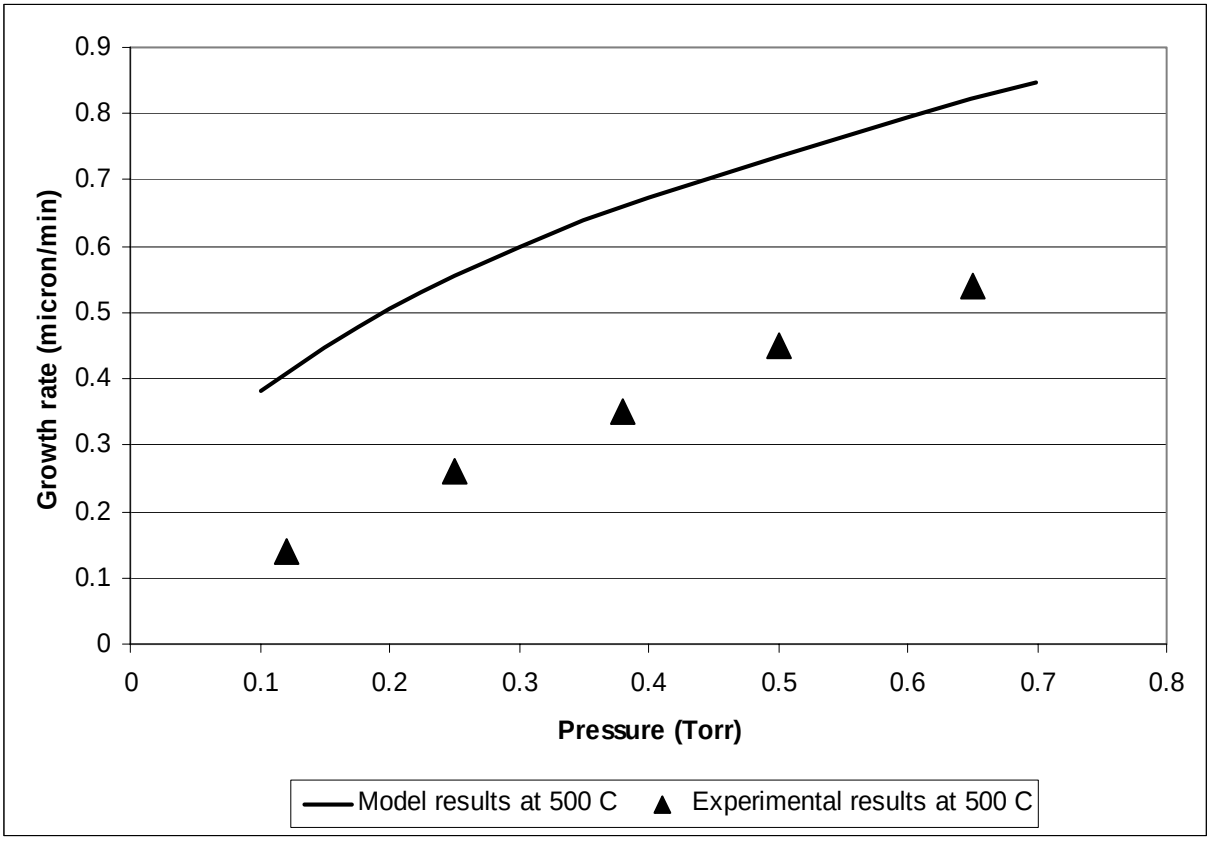

Figure 5.3.2 Growth rate (μm/min) versus partial pressure for SiNW synthesis at 500°C compared with date from Ref. 101.

First, the homogeneous nucleation approximation for the activation barrier ΔG^* is unrealistic, since the actual activation barrier is invariably smaller. The value of α, which accounts for the nonhomogeneity of the nucleation process, is adopted from a single source in the literature [98] that does not correspond to the SiNW growth conditions of Ref. 101. More realistic data are unavailable. Second, uncertainties in the bulk diffusion coefficient of Si in Au and the sticking coefficient of Si on the catalyst surface induce other temperature-sensitive errors in the application of the model.

A number of expressions exist for the temperature-dependence of the diffusion coefficient. Assuming that the diffusion coefficients and the concentrations of vacancies in interstitial gold and substitutional Au vary according to an Arrhenius law, a plot of log D_b vs. $1/T$ is a straight line. Here, D_b refers to the bulk diffusion coefficient of Si in Au. Wilcox and LaChapelle [102] proposed three different Arrhenius-type relations for Si-Au binary diffusion [102], i.e., $D_b = 2.75\times10^{-3}\ exp(-\ 47400/RT)$, $1.15\times10^{3}\ exp(-\ 71800/RT)$, or $1.78\times10^{-2}\ exp(-\ 26000/RT)$. The D_b vs. $1/T$ plots for these three diffusivities are contained in Appendix III. We have used the last of these three expressions in our model, since it is valid when there are more than 10^3 dislocations/cm^2 at the diffusing surface. While it is beyond the scope of this thesis to determine the number of dislocations that is characteristic of the Au catalyzed growth of SiNWs, we note that catalyst beds are prepared by the deposition of gold nanoparticles. This process most likely induces a large number of dislocations and improper surface conditions. The first two relations represent diffusion conditions at saturated and structurally homogeneous surface conditions, respectively. Since the synthesis process ceases upon reaching equilibrium, which corresponds to complete poisoning of the catalyst, these are most likely not for cases

pertinent to the catalyzed growth of SiNWs. The predicted growth rates using the first of the three D_b relations are two orders of magnitude smaller than the measurements. The second relation also underpredicts these growth rates.

5.4 Conclusions on SiNW growth model

In summary, we propose a model for the Au-catalyzed growth of SiNW using SiH_4 as the source gas. We assume a nucleation model and model the impingement of Si atoms from the ambient and their subsequent diffusion in a manner similar to that for carbon nanotube growth, as discussed in Chapter 3. However, critical parameter values are unavailable for conditions corresponding to experimental measurements. Thus, while our results agree qualitatively with reported experimental data (with similar orders of magnitude for the growth rate), the quantitative agreement varies. Nonetheless, the model is a useful stepping stone to understand catalytic SiNW growth, since most of the previous literature either contains only Si beam epitaxy models for nanowires or is empirical. Improvement of the model is part of ongoing research in our group.

CHAPTER 6

CONCLUSIONS AND FUTURE WORK

Conclusions

This thesis reports a comprehensive numerical/experimental study on the growth of carbon nanostructures. The experimental portion of this research focuses on using a flame reactor (using ethylene as the fuel) to deposit carbon nanostructures on substrates (both metal-catalyzed as well as non-catalyzed deposition) in order to achieve desirable surface properties. Nickel and iron were primarily used as catalysts and the effect of iron nanoparticles obtained from a ferrofluid was also observed. While the nickel wire catalyst mainly resulted in carbon nanotubes with catalyst particles at their tips (tip-growth mechanism), both iron and the ferrofluid produced mainly a forest of carbon nanotubes/nanofibers/nanopearls. Silicon surfaces used as substrates without any catalyst coating resulted in the deposition of amorphous carbon films, which were observed to be superhydrophobic over a certain area. Thus, a cheap yet very dependable and highly repeatable and rapid on-demand process was developed whereby superhydrophobic films could be deposited on surfaces that can withstand high flame temperatures (typically 1200 – 1500 K). The hydrophobicity was observed to be extremely durable over long periods of time. Stainless steel (SS) meshes were used for the deposition of carbon nanostructures on them and these were then used as anodes in microbial fuel cells. It was observed that biofilms were formed and attached on to these surfaces having nano/microscale asperities. Their degree of attachment was observed to be far superior than to plain SS substrates.

The CNT growth model developed in this research is one of the first such models which combine the different processes involved in their catalytic synthesis. The model has been developed to cluster gas phase chemistry, carbon deposition by catalytic effect on metal catalyst particles, carbon diffusion through the particles, nucleation and subsequent growth of carbon nanostructures. It also handles catalyst poisoning by the formation of an encapsulating layer. The model has been validated for chemical vapor deposition (CVD) synthesis of CNTs against three sets of data for cobalt (Co) and iron (Fe) catalysts and then extended to flame synthesis conditions. Flame conditions have been modeled using extended chemistry for ethylene pyrolysis.

Impact of the research

This particular research has a two-fold impact as far as economic production of CNS is concerned. First of all, a very rapid yet cheap method is developed, by which surfaces could be covered with a superhydrophobic carbon film. This provides very economic fabrication of anodes for MiFCs to which microbial colonies will attach readily, thereby enhancing wastewater treatment. These biofilms can produce electrons which results in electricity production in a fuel cell. Secondly, the comprehensive model for CNT growth can predict the conditions that will lead to desired growth rates, and can form a very helpful predictive tool by saving a lot of experimental iterations, which could be potentially very expensive, especially for CVD conditions. The model will also help in a fundamental understanding of the CNT growth phenomena, which is necessary to devise appropriate synthesis methods for desired CNT growth rates and structures.

Future work

A similar model for catalytic silicon nanowire/nanowhisker (SiNW) growth is presently also developed because of its inherent similarity to catalytic CNT growth. However, the nucleation chemistry and especially catalyst poisoning is not fully understood. Such a comprehensive catalytic growth model for SiNWs has not been reported in literature, and hence, holds a lot of potential for future research direction for the group. The structure of SiNWs and their growth rate is also closely related to the contact angle between the molten catalyst (usually gold) particle and the growing SiNW. Clustering all these phenomena will make a complete study.

We have been collaborating on research on wastewater treatment and simultaneous production of electricity by using microbial fuel cells (MiFCs). Biofilm formation is observed to be much superior on anode substrates prepared by flame deposition of carbon nanostructures.

CITED LITERATURE

[1] Sen, S., and Puri, I.K., Flame synthesis of carbon nanofibers and nanofiber composites containing encapsulated metal particles. *Nanotechnology* 15(3):264-8 (2004).

[2] Arana, C., Sen, S., and Puri, I.K., Catalyst influence on the flame synthesis of aligned carbon nanotubes and nanofibers. *Proceedings of the Combustion Institute* 30(2):2553-60 (2004)

[3] Singer, J.M., and Grumer, J., Carbon formation in very rich hydrocarbon-air flames—I. Studies of chemical content, temperature, ionization and particulate matter. *Proceedings of the Combustion Institute* 7(1):559-69 (1958).

[4] Ijima, S., Helical microtubules of graphitic carbon. *Nature* 354:56-8 (1991).

[5] Morales, A. M. and Lieber, C. M., A laser ablation method for synthesis of crystalline semiconductor nanowires. *Science* 279:208-11 (1998).

[6] Saito, R., Fujita, M., Dresselhaus, G., and Dresselhaus, M.S., Electronic structure of chiral graphene tubules. *Applied Physics Letters* 60:2204-6 (1992).

[7] Wei, B.Q., Vajtai, R., and Ajayan, P.M., Sequence growth of carbon fibers and nanotube networks by CVD process. *Carbon* 41:179-98 (2003).

[8] Li, X., Ci, L., Kar, S., Soldano, C., Kilpatrick, S.J., and Ajayan, P.M., Densified aligned carbon nanotube films via vapor phase infiltration of carbon. *Carbon* 45:847-51 (2007).

[9] Ou, F.S., Shaijumon, M.M., Ci, L., and Ajayan, P.M., Template assembly of tube-in-tube carbon nanotubes using Cu as catalyst. *Carbon* 45:1696-716 (2007).

[10] Saveliev, A.V., Merchan-Merchan, W., and Kennedy, L.A., Metal catalyzed synthesis of carbon nanostructures in an opposed flow methane oxygen flame. *Combustion and Flame* 135(1-2):27-33 (2003).

[11] Height, M.J., Howard, J.B., Tester, J.W., and Vander Sande, J.B., Flame synthesis of single-walled carbon nanotubes. *Carbon* 42(11):2295-307 (2004).

[12] Vander Wal, R.L., Fe-catalyzed single-walled carbon nanotube synthesis within a flame environment. *Combustion and Flame* 130(1-2):37-47 (2002).

[13] Merchan-Merchan, W., Saveliev, A.V., Kennedy, L.A., and Fridman, A., Formation of carbon nanotubes in counter-flow, oxy-methane diffusion flames without catalysts. *Chemical Physics Letters* 354(1-2):20-4 (2002).

[14] Merchan-Merchan, W., Saveliev, A.V., and Kennedy, L.A., High-rate flame synthesis of vertically aligned carbon nanotubes using electric field control. *Carbon* 42(3):599-608 (2004).

[15] Okuno, H., Issi, J.-P., and Charlier, J.-C., Catalyst assisted synthesis of carbon nanotubes using the oxy-acetylene combustion flame method. *Carbon* 43(4):864-6 (2005).

[16] Lambert, J.M., Ajayan, P.M., and Bernier, P., Synthesis of single and multi-shell carbon nanotubes. *Synthetic Metals*, 70:1475-6 (1995).

[17] Zavarukhin, S.G., and Kuvshinov, G.G., The kinetic model of formation of nanofibrous carbon from CH_4–H_2 mixture over a high-loaded nickel catalyst with consideration for the catalyst deactivation. *Applied Catalysis* A, 272(1-2):219-27 (2004).

[18] Kuwana, K., and Saito, K., Modeling CVD synthesis of carbon nanotubes: Nanoparticle formation from ferrocene. *Carbon* 43(10):2088-95 (2005).

[19] Scott, C.D., Chemical Models for Simulating Single-Walled Nanotube Production in Arc Vaporization and Laser Ablation Processes. *Journal of Nanoscience and Nanotechnology* 4(4):368-76 (2004).

[20] Dateo, C.E., Gokcen, T., and Meyyappan, M., Modeling of the HiPco Processes for Carbon Nanotube Production. I. Chemical Kinetics. *Journal of Nanoscience and Nanotechnology* 2(5):523-34 (2002).

[21] Zhang, Y., and Smith, K.J., A kinetic model of CH_4 decomposition and filamentous carbon formation on supported Co catalysts. *Journal of Catalysis* 231(2):354-64 (2005).

[22] Perez-Cabero, M., Romeo, E., Royo, C., Monzon, A., Guerrero-Ruiz, A., and Rodriguez-Ramos, I., Growing mechanism of CNTs: a kinetic approach. *Journal of Catalysis* 224(1):197-205 (2004).

[23] D'Anna, A., Violi, A., D'Alessio, A., and Sarofim, A.F., A reaction pathway for nanoparticle formation in rich premixed flames. *Combustion and Flame* 127(1-2):1995-2003 (2001).

[24] Endo, H., Kunawa, K., Saito, K., Qian, D., Andrews, R., and Grulke, E.A., CFD prediction of carbon nanotube production rate in a CVD reactor. *Chemical Physics Letters* 387(4-6):307-11 (2004).

[25] Hinkov, I., Farhat, S., and Scott, C.D., Influence of the gas pressure on single-wall carbon nanotube formation. *Carbon* 43(12):2453-62 (2005).

[26] Kee, R.J., Rupley, F.M., and Miller, J. A., CHEMKIN: A Fortran chemical kinetics package for the analysis of gas phase chemical kinetics. Sandia National Laboratories Report No. 89-8009B.

[27] Krestinin, A.V., and Moravsky, A.P., Mechanism of fullerene synthesis in the arc reactor. *Chemical Physics Letters* 286(5):479-84 (1998).

[28] Gommes, C., Blacher, S., Bossuot, Ch., Marchot, P., Nagy, J.B., and Pirard, J.-P., Influence of the operating conditions on the production rate of multi-walled carbon nanotubes in a CVD reactor. *Carbon* 42(8-9):1473-82 (2004).

[29] Yu, Z., Chen, D., Totdal, B., and Holmen, A., Effect of catalyst preparation on the carbon nanotube growth rate. *Catalysis Today* 100(3-4):261-7 (2005).

[30] Villacampa, J.I., Royo, C., Romeo, E., Montoya, J.A., Del Angel, P., and Monzon, A., Catalytic decomposition of methane over Ni-Al_2O_3 coprecipitated catalysts: Reaction and regeneration studies. *Applied Catalysis A* 252(2):363-83 (2003).

[31] Snoeck, J.-W., Froment, G.F., and Fowles, M., Kinetic Study of the Carbon Filament Formation by Methane Cracking on a Nickel Catalyst. *Journal of Catalysis* 169(1):250-62 (1997).

[32] Chen, D., Christensen, K.O., Ochoa-Fernandez, E., Yu, Z., Totdal, B., Latorre, N., Monzon, A., and Holmen, A., Synthesis of carbon nanofibers: effects of Ni crystal size during methane decomposition. *Journal of Catalysis* 229(1):82-96 (2005).

[33] Puretzky, A.A., Geohegan, D.B, Jesse, S., Ivanov, I.N., and Eres, G., In situ measurements and modeling of carbon nanotube array growth kinetics during chemical vapor deposition. *Applied Phys*ics *A* 81:223-40 (2005).

[34] Zhang, Q.L., O'Brien, S.C., Heath, J.R., Liu, Y., Curl, R.F., Kroto, H.W., and Smalley, R.E., Reactivity of large carbon clusters: spheroidal carbon shells and their possible relevance to the formation and morphology of soot. *Journal of Physical Chemistry* 90(4):525-8 (1986).

[35] Howard, J.B., McKinnon, T., Makarovsky, Y., Lafleur, A.L., and Johnson, M.E., Fullerenes C60 and C70 in Flames. *Nature* 352:139-41 (1991).

[36] Howard, J.B., Chowdhury, K.D., and Vander Sande, J.B., Carbon Shells in Flames. *Nature* 370:603 (1994).

[37] Vander Wal, R.L., Ticich, T.M., and Curtis, V.E., Diffusion flame synthesis of single-walled carbon nanotubes. *Chemical Physics Letters* 323(3-4):217-23 (2000).

[38] Yuan, L., Saito, K., Pan, C., Williams, F.A., and Gordon, A.S., Nanotubes from methane flames. *Chemical Physics Letters* 340(3-4):237-41 (2001).

[39] Merkulov, V.I., Melechko, A.V., Guillorn, M.A., Lowndes, D.H., and Simpson, M.L., Growth rate of plasma-synthesized vertically aligned carbon nanofibers. *Chemical Physics Letters* 361(5-6):492-8 (2002).

[40] Yuan, L., Saito, K., Hu, W., and Chen, Z., Ethylene flame synthesis of well-aligned multi-walled carbon nanotubes. *Chemical Physics Letters* 346(1-2):23-8 (2001).

[41] Vander Wal, R.L., and Hall, L.J., Flame synthesis of Fe catalyzed single-walled carbon nanotubes and Ni catalyzed nanofibers: growth mechanisms and consequences. *Chemical Physics Letters* 349(3-4):178-84 (2001).

[42] Vander Wal, R.L., and Ticich, T.M., Flame and Furnace Synthesis of Single-Walled and Multi-Walled Carbon Nanotubes and Nanofibers. *Journal of Physical Chemistry B* 105(42):10249-56 (2001).

[43] Vander Wal, R.L., Flame synthesis of Ni-catalyzed nanofibers *Carbon* 40(12):2101-7 (2002).

[44] Vander Wal, R.L., and Hall, L.J., Ferrocene as a precursor reagent for metal-catalyzed carbon nanotubes: competing effects. *Combustion and Flame* 130(1-2):27-36 (2002).

[45] Baker, R.T.K., Harris, P.S., Thomas, R.B., and Waite, R.J., Formation of filamentous carbon from iron, cobalt and chromium catalyzed decomposition of acetylene. *Journal of Catalysis* 30(1):86-95 (1973).

[46] Tibbets, G.G., Devour, M.G., and Rodda, E.J., An adsorption-diffusion isotherm and its application to the growth of carbon filaments on iron catalyst particles. *Carbon* 25(3):367-75 (1987).

[47] Rodriguez, N.M., A review of catalytically grown carbon nanofibers. *Journal of Materials Research* 8(12): 3233-50 (1993).

[48] Dai, H., Rinzler, H.G., Nikolavev, P., Thess, A., Colbert, D.T., and Smalley, R.E. Single-wall nanotubes produced by metal-catalyzed disproportionation of carbon monoxide. *Chemical Physics Letters* 260(3-4):471-5 (1996).

[49] Lee, G.W., Jurng, J., and Hwang, J., Formation of Ni-catalyzed multiwalled carbon nanotubes and nanofibers on a substrate using an ethylene inverse diffusion flame. *Combustion and Flame* 139(1-2):167-75 (2004).

[50] Pan, C., Liu, Y., Cao, F., Wang, J., and Ren, Y., Synthesis and growth mechanism of carbon nanotubes and nanofibers from ethanol flames. *Micron* 35(6):461-8 (2004).

[51] Nakazawa, S., Yokomori, T., and Mizomoto, M., Flame synthesis of carbon nanotubes in a wall stagnation flow. *Chemical Physics Letters* 403(1-3):158-62 (2005).

[52] Tsantilis, S., Kammler, H.K., and Pratsinis S.E., Population balance modeling of flame synthesis of titania nanoparticles. *Chemical Engineering Science* 57(12):2139-56 (2002).

[53] Robertson, J., Diamond-like amorphous carbon. *Materials Science and Engineering R* 37(4-6):129-281 (2002).

[54] Levesque, A., Binh, V.T., Semet, V., Guillot, D., Fillit, R.Y., Brookes, M.D., *et al*., Mono disperse carbon nanopearls in a foam-like arrangement: a new carbon nano-compound for cold cathodes. *Thin Solid Films* 464-465:308-14 (2004).

[55] Naha, S., Sen, S., and Puri, I.K., Flame synthesis of superhydrophobic amorphous carbon surfaces. *Carbon* 45(8):1702-6 (2007).

[56] Schulz, H., Leonhardt, M., Scheibe, H.-J., and Schultrich, B., Ultra hydrophobic wetting behavior of amorphous carbon films. *Surface and Coatings Technology* 200(1-4):1123-6 (2005).

[57] Zhou, Y., Wang, B., Song, X., Li, E., Li, G., Zhao, S., *et al*., Control over the wettability of amorphous carbon films in a large range from hydrophilicity to super-hydrophobicity. *Applied Surface Science* 253(5):2690-4 (2006).

[58] Wang, Z.L., and Kang, Z.C., Pairing of Pentagonal and Heptagonal Carbon Rings in the Growth of Nanosize Carbon Spheres Synthesized by a Mixed-Valent Oxide-Catalytic Carbonization Process. *Journal of Physical Chemistry* 100(45):17725-31 (1996).

[59] Pozzato, A., Dal Zilio, S., Fois, G., Vendramin, D., Mistura, G., Belotti, M., *et al*. Superhydrophobic surfaces fabricated by nanoimprint lithography. *Microelectronic Engineering* 83(4-9):884-8 (2006).

[60] Arana, C., Pontoni, M., Sen, S., and Puri, I.K., Field measurements of soot volume fractions in laminar partially premixed coflow ethylene/air flames. *Combustion and Flame* 138(4):362-72 (2004).

[61] Sharon, M., Mukhopadhyay, K., Yase, K., Iijima, S., Ando, Y., and Zhao, S., Spongy carbon nanobeads: A new material. *Carbon* 36(5-6):507-11 (1998).

[62] McFeely, F.R., Kowalcyk, S.P., Ley, L., Cavell, R.G., Pollak, R.A., and Shirley D.A., X-ray photoemission studies of diamond, graphite, and glassy carbon valence bands. *Physical Review B* 9(12):5268-78 (1974).

[63] Diaz, J., Paolicelli, G., Ferrer, S., and Comin, F., Separation of sp^3 and sp^2 components in the C1s photoemission spectra of amorphous carbon films. *Physical Review B* 54(11):8064-9 (1996).

[64] Dentel, S. K., Strogen, B., Sharma, A., and Chiu, P. C., Direct generation of electricity from sludges and other liquid wastes. *Water Science and Technology* 50(9):161-8 (2004).

[65] Logan, B., Cheng, S., Watson, V., and Estadt, G., Graphite fiber brush anodes for increased power production in air-cathode microbial fuel cells. *Environmental Science & Technology* 41(9):3341-6 (2007).

[66] Naha, S., Sen, S., De, A.K., and Puri, I.K., A detailed model for the flame synthesis of carbon nanotubes and nanofibers. *Proceedings of the Combustion Institute* 31(2):1821-9 (2007).

[67] Liu, H., and Dandy, D.S., Nucleation Kinetics of Diamond on Carbide-Forming Substrates during Chemical Vapor Deposition. *Journal of the Electrochemical Society* 143(3):1104-9 (1996).

[68] Samorjai, G.A., Introduction to Surface Chemistry and Catalysis, John Wiley and Sons, Inc., New York (1994).

[69] Chen, D., Lodeng,R., Anundskas, A., Olsvik, O., and Holmen, A., Deactivation during carbon dioxide reforming of methane over Ni catalyst: microkinetic analysis. *Chemical Engineering Science* 56 (4):1371-9 (2001).

[70] Naha, S., and Puri, I.K., A Model for Catalytic Growth of Carbon Nanotubes. *Journal of Physics D: Applied Physics* 41(6):065304 (6 pp) (2008).

[71] Venables, J.A., Spiller, G.D.T., and Hanbucken, N., Nucleation and growth of thin films. *Reports on Progress in Physics* 47(4):399-459 (1984).

[72] Yokoyama, H., Namakura, H., and Koiwa, M., The solubility and diffusion of carbon in palladium. *Acta Materiala* 46 (8):2823-30 (1998).

[73] Sharma, R., Rez, P., Brown, M., Du, G., and Treacy M.M.J., Dynamic observations of the effect of pressure and temperature conditions on the selective synthesis of carbon nanotubes. *Nanotechnology* 18(12):125602(8pp) (2007).

[74] Jönsson, M., Nerushev, O.A., and Campbell, E.E.B., In situ growth rate measurements during plasma-enhanced chemical vapour deposition of vertically aligned multiwall carbon nanotube films. *Nanotechnology* 18(30):305702(5pp) (2007).

[75] Liu, K., Jiang, K., Feng, C., Chen, Z., and Fan, S., A growth mark method for studying growth mechanism of carbon nanotube arrays. *Carbon* 43(14):2850-6 (2005).

[76] Bower, C., Zhou, O., Zhu, W., Werder, D.J., and Jin, S., Nucleation and growth of carbon nanotubes by microwave plasma chemical vapor deposition. *Applied Physics Letters* 77(17):2767-9 (2000).

[77] Yun. J., and Dandy, D.S., A kinetic model of diamond nucleation and silicon carbide interlayer formation during chemical vapor deposition. *Diamond and Related Materials* 14:1377-88 (2005).

[78] Bronikowski. M.J., CVD growth of carbon nanotube bundle arrays. *Carbon* 44:2822-32 (2006).

[79] Ding, F., Rosén, A., and Bolton, K., Molecular dynamics study of the catalyst particle size dependence on carbon nanotube growth. *Journal of Chemical Physics* 121(6):2775-9 (2004).

[80] Park, J.H., Alegaonkar, P. S., Jeon, S. Y., and Yoo, J. B., Carbon nanotube composite: Dispersion routes and field emission parameters. Composites Science and Technology 68:753-9 (2008).

[81] Camponeschi, E., Vance, R., Al-Haik, M., Garmestani, H., and Tannenbaum, R., Properties of carbon nanotube–polymer composites aligned in a magnetic field. Carbon 45:2037-46 (2007).

[82] Krajcik, R., Jung, A., Hirsch, A., Neuhuber, W., and Zolk, O., Functionalization of carbon nanotubes enables non-covalent binding and intracellular delivery of small interfering RNA for efficient knock-down of genes. Biochemical and Biophysical Research Communications 369:595-602 (2008).

[83] Louchev, O. A., Laude, T., Sato, Y., and Kanda, H., Diffusion-controlled kinetics of carbon nanotube forest growth by chemical vapor deposition. The Journal of Chemical Physics 118:7622-34 (2003)

[84] Katta, V.R., Goss, L.P., and Roquemore, W.M., Effect of Non-unity Lewis Number and Finite-rate Chemistry on the Dynamics of a Hydrogen-air Jet Diffusion Flame. *Combustion and Flame* 96(1-2):60-74 (1994).

[85] Nolan, P.E., Lynch, D.C., and Cutler, A.H., Catalytic disproportionation of CO in the absence of hydrogen: Encapsulating shell carbon formation. *Carbon* 32(3):477-83 (1994).

[86] Rodriguez, N.M., Kim, M.S., and Baker, R.T.K., Promotional Effect of Carbon Monoxide on the Decomposition of Ethylene over an Iron Catalyst. *Journal of Catalysis* 144(1):93-108 (1993).

[87] Ichinose, N., Ozaki, Y., and Kashu, S., Superfine Particle Technology, Springer Verlag, London, pp. 201-15 (1991).

[88] Yu, Z., Chen, D., Totdal, B., Zhao, T., Dai, Y., Yuan, W., and Holmen, A., Catalytic engineering of carbon nanotube production. *Applied Catalysis A* 279(1-2):223-33 (2005).

[89] Li, C., Liu, Z., Gu., C., Xu, X., and Yang, Y., Controllable Synthesis and Growth Model of Amorphous Silicon Nanotubes with Periodically Dome-Shaped Interiors. *Advanced Materials* 18:228-34 (2006).

[90] Wagner, R.S., and Ellis, W.C., Vapor-Liquid-Solid Mechanism of Single Crystal Growth. *Applied Physics Letters* 4(5):89-90 (1964).

[91] Wang, N., Cai, Y., and Zhang, R.Q., Growth of nanowires. *Materials Science and Engineering R* 60:1-51 (2008).

[92] Givargizov, E.I., Highly Anisotropic Crystals. Springer, New York (1987).

[93] Wang, H., and Fischman, G.S., Role of liquid droplet surface diffusion in the vapor-liquid-solid whisker growth mechanism. *Journal of Applied Physics* 76:1557-62 (1994).

[94] Obretenov, W., Kashchiev, D., and Bostanov, V., United Description of the Rate of Nucleation-Mediated Crystal Growth. *Journal of Crystal Growth* 96:843-8 (1989).

[95] Kashchiev, D., Nucleation: basic theory with applications. Butterworth-Heinemann, Oxford, UK (2000).

[96] Saltsburg, S., Smith, J.N. (Jr.), and Rogers, M., Fundamentals of Gas-Surface Interactions. Academic Press (1967).

[97] Zhang, Y., and Smith, K.J., A kinetic model of CH_4 decomposition and filamentous carbon formation on supported Co catalysts. *Journal of Catalysis* 231(2):354-64 (2005).

[98] Onischuk, A.A., Strunin, V. P., Ushakova, M. A., and Panfilov, V. N., Studying of silane thermal decomposition mechanism. *International Journal of Chemical Kinetics* 30(2): 99-110 (1999).

[99] Lasagni, F., Mingler, B., Dumontc, M., and Degischer, H.P., Precipitation kinetics of Si in aluminium alloys. *Materials Science and Engineering A* 480(1-2):383-91 (2008).

[100] Wagner, R., and Kaumpmann, R., Materials Science and Technology: A Comprehensive Treatment. Vol. 5, VCH, Weinheim (1991).

[101] Lew, K.-K., and Redwing, J.M., Growth characteristics of silicon nanowires synthesized by vapor-liquid-solid growth in nanoporous alumina templates. *Journal of Crystal Growth* 254:14-22 (2000).

[102] Wilcox, W.R., and LaChapelle, T.J., Mechanism of Gold Diffusion into Silicon. *Journal of Applied Physics* 35(1):240-6 (1964).

APPENDIX

I. Detailed engineering drawing (not to scale) of parts of the burner used in flame synthesis:

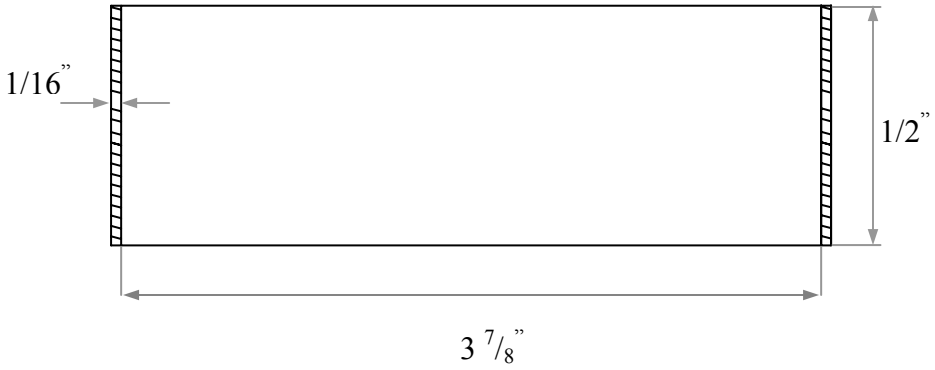

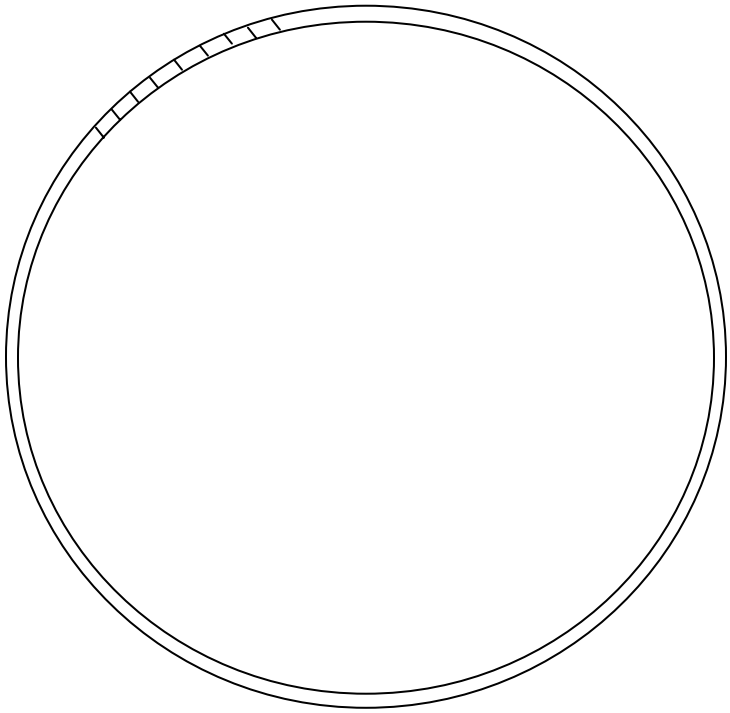

Aluminum Tube (Qty.: 1)

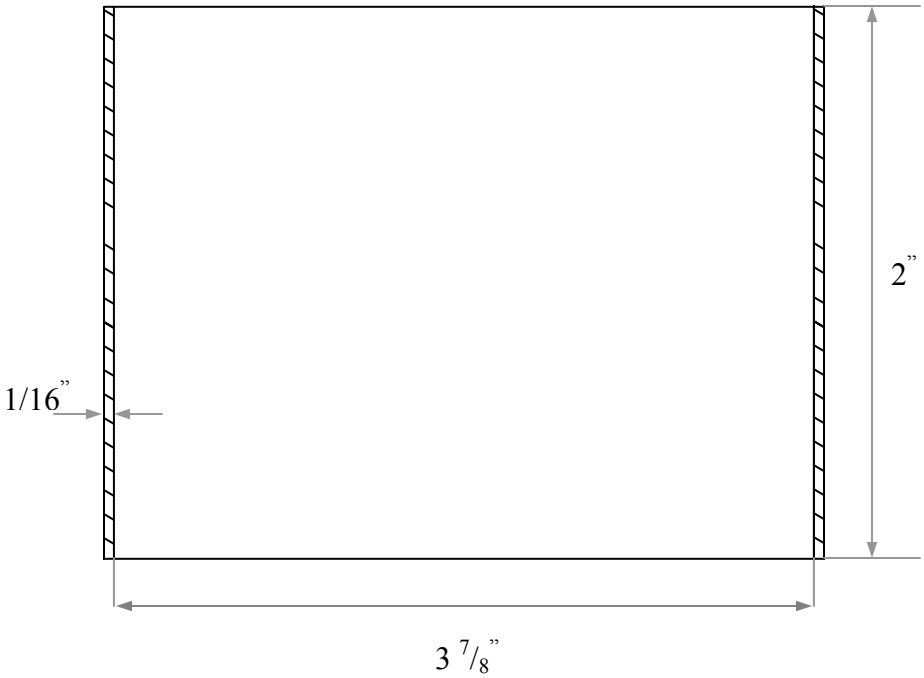

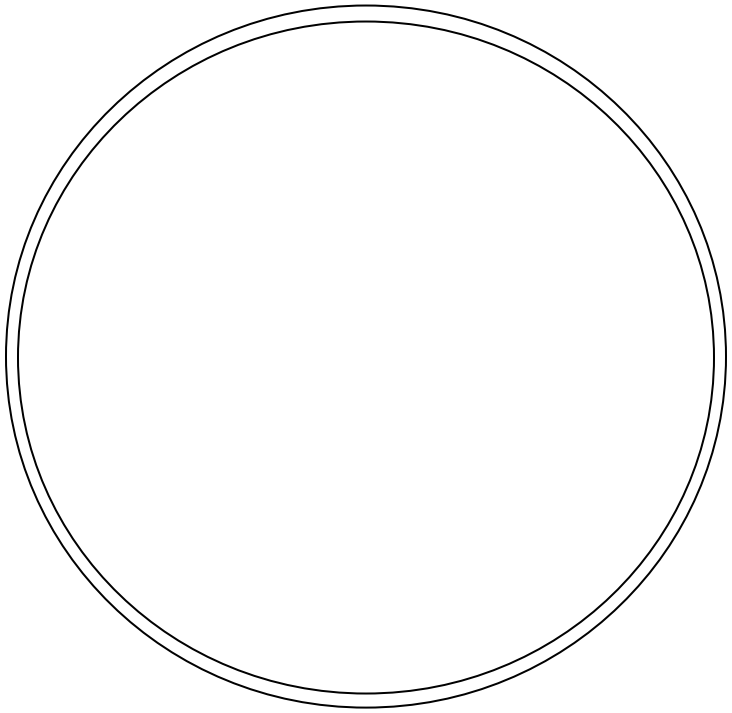

Aluminum Tube (Qty: 1)

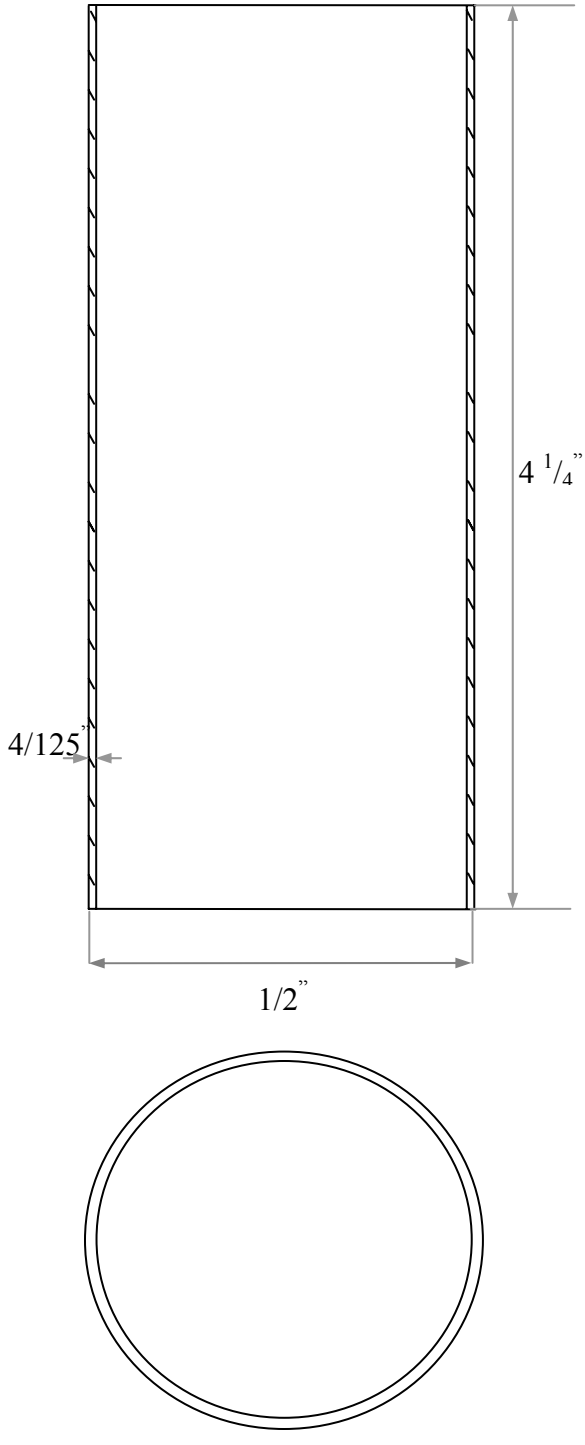

Stainless Steel Tube (Inner tube for fuel inlet) (Qty.: 1)

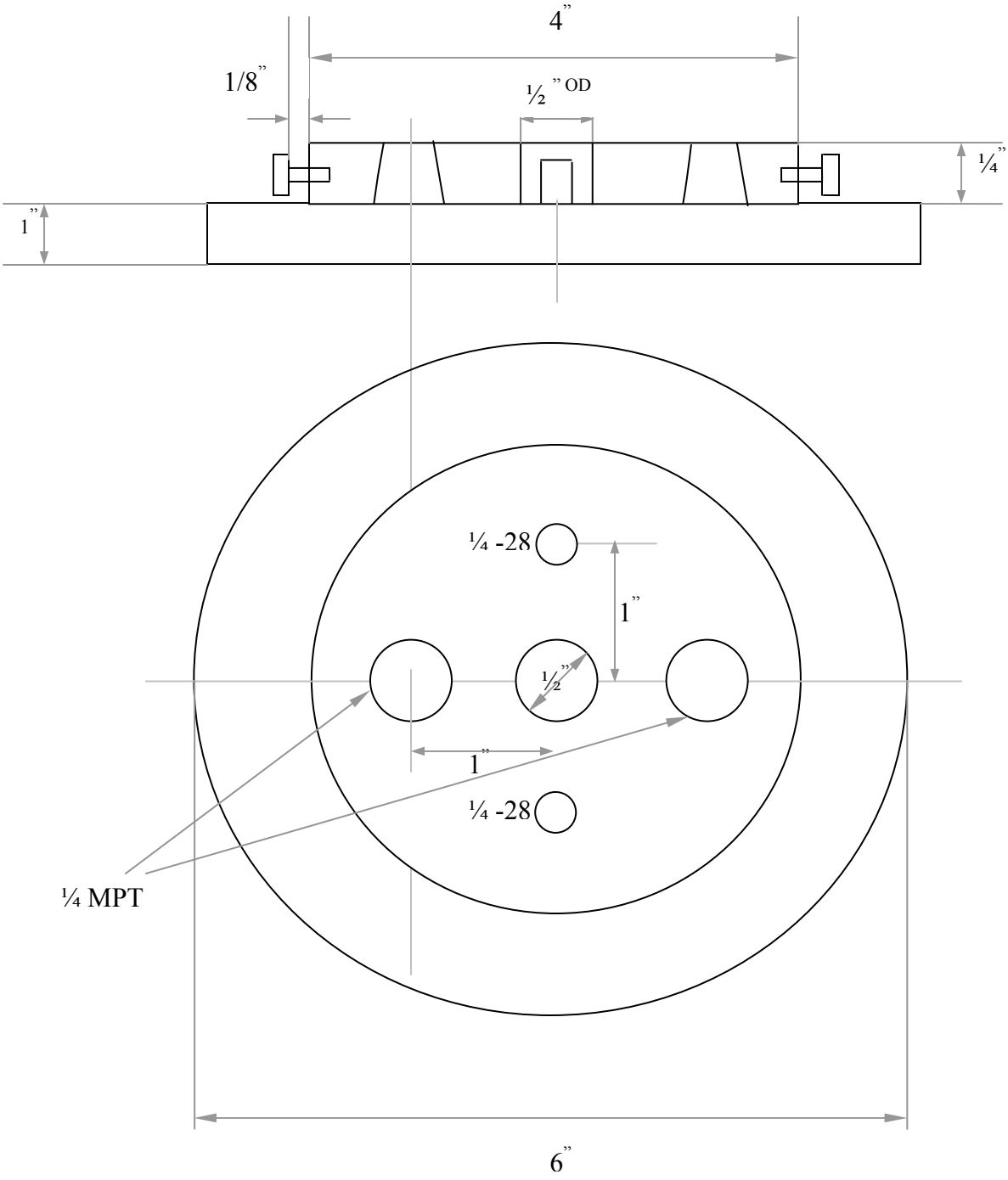

Base of Burner (Aluminum, Qty 1)

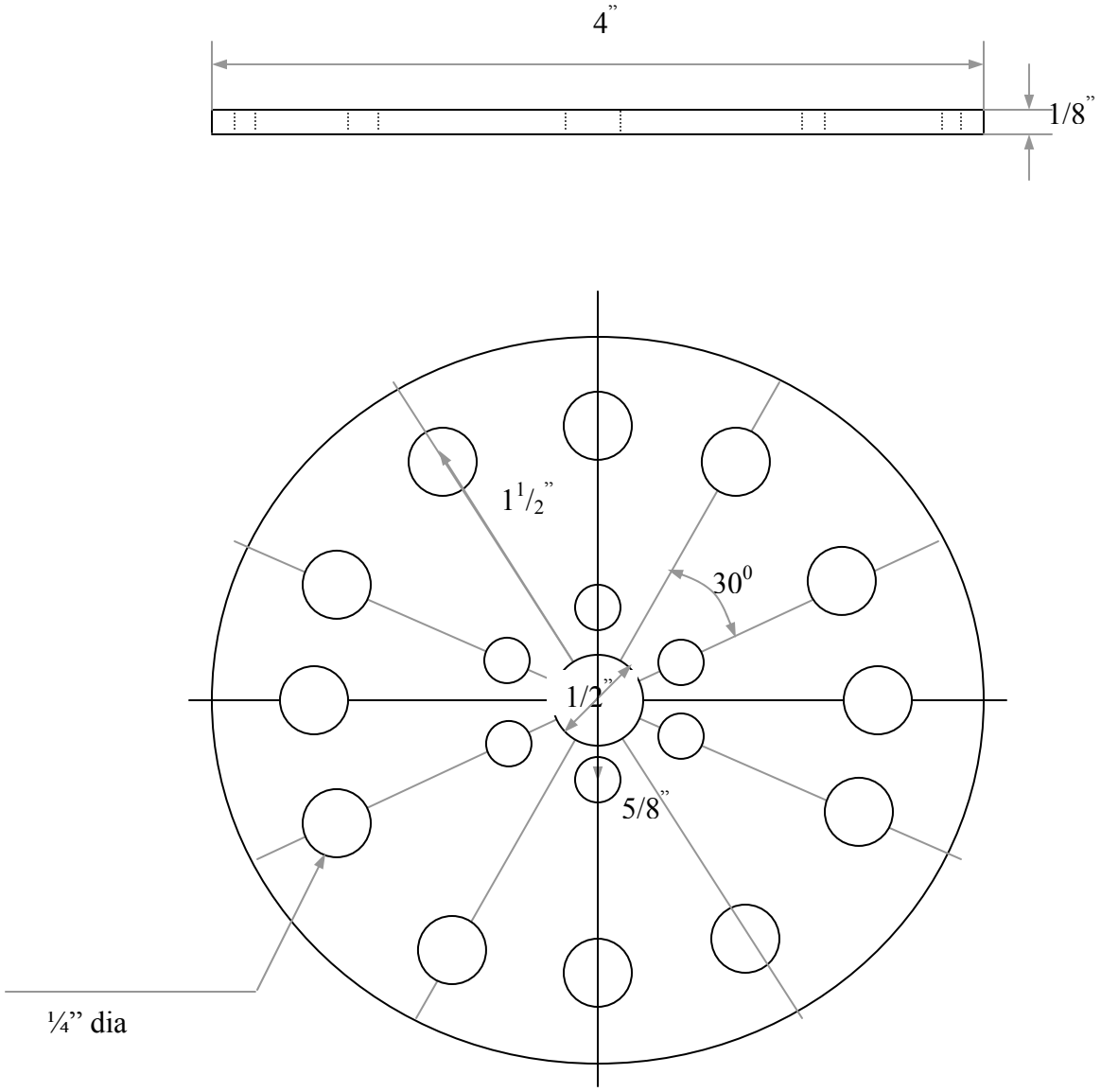

Distributor Plate (Aluminum, Qty 1)

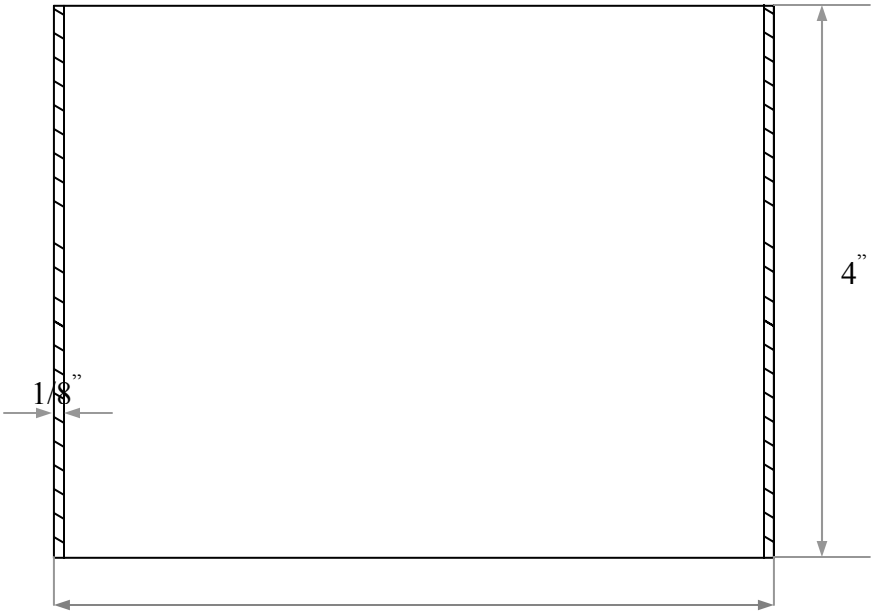

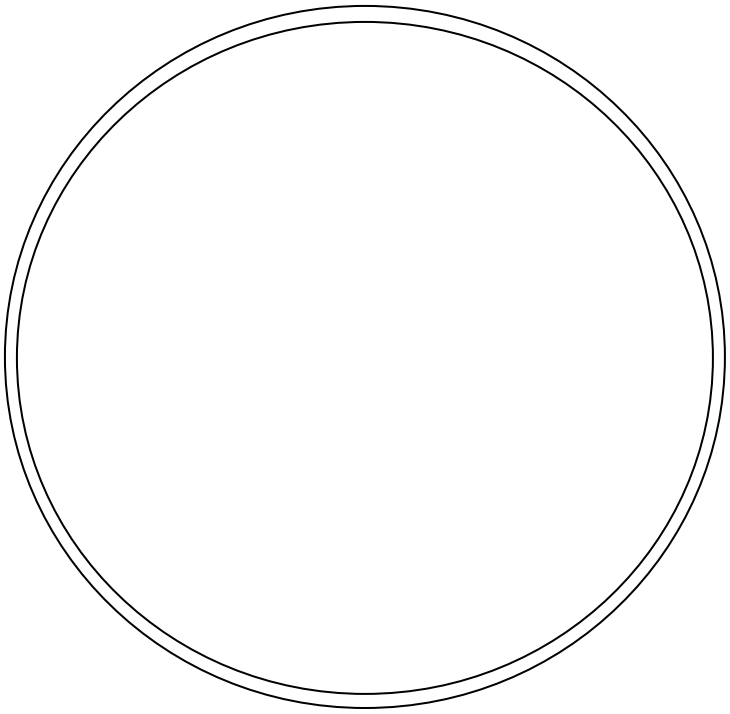

Body (Aluminum, Qty 1)

II. Carbon nanostructures grown on Ni wire catalyst

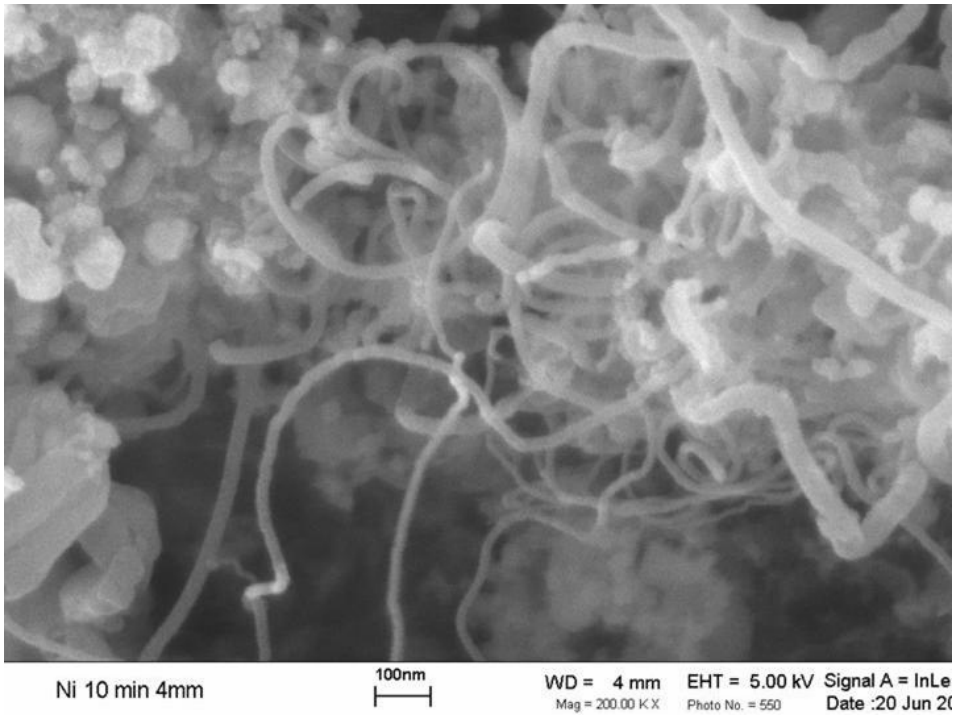

(a)

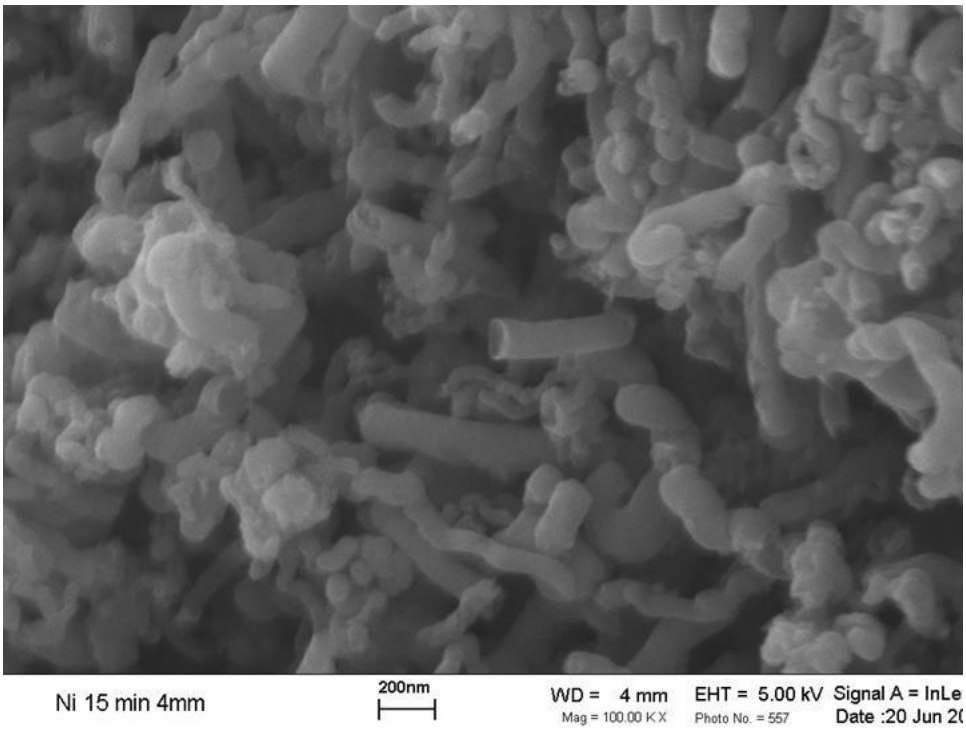

(b)

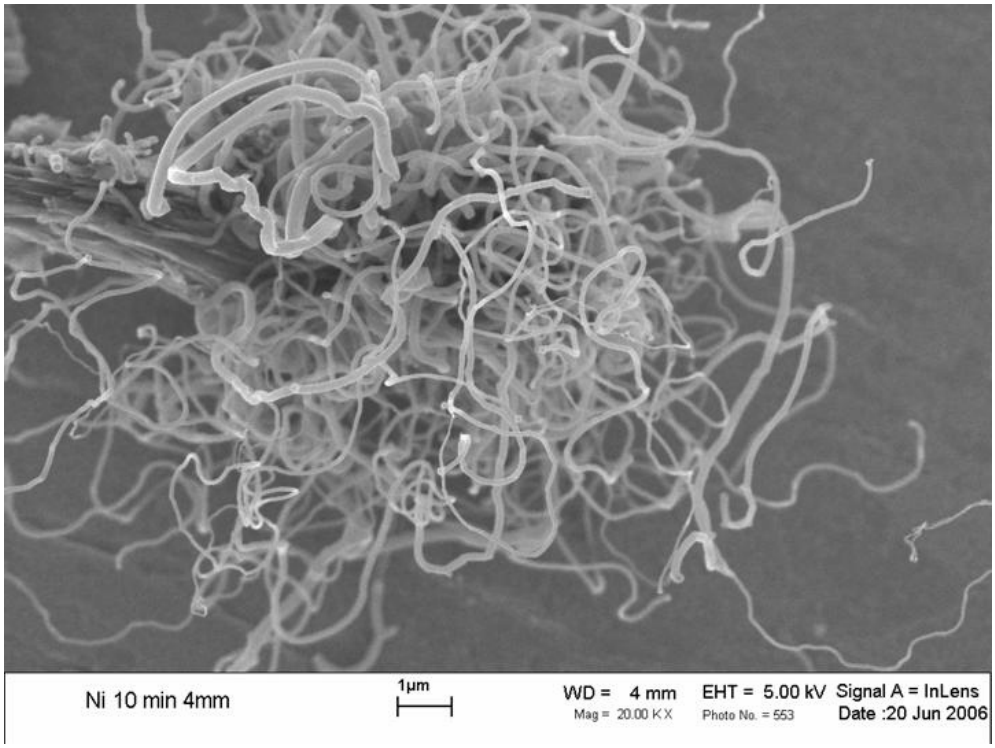

(c)

The figures above show SEM images of CNT/CNFs grown on a Ni wire substrate. Figure (a) shows the structures deposited at 4 mm HAB and for an exposure time of 10 min. Figure (b) shows the same for 15 min. Figure (c) just shows a lower magnification view of a cluster of CNT/CNFs on the Ni substrate.

Element	Weight %	Atomi c%
C K	11.98	19.94
O K	40.70	50.86
Na K	23.03	20.03
S K	1.76	1.10
Fe K	22.53	8.06
Totals	100.00	

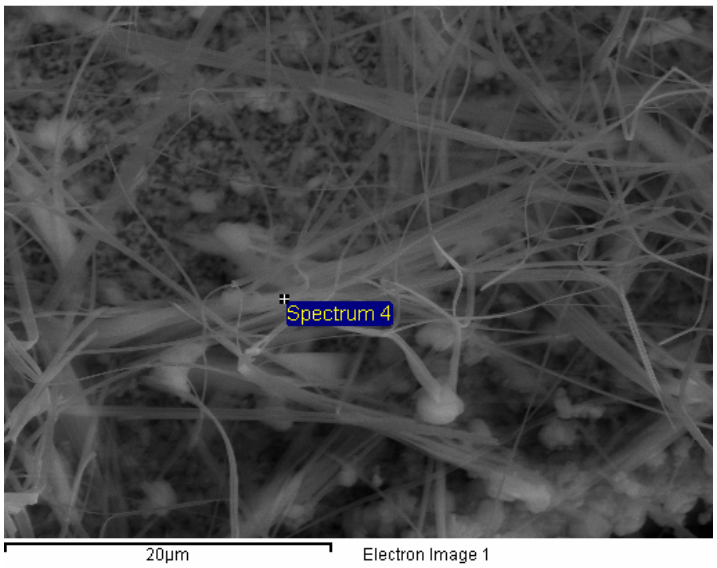

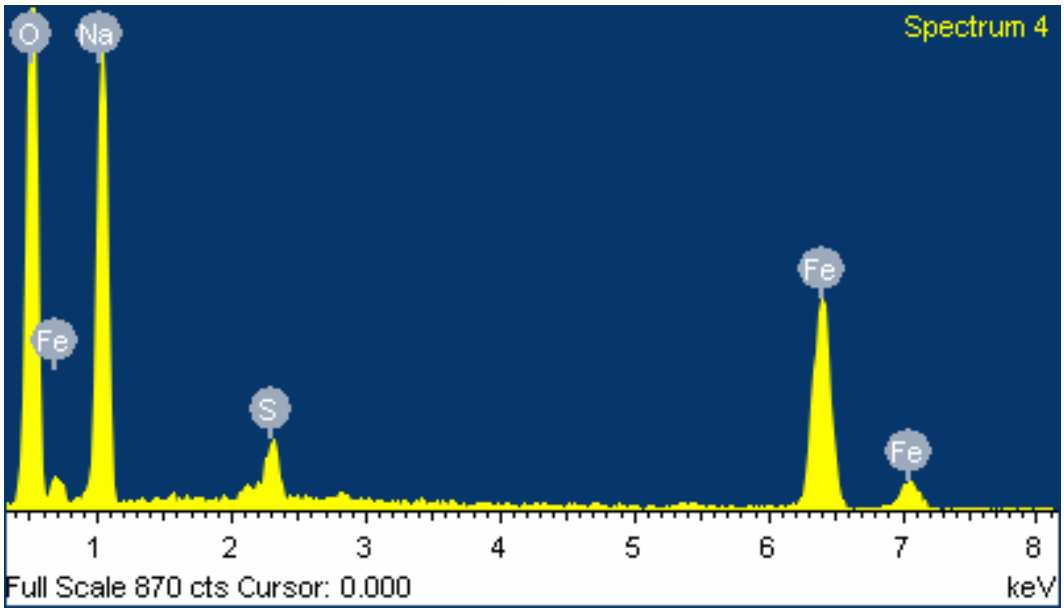

(d)

Figure (d) above shows the SEM image (top right) of a representative area on a stainless steel wire mesh coated with ferrofluid and exposed to the ethylene flame discussed here for 10 minutes. The EDS spectra are shown at the bottom and the elemental analysis on the top left.

Element	Weight %	Atomic %
C K	4.95	12.21
O K	23.60	43.75
Na K	7.65	9.87
S K	0.75	0.69
Fe K	63.06	33.48
Totals	100.00	

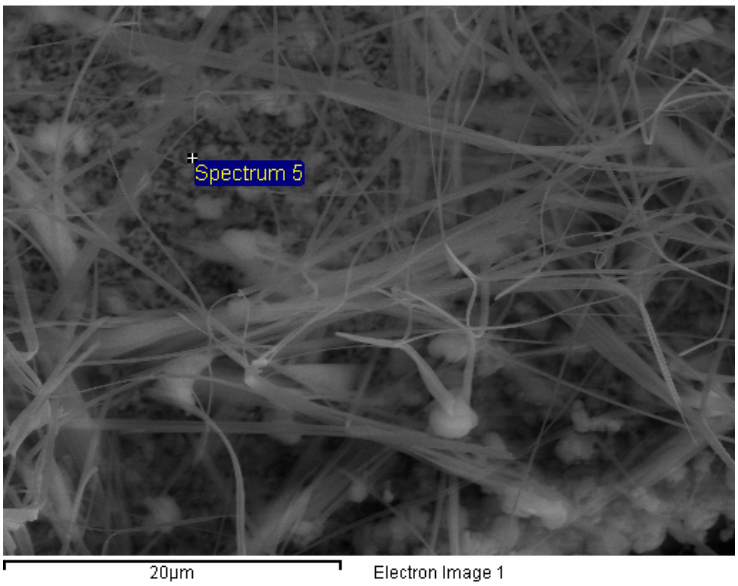

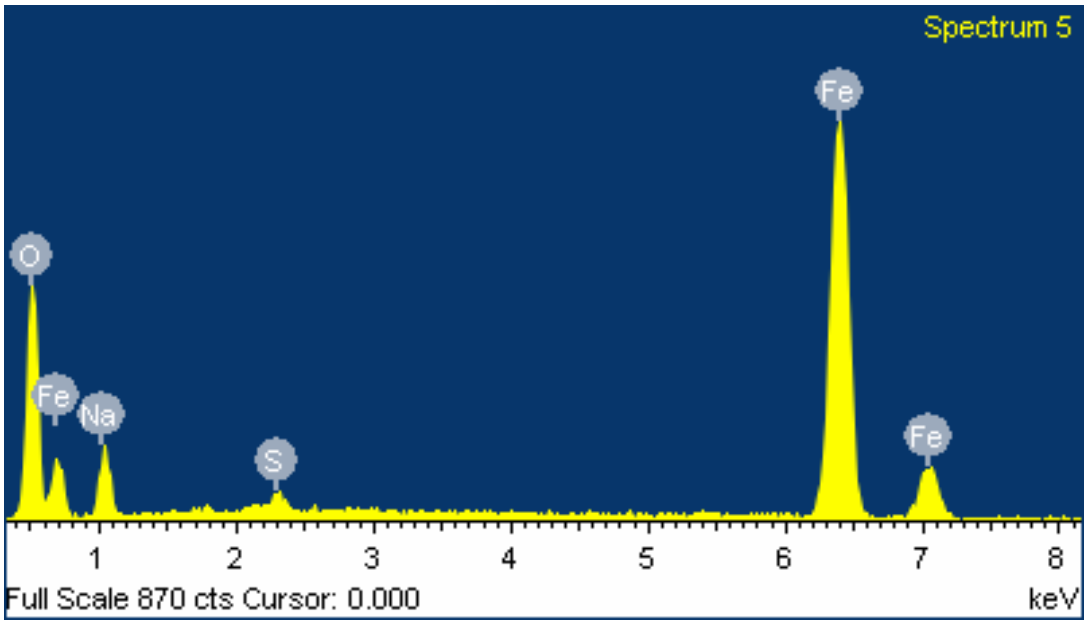

(e)

Figure (e) is similar to the previous one, only at a different location on the same sample, and as can be seen from the elemental analysis, this part has a smaller C content than the previous one.

III. Diffusivities for Si/Au system

The three diffusivity expressions in terms of temperature T suggested in Ref. 102 are as follows, as already discussed:

$$D_b = 2.75 \text{ X } 10^{-3} \exp(- 47400/RT) \qquad \text{(III-1)}$$

$$D_b = 1.15 \text{ X } 10^{3} \exp(- 71800/RT) \qquad \text{(III-2)}$$

$$D_b = 1.78 \text{ X } 10^{-2} \exp(- 26000/RT) \qquad \text{(III-3)}$$

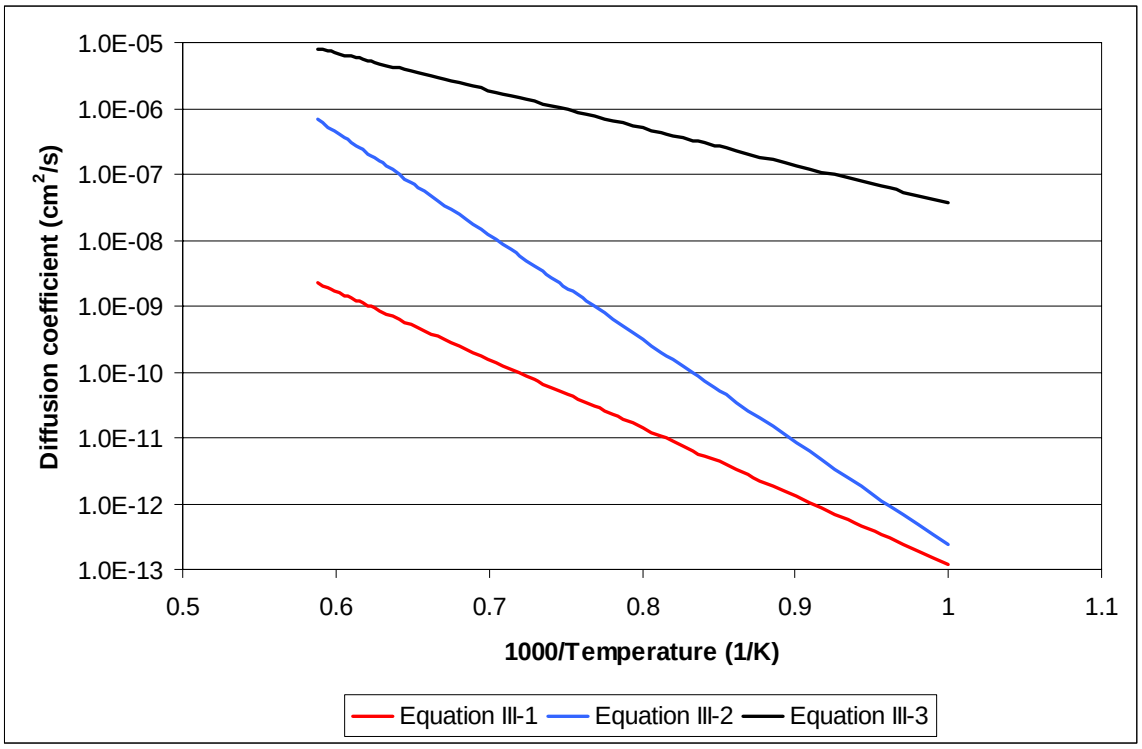

Figure showing the variation of the diffusion coefficient between Si and Au with temperature for the three different expressions reported in Ref. 102. Equation III-3 (depicted by the black plot in the Figure) was chosen as the desirable expression for diffusivity in the calculations discussed in this research.

IV. Specifications of the SEM, TEM, XPS instruments used in this research

1. Field-Emission Scanning Electron Microscope (FE-SEM)

The LEO (Zeiss) 1550 is a high-performance Schottky field-emission SEM capable of resolution in 2-5 nm size range. It is used for high-resolution imaging of surfaces, qualitative assessment of the distribution of elements (with atomic numbers between boron and uranium), submicron structure analysis, and determination of crystal orientation and crystalline texture.

General specifications:

It is equipped with:

- In-lens secondary electron, and Robinson-type back-scattered electron detectors
- Oxford INCA Energy E2H X-ray Energy Dispersive Spectrometer (EDS) system with Silicon Drifted detector
- HKL Nordlys II Electron Back Scatter Diffraction (EBSD) system, including a Forward Scatter Electron (FSE) detector

2. Environmental SEM (E-SEM)

The FEI Quanta 600 FEG is an environmental SEM that can operate in high-vacuum and low-vacuum modes. It is used to image samples that are difficult to impossible to image in high vacuum SEMs; in situ experiments such as hydrating, dehydrating and heating samples are possible with the ESEM. It can operate with pressures around the sample up to 4000 Pa and in conjunction with a Peltier stage can image fully hydrated samples, a critical advantage for imaging biological samples.

General specifications:

It is equipped with:

- High-vacuum, low-vacuum, and extended vacuum modes
- A heating stage to 1000 C
- Bruker EDX with a Silicon Drifted Detector

3. Transmission Electron Microscope (TEM)

The Philips EM 420 is a Scanning Transmission Electron Microscope that uses interactions between an electron beam and a thin sample to extract information about the structure of materials. The instrument is used primarily for imaging the internal structure of materials using differential electron absorption and diffraction contrast. It is the used to survey samples before putting them in the Titan.

General specifications:

It is equipped with:

- Tungsten filament electron gun
- 120 kV maximum accelerating voltage
- Scanning Transmission Electron Microscopy mode (STEM)
- CCD camera for recording images

4. X-ray photoelectron spectrometer (XPS)

XPS studies were conducted in the surface-analysis laboratory of the Chemistry Department at Virginia Tech, which contains a Perkin Elmer 5400 X-ray photoelectron spectrometer (XPS) with ion-scattering spectrometry (ISS) capabilities.

More details of the abovementioned equipment could be found at www.ictas.vt.edu/ncfl.